DTU Physics
Department of Physics

Max-Planck-Institut
für Plasmaphysik

PROBE MEASUREMENTS IN THE X-POINT REGION AT ASDEX UPGRADE

Raheesty Devi Nem

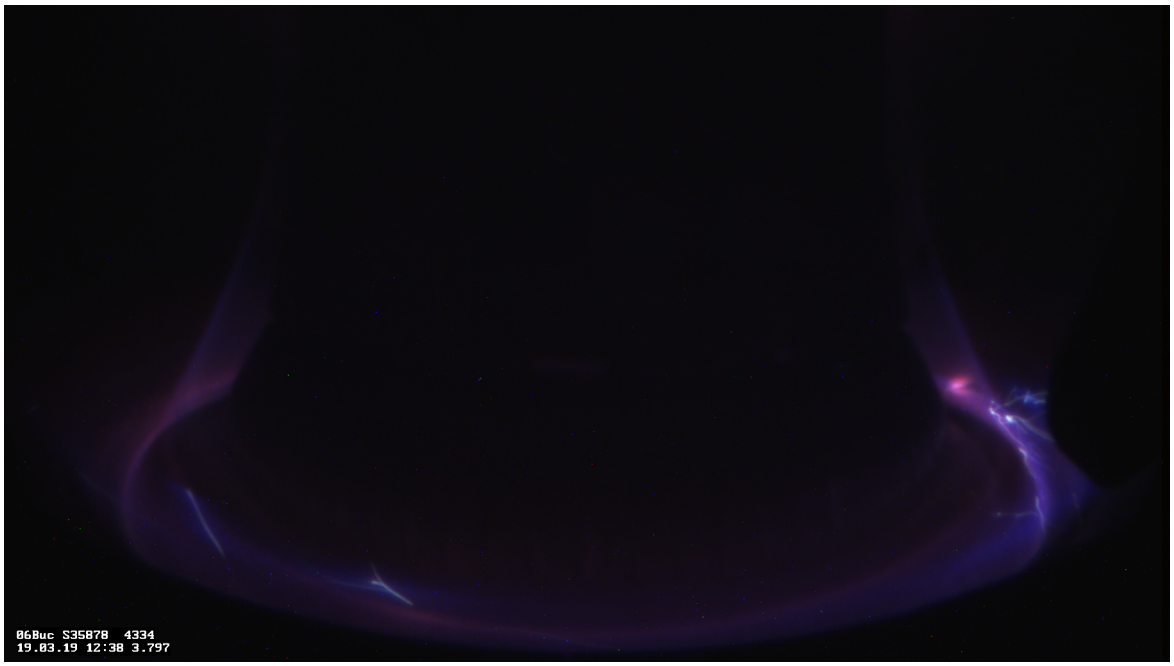

Thesis submitted for a degree of Doctor of Philosophy

Supervisors: Volker Naulin & Thomas Eich

Section for Plasma Physics and Fusion Energy
Department of Physics
Technical University of Denmark
&
Max-Planck-Institut für Plasmaphysik

31 July 2020

Abstract

Plasma fluctuations in the divertor region just below the X-point at ASDEX Upgrade tokamak are investigated using Langmuir probes measurements. These probes are mounted on the X-point manipulator, which provides unique access to measurements of the ion-saturation current through three consecutive regions, the low-field side scrape-off layer, the private flux region and the high-field side scrape-off layer. This enables a detailed analysis, which are provided in two parts. In the first part, a general fluctuation study is presented, in which regions of low fluctuations are identified. The second part focuses on the characteristics of the fluctuations in the three different regions around the X-point and differentiate the universal features to the fluctuations at the outboard mid-plane.

For the first part, spectral analysis methods reveal the presence of a region of low fluctuations not only in the low-field side scrape-off layer, but also in the high-field side of the private flux region of which the latter has not been reported previously. The two 'quiescent' regions are observed both in helium and deuterium plasmas and appear to be generally independent of the auxiliary heating source in use.

For the second part, the application of the filtered Poisson process (FPP) model shows that rather than the universal conditional averaged wave-form of a steep front and trailing wake found at the outboard mid-plane of a wide range of toroidal fusion experimental devices, the X-point fluctuations display a more symmetric wave-form on the low-field side scrape-off layer. Moreover, it is found that the methods used for the conditional averaged wave-form and power spectral density in the FPP model are able to fit the X-point data successfully when considered individually, but not in a unified manner as generally observed at the outboard mid-plane. The discrepancy shows that the X-point region cannot in general be modeled as a series of uncorrelated pulses satisfying the Poisson distribution. This also shows that the fluctuations born at the mid-plane are not surviving and dominant in the divertor region, where local instabilities may also contribute to the fluctuations.

Dansk Resumé

Plasma fluktuationer i divertor området under X-punktet i ASDEX Upgrade tokamakken er undersøgt ved hjælp af Langmuir probe målinger af ion-mætnings-strømmen. Proberne er monteret på X-punktsmanipulatoren og dækker de sammenhængende områder: scrape-off layer på lavfeltssiden, det private fluks område, og scrape-off layer på højfeltssiden. Dette har gjort det muligt at fortage en detaljeret analyse, som præsenteres i to dele. I den første del foretages en generel analyse af fluktuationsmålingerne og områder med forsvindende fluktuationer identificeres. I den anden del beskrives karakteristikkerne af fluktuationerne i de tre områder omkring X-punktet seperat, og de universelle egenskaber sammenlignes med tilsvarende fluktuationer ved.

I den første del anvendes spektralanalyse til at identificere et område med forsvindende fluktuationer ikke bare på lavfeltssiden, men også på højfeltsiden af det private fluks område, som ikke er blevet reporteret tidligere. De to 'quiescent' områder er observeret både for helium og deuterium plasmaer og ser generelt ud til at være uafhængige af den benyttede opvarmningskilde.

I den anden del viser anvendelsen af den 'filtered Poisson process (FPP)' metoden at den universelle (betingede-forventningsværdi) bølgeform med en stejl front og langsomt aftagende hale fundet ved midt-planet i mange fusions-eksperimenter ikke findes for fluktuationer omkring X-punktet. Istedet har disse en mere symmetrisk form på lavfeltsiden. Yderligere, finder vi at modellerne for både den betingede-forventningsværdi og fluktuations spektret i FPP modellen kan beskrive måledataene fra X-punkt området, når de betragtes individuelt. Tilgengæld tillader de to metoder ikke en forenet beskrivelse, som det er tilfællet ved midt-planet. Denne uoverensstemmelse viser at fluktutionerne omkring X-punktet ikke kan beskrives som en serie af ukorrelerede pulser fra en Poisson fordeling. Ydermere, viser det at de fluktutioner, der opstår ved midt-planet ikke trænger ind i divertor-området, hvor også lokale instabiliteter kan bidrage til spektret af fluktuationer.

Acknowledgment

This work has been carried out within the framework of the EUROfusion Consortium and has received funding from the Euratom research and training programme 2014-2018 and 2019-2020 under grant agreement No 633053. The views and opinions expressed herein do not necessarily reflect those of the European Commission.

I would like to thank my supervisor, Volker Naulin, and co-supervisor, Thomas Eich, for giving me the opportunity to work on this project. I would like to express my appreciation to Jens Juul Rasmussen for his valuable and constructive suggestions, for always taking time to answer my questions and for proofreading my work with great attention. I would like to express my gratitude to Albrecht Herrmann, who made it possible for me to get a probe head for all my measurements, making this project successful and also for his assistance during the experiments. My special thanks goes to Bernhard Sieglin for his support in recommissioning the X-point manipulator diagnostics and helping me with the experimental planning. I owe my thanks to Christian Pfleger for assembling the probe head on time and Pascal de Marné for improving the software of the XPM diagnostics such that stationary measurements were possible. This has been an experimental project and has required the involvement of many more people to make the machine work, therefore I wish to thanks the ASDEX Upgrade team for their contribution. I am thankful to Odd Erik Garcia, Audun Theodorsen and especially Gregor Decristoforo, for taking time to answer my questions related to the filtered Poisson process model. Suggestions given by Matthias Wiesenberger and Anders Henry Nielsen have been of great help in improving the thesis.

On a less academic note, my thanks goes to my office mates and fellow PhD students at DTU for pleasant distractions in the form of coffee breaks and Friday bars. I would like to thank my friends and colleagues at IPP for the data discussions and 'Spielabends'. Finally, I wish to thank my family for their love and encouragement and most importantly to Jakob Gath for his very detailed proofreading of my thesis, for making me dinners so I could write this thesis and for taking care of me when I was struggling.

Raheesty Devi Nem
Section for Plasma Physics and Fusion Energy
Department of Physics
Technical University of Denmark
31 July 2020

Contents

List of Acronyms

Acronym	Full name
ACF	AutoCorrelation Function
ASDEX	Axially Symmetric Divertor EXperiment
CA	Conditional Averaged
CLT	Central Limit Theorem
D−T	Deuterium−Tritium
ECRH	Electron Cyclotron Resonance Heating
ELM	Edge Localized Mode
EM	ElectroMagnetic
EQH	Equilibrium reconstruction from CLISTE code
FFT	Fast Fourier Transform
FPP	Filtered Poisson Process
HFS	High Field Side
ICRH	Ion Cyclotron Resonance Heating
I-V	Current (I) -Voltage (V)
JET	Joint European Torus
LCFS	Last Closed Flux Surface
LFS	Low Field Side
MP	Mach Probe
NBI	Neutral Beam Injection
PDF	Probability Density Function
PFR	Private Flux Region
PSD	Power Spectral Density
RF	Radio Frequency
SOL	Scrape-Off Layer
XPM	X-Point Manipulator

Chapter 1

Introduction

At the moment, about 80% of the world's primary energy consumption is generated from fossil fuels, i.e, oil, coal and natural gases [1]. The burning of fossil fuels affects the environment and the climate adversely both locally and globally, due to the release of greenhouse gases and 'poisonous' particles [2]. It is therefore desirable to replace fossil fuels by alternative energy sources [3]. In recent years many new ways for producing 'green' energy have appeared, e.g., wind, solar hydro and so on. However, while important they do not scale easily. One candidate that does scale is fusion. Fusion does not produce greenhouse gases and compared to fossil fuels, which are exhaustible, there is a sufficient amount of fuel in seawater to fuel fusion reactions for ages. It can even be extracted at low cost. Only a small amount of fuel is needed to operate a fusion power plant and with the current fuel reserve, energy produced by fusion can supply the world's demand for millions of years. Another advantage of a fusion reactor is that there is no concept of nuclear meltdown, as is the unfortunate case for *fission* power plants. For fusion processes to take place fuel has to be continuously fed into the fusion reactor. The amount of fuel present in a fusion reactor is very small compared to a *fission* reactor, where the energy production is sustained by chain reactions in a huge amount of fuel at any instant. The low fuel-mass present in a fusion reactor makes it impossible for meltdown to occur [4].

However, as of now none of the current fusion devices are actually producing a net surplus of energy as it is extremely challenging to confine the hot plasma (the fourth state of matter) for sufficiently long time to be able to make a surplus of fusion power. The three major requirements for fusion reactions to take place in a fusion reactor are: very high temperatures (in the range of 150 million degrees Kelvin), a large-magnetic field ($\approx$ 2 - 6 T) and high-current superconducting magnets ($\approx$ 1 MA), and lastly materials with low activation. Each has its own technical complications and challenges. The single most important challenge that affects almost all aspects of realizing a fusion device is materials. Materials of the wall of the fusion devices must both be able to withstand extreme high heat loads while having low-activation. As it turns out, there are only very few candidates for such materials. The development and maintenance of such components makes a fusion

reactor a complex and costly facility. Furthermore, materials for the structures of the wall must have low-activation such that they can tolerate a high heat load and bombardment of high energy neutrons. ITER is a new fusion device that is designed to demonstrate the possibility to produce more energy than it will need to heat the plasma [5]. The goal for ITER is to resolve critical scientific and technical issues. However, it is not designed to produce electricity. ITER is projected to produce 500 MW of fusion power from an input power of 50 MW. If ITER successfully demonstrates a net surplus power, the next step will be DEMO - a demonstration fusion power plant that will produce electricity to the grid.

Another key challenge in the realisation of fusion power is the confinement of the plasma and this is limited by the energy loss of the plasma to its surroundings [6]. Thus, this energy loss is compensated by the fusion energy yields which is used to maintain reaction conditions. The classical transport due collisions, i.e., particles and energy transport without considering any instabilities, has been calculated and experimental observations in the last decades showed that the rate of energy loss is faster than the theoretical values. The disagreement between the experimental and theoretical value is now known to be due transport mediated by turbulent fluctuations, which is referred to as 'anomalous' transport. As mentioned above, the lifetime of plasma facing components (wall materials) is one major issue and the anomalous transport enhances the plasma-wall interactions. Research of the past decades shows that part of the problem lies with the filamentary structures created in the edge of the plasma due to the interchange instability. The radial interchange motion, caused by the ballooning effect on the LFS and the parallel pressure gradient, ejects these filamentary structures into the SOL where turbulence-driven transport results in broad plasma profiles [7] and increases the level of plasma-wall interactions. In fusion devices different kind of fluctuations are observed, however their relationship to the observed anomalous transport is still not fully clarified [8]. Turbulence induced transport seems to be inevitable and it is yet another important and challenging issue that needs to be understood to be able to optimize the fusion devices.

To get more insight of the turbulence-induced transport, this work focuses on fluctuation studies in the X-point region using conducting wires known as Langmuir probes. In simple words, the X-point is the point at which the poloidal magnetic field has no magnitude. Measurements in the X-point region is crucial as the mere presence of the X-point influences filamentary structures and the turbulence in the scrape-off layer (region of 'open' magnetic field). Many studies have been carried out at the mid-plane and at the divertor of a tokamak to understand, for example, the convective transport by filamentary structures [7], the effects of collisionality and magnetic geometry on the edge turbulence [9], the properties of the filamentary structures [10–12] and many more. Concentrating only on the filaments at the outboard mid-plane, studies of filamentary transport have been carried out for various machines and there is a vast literature related to the dynamics of these filaments which, to a large degree, have been characterized. In particular, the filtered Poisson process model, developed based on the outboard mid-plane observations, has proved to be a useful method in unifying the characteristics of these filaments across different fusion devices [13]. The story is quite different for the X-point region. Even though significant

progress in comprehending the scrape-off layer physics has been made several uncertainties still remains, which among other issues is due to lack of measurements around the X-point. In large, the effects of the X-point as the plasma streams down from the mid-plane towards the divertor is not well understood.

In this thesis, we investigate the characteristics of the fluctuations close to the X-point region and compare the findings with existing literature at the outboard mid-plane. In particular, the filtered Poisson process model which has proven to work well for characterizing the fluctuations at the outboard mid-plane has been tried on fluctuations around the X-point region, in order to determine whether they exhibit the same universal features. In this chapter, sections 1.1 and 1.2 introduce the basic principles of fusion reactions and tokamaks, respectively. The different regions in a tokamak, e.g. scrape-off layer, divertor and X-point are defined in section 1.3. Section 1.4 gives a brief overview of the possible types of turbulence that occurs around the X-Point and in the divertor region. The Langmuir probe method used to determined the relative fluctuation level locally below the X-point is outlined in section 1.5.

The experimental measurements have been carried out at ASDEX Upgrade tokamak. The X-point manipulator at ASDEX Upgrade increases the diagnostics coverage in the poloidal plane and thus, making it possible for local measurements just under the X-point. The experimental setup is described and illustrated in chapter 2. The methodological approaches used to analyze the measurements are introduced in chapter 3. Synthetic data are generated to investigate the behaviour of the filtered Poisson process model and this study is presented in chapter 4. The analyzed measurements are discussed in chapter 5. The conclusion in chapter 6 summarises the key findings of this work and in chapter 7 we give an outlook.

1.1 Nuclear fusion

Fusion is the process of combining two or more light nuclei together to form a heavier nucleus. There are various fusion reactions that may occur. The ones of most interest

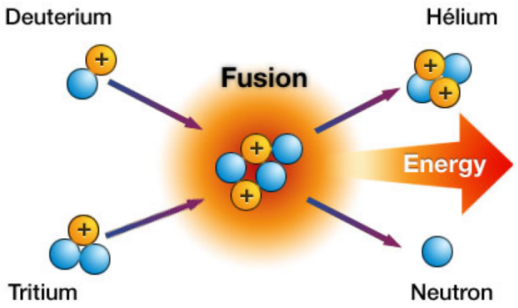

Figure 1.1: The fusion of deuterium and tritium forming a helium atom and releasing a neutron and 17.6 MeV. Taken from [14].

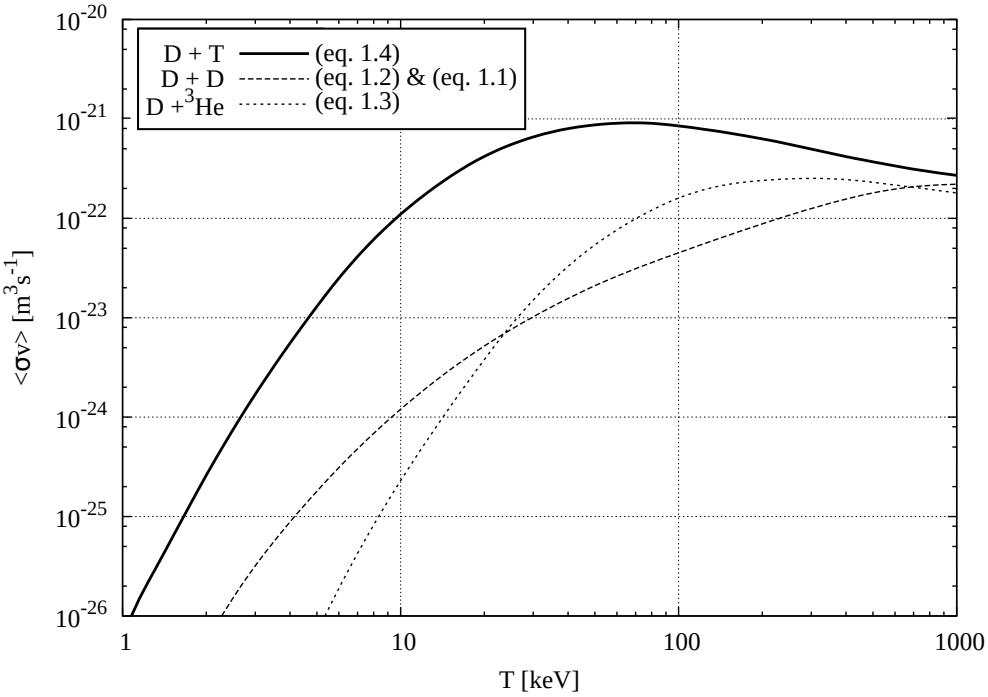

Figure 1.2: The rate coefficient of different fusion reactions as a function of temperature. Adapted from [15].

for laboratory plasma fusion are the ones involving helium (He), deuterium (D) and tritium (T). These reactions are listed as follows:

$$\mathrm{D} + \mathrm{D} \rightarrow \mathrm{He}_2^3 + \mathrm{n} + 3.3\,\mathrm{MeV}, \tag{1.1}$$

$$\mathrm{D} + \mathrm{D} \rightarrow \mathrm{T} + \mathrm{p} + 4.0\,\mathrm{MeV}, \tag{1.2}$$

$$\mathrm{D} + \mathrm{He}_2^3 \rightarrow \mathrm{He}_2^2 + \mathrm{p} + 18.4\,\mathrm{MeV}, \tag{1.3}$$

$$\mathrm{D} + \mathrm{T} \rightarrow \mathrm{He}_2^4 + \mathrm{n} + 17.6\,\mathrm{MeV}. \tag{1.4}$$

The most promising reaction for use in a fusion power plant is that of deuterium and tritium (see eq. (1.4)), because it has the highest reaction cross section at the lowest energy. For experimental investigation, D is also used as fuel, where 50% of the reactions are due to equation (1.1) and the other half are due to equation (1.2). Figure 1.1 shows an illustration of D-T fusion and figure 1.2 provides the rate coefficient $\langle \sigma v \rangle$, for different fusion reactions as a function of the temperature. It is seen that the equation (1.4) proves to be the most favourable reaction as it has the largest rate coefficient at lowest temperature compared to the other reactions. The optimal rate coefficient of the D-T reaction is approximately 10^{-21} $\mathrm{m}^3\mathrm{s}^{-1}$ at 70 keV.

Tritium has a half-life of approximately 12 years, which means that for a specific given amount of tritium, half of the atoms undergo radioactive decay in 12 years. Tritium occurs throughout the environment and can mostly be found in the form of tritiated water rather

than in its natural state [16]. Tritium can be bred from lithium using the neutron released by the D-T reaction (eq. (1.4)). Mainly, two lithium isotopes are of interest, giving rise to the following reactions:

$$\mathrm{n} + \mathrm{Li}_3^6 \rightarrow \mathrm{He}_2^4 + \mathrm{T} + 4.8\,\mathrm{MeV}, \tag{1.5}$$

$$\mathrm{n} + \mathrm{Li}_3^7 \rightarrow \mathrm{He}_2^4 + \mathrm{T} + \mathrm{n} - 2.5\,\mathrm{MeV}. \tag{1.6}$$

Lithium-6 is a good candidate for tritium breeding together with neutron-multipliers such as beryllium. As seen in equation (1.6) the neutrons are used up during the tritium breeding, making neutron-multipliers necessary. Even though a neutron is released during the tritium breeding, Lithium-7 is not suitable due to the small reaction cross section. Deuterium and lithium are abundant on our planet, providing almost inexhaustible sources for fusion [17].

In order for the fusion reactions to occur, temperatures of around 150 million degrees Kelvin are needed. At such temperatures the atoms are fully ionized and the fuels (i.e, D and T gas) are in the state of plasma. There is no solid material that can withstand such temperatures. Therefore, it requires that the plasma does not have direct contact with the device containing it. Since the plasma consists of ionized particles, it can be confined by magnetic fields.

There are several fusion devices, the simplest approach is a linear configuration such as a pinch. In a pinch, an electrically conducting filament is compressed by magnetic forces. Unfortunately, the pinch has large end losses and therefore the particles are not confined. Alternatively, these end losses can be optimized by a toroidal geometry but a simple toroidal system is unstable due to interchange instability and $\mathbf{E}\times\mathbf{B}$ drift that arises [18]. Therefore, the magnetic field lines are twisted helically by a toroidal plasma current to prevent charge separation and thereby, suppresses the $\mathbf{E} \times \mathbf{B}$ drift, creating a tokamak. Experimental research of tokamak devices started in 1956 in the Kurchatov Institute, Moscow, by a group of Soviet scientists led by Lev Artsimovich [19]. The group constructed the first series of tokamaks, the most successful being T-3.

Another major concept for magnetically confined plasma is the stellarator [20]. This concept was introduced by Lyman Spitzer where he proposed to twist the torus into a figure 'eight'-resembling shape such as to introduce the rotational transform in a toroidal configuration. Both the tokamak and the stellarator concept were developed in the 1950s and the current leading concept is the tokamak. The next section introduces the working principle of a tokamak.

1.2 The tokamak device

One of the most advanced fusion confinement concepts is the tokamak [21]. In the following section the basic principles of a tokamak will be described. The tokamak is a magnetic confinement concept with a torus shaped vacuum vessel, which contains the plasma. The tokamak consists of three sets of magnetic field coils [3], as shown in figure 1.3.

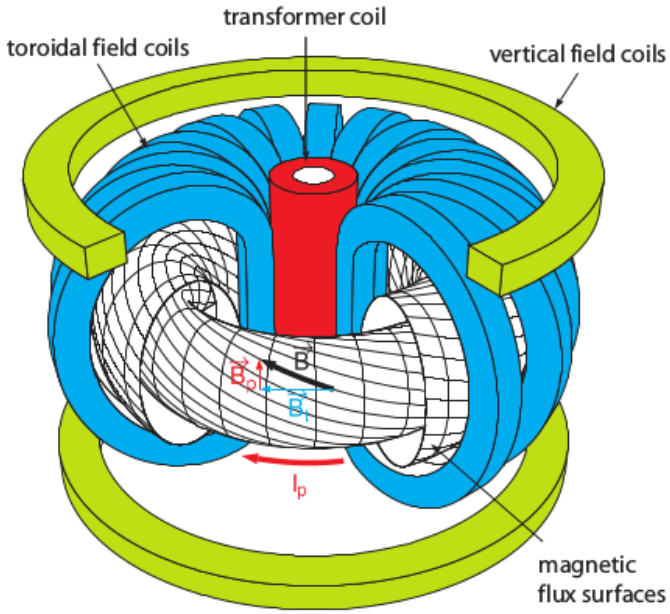

Figure 1.3: Schematic view of the tokamak principle, consisting of three sets of magnetic field coils. Taken from [15].

1. The first set of coils are the toroidal magnetic field coils (shown in blue). As stated in the name, these coils produce a toroidal magnetic field, B_{T}.
2. The poloidal field coils are shown in green and they create a vertical magnetic field, known as the poloidal magnetic field B_{p}. These are used for the control of the position and shape of the plasma.
3. The third component of the magnet system is the central solenoid, which is essentially a large transformer. By changing the current in the central solenoid a toroidal electric field is induced, which leads to the formation of the toroidal plasma current, I_{p}. The plasma current creates the poloidal magnetic field. The combination of the toroidal and poloidal magnetic fields confines the plasma. The confinement of the plasma is described by the force balance: $\mathbf{j} \times \mathbf{B} = \nabla \mathrm{p}$, where $\boldsymbol{j}$ is the current density, p is the pressure and $\boldsymbol{B}$ is the magnetic field.

1.3 Scrape-off layer and divertor

When a tokamak is operated in a magnetic coil setup as described in section 1.2, there will be a point where the poloidal magnetic flux surface starts touching the wall and limits the extend of the plasma. This scenario is shown in figure 1.4 (a) and is called the *limiter* configuration. In this illustration the wall itself is acting as the limiter. Apart from the wall, there are other types of limiters, such as bell limiter. The confined plasma in the limiter

configuration touches the tokamak wall. The poloidal magnetic field in limiter tokamaks is created by the plasma current. The last magnetic flux surface that does not touch a limiter or any solid surface is known as the last closed flux surface (LFCS). This is represented by the black line in figure 1.4 (a). For a long time most of the fusion devices (e.g JET, Tore Supra) were operating with limiters. In this configuration the plasma quickly reaches the wall and recombines into neutral gas, which then lead to erosion of the wall. Due to the proximity of the center of the plasma and the wall, the eroded particles easily reached the confined plasma and increased the impurity content. The high impurity content dilutes the fusion fuel and leads to poor plasma confinement.

To decrease the impurities in the main plasma a different magnetic configuration was developed known as the divertor configuration. In this configuration the distance between the wall and the confined plasma is increased by placing, in addition to the limiter configuration, extra external poloidal field coils above and below the plasma. These are illustrated in green in figure 1.4 (b) and (c). The electric current of the external coils is running parallel to the plasma current, inducing an additional poloidal magnetic field that leads to a reduction of the poloidal magnetic flux surfaces between the plasma and the coils. When the current is sufficiently strong a new magnetic topology is obtained (fig. 1.4 (b)), where a poloidal magnetic flux surface is reduced to zero. This configuration creates an X-point, which is a point in the poloidal plane where the plasma current and the external coil current creates a null in the poloidal field. Increasing the current in the divertor coils even more moves the X-point closer to the confined plasma. Consequently the confined plasma does not touch the limiter anymore and thus creates the divertor configuration as shown in figure 1.4 (c).

The magnetic flux surface that passes through the X-point separates the confined plasma from the unconfined region. This magnetic flux surface is called the separatrix or LCFS. The plasma, shown in light blue colour, outside the separatrix called the scrape-off layer (SOL) follows the magnetic field lines and reaches the divertor region. The region limited by the two separatrix legs below the X-point (see fig. 1.4 (c) in dark blue) is called the private flux region (PFR).

Compared to an open divertor, a divertor with higher closure is able to hold a higher neutral gas pressure which is favourable for helium pumping and divertor detachment. This means that the plasma energy and momentum is dissipated by atomic processes before reaching the divertor targets plates. For future fusion devices, such as ITER and DEMO, a closed divertor configuration is preferable because of the following advantages:

- Reduction of impurity transport of the ion-sputtered particles to the main plasma. Thus, improving the energy confinement.
- The divertor is used to pump out helium 'ashes'. Helium is unavoidably produced as a contaminant in D-T fusion and must be removed to avoid fusion fuel dilution.

However, in the divertor configuration the power reaches the targets in a narrow toroidal line, known as the strike line, hence decreasing the plasma-wetted area compared to the limiter configuration. The plasma-wetted area is a few mm around the strike line. This

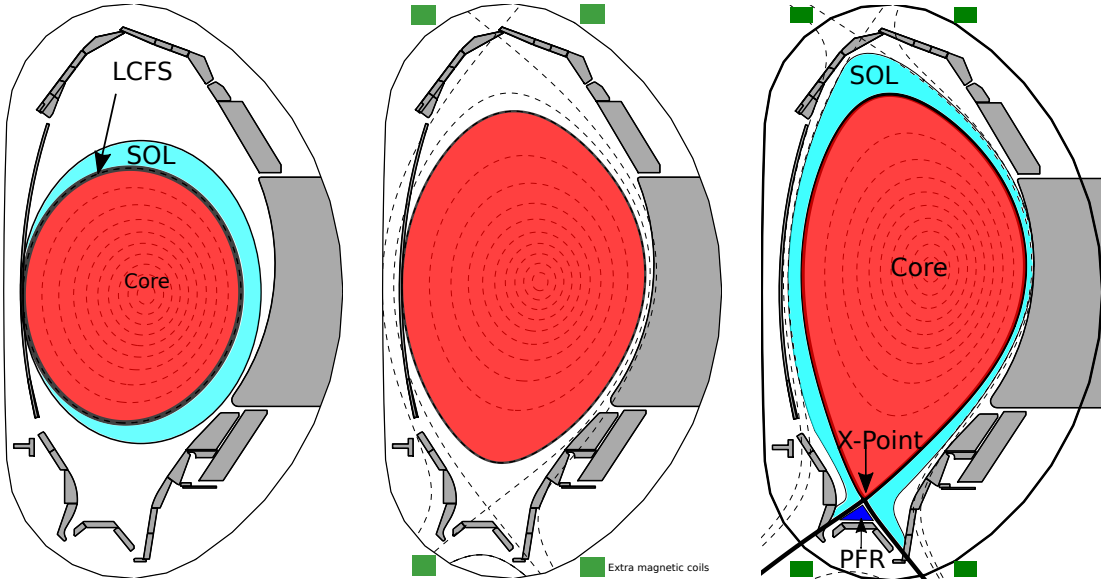

(a) Limiter configuration

(b) Limiter configuration with divertor coils

(c) Divertor Configuration

Figure 1.4: (a) shows the limiter configuration, (b) shows the limiter configuration with divertor coils currents and (c) the divertor configuration. Courtesy of B. Sieglin [22].

localized energy deposition is one the challenges in fusion research as it limits the number of materials that can be used as they have to be able to withstand the power deposition without changing their properties and without sputtering.

The most viable materials that can handle the high temperatures and heat fluxes in the divertor are tungsten and carbon. Carbon, however has the disadvantage of fusion fuel retention as it has a high affinity for hydrogen [23–25].

When the divertor was introduced in ASDEX Upgrade tokamak, a formation of a transport barrier at the plasma edge was found. This regime was termed the *high-confinement mode*, H-mode [26]. The transport barrier is a visible steepening of the plasma density profiles in the edge region of the plasma that results in a higher pressure at the magnetic axis. This phenomenon is associated with the suppression of small scale turbulence. To explain the formation of the transport barrier in fusion devices, the $\mathbf{E} \times \mathbf{B}$ velocity shear model was developed. Experimental results shows that the $\mathbf{E} \times \mathbf{B}$ velocity shear suppresses turbulence and transport in both the plasma edge and core. However, due to its complexity and lack of measurements the mechanism behind the formation of the $\mathbf{E} \times \mathbf{B}$ shearing is not fully understood [27–30]. ITER is foreseen to operate in H-mode as compared to the Low-confinement mode (L-mode), the core density is large for a longer time and this leads to a better plasma confinement.

1.4 Turbulence

A smooth laminar flow in homogeneous fluids are stable to small perturbations when certain conditions are met. One such such condition is the Reynolds number R, defined as $R = VL/\nu$ where V and L are the characteristic velocity and length of the flow and ν is its viscosity, should not exceed a critical value for stable flow. If the condition is not satisfied the perturbation can grow until a new equilibrium is reached. The new equilibrium can become unstable to other perturbations such that the flow is then a superposition of many nonlinear interacting perturbations with nearly random phases. This creates a state of nearly chaotic fluctuations that is termed to be turbulence. Even though a turbulent flow exhibits chaotic behaviour, not every chaotic flow is necessarily turbulent. An example is a jet trail, whose flow is highly chaotic but not turbulent as the shape of the trail is maintained for a long distance behind the jet. A chaotic system has a certain degree of freedom and its solution is very sensitive to the initial conditions. For a system to be called turbulence it has to fulfill other properties which are going to be highlighted in this section. The phenomenon of turbulence occurs in most fluid flows in nature and is therefore of interest to most engineering applications. Water currents below the surface of the oceans, for example the Gulf stream, are turbulent. The stochastic nature of the motions in the photosphere of the sun is observed to be in a turbulent state [31]. The wakes of ships and aircrafts are in turbulent motion. Turbulent flows can be observed in many daily life situations. An example is shown in figure 1.5. Near the wick of a recently extinguished candle, the smoke arises in an orderly manner (laminar flow) and as the smoke rises it turns into a swirling motion exhibiting turbulent flow. These examples along with plenty more, show that the study of turbulence is an interdisciplinary activity. Even though the study of turbulence dates back to 1883 (O. Reynolds pipe flow experiments), there is no precise definition of turbulence. However, fully developed turbulent flows often shows the following characteristics [32]:

- *Fluctuations*: A characteristic of a turbulent flow is that it carries fluctuations in the dependent-field quantities (e.g density, temperature, etc) even when the flow's boundary conditions are steady. Turbulent fluctuations seems to be irregular, chaotic and random. Thus, a deterministic approach to turbulence problems is impossible.
- *Vorticity*: Turbulent flows are characterized by fluctuating vorticity $\boldsymbol{\omega}$ which are identifiable whirl like structures called vortices. The vorticity is the curl of the velocity vector $\mathbf{v}$ and can be expressed as $\boldsymbol{\omega} = \nabla \times \mathbf{v}$.
- *Dissipation*: Turbulence is essentially dissipative, i.e, the kinetic energy is converted to heat. If no energy is supplied to the system, depending on the Reynolds number, the turbulence can decay rapidly.
- *Diffusivity*: Diffusivity of turbulence causes rapid mixing and increases rates of momentum, heat and mass transport.

In fusion devices, such as the tokamak, the plasma transport is now known to be dominated by turbulent mediated transport. While classical and neo-classical transport are important

Figure 1.5: The smoke from a recently extinguished candle exhibits laminar flow near the wick and higher up, interactions with randomly moving air molecules break the flow into turbulence. Taken from [33].

in some regimes, in hot plasmas turbulent transport is dominant since the collision frequency decreases with increasing temperature. In tokamak plasmas, the transport of heat and particles happens faster than expected from classical theory, indicating the presence of turbulent processes. Turbulence causes fluctuations in the plasma parameters (e.g density, temperature and electric field) and it is believed to be the cause for the observed transport losses. In tokamaks, the turbulence is driven by a number of instabilities. In the following sections, those relevant for the presented work, are discussed.

1.4.1 Kelvin-Helmholtz instability

The Kelvin-Helmholtz (K-H) instability occurs at the interface between two parallel inviscid incompressible fluid streams with different velocities. The interface is a shearing layer, as it corresponds to a rapid change in velocity across the interface. The vorticity is approximately uniform in this shear layer, but vanishes on each side of the layer as the velocities become uniform. Hence, a shearing layer appears as a vortex sheet inside an irrotationnal flow. An external perturbation can cause the vortex sheet to start oscillating. This happens when the pressure in concavities is larger than pressure in convexities resulting in a growing amplitude of the oscillations. This results in a tautening of the interface and results in a phenomenon where the interface rolls up, in the direction corresponding to the vorticity direction of the mixing layer. The mixing layer is the interaction between the two fluids. Instabilities of this kind occurs frequently in nature. An example is cloud formation shown in figure 1.6, where the upper layer of hot air is moving faster than the cold air in the lower layer. The vortices formed causes the top cloud layer to roll into the wave-like structures and the vorticity, as a vector $\mathbf{i}$ perpendicular to the plane, can be seen to be to the right. The K-H instability leads to increased heat, momentum and moisture transport in the atmosphere.

Figure 1.6: Atmospheric observation of Kelvin-Helmholtz instability. Taken from [34].

1.4.2 Interchange instability

The interchange instability can be observed in magnetohydrodymanic fluids and can be seen as the generalization of the Rayleigh-Taylor instability known from neutral fluids. Originally, the Rayleigh-Taylor instability occurs in systems where there is an interface between a heavy fluid (e.g water) resting on a lighter fluid (e.g oil). A perturbation of the interface leads to ascending oil blobs and descending water blobs. Compared to the Rayleigh-Taylor instability, gravity is negligible in laboratory plasmas and the perturbation arises instead from the diamagnetic drift. In laboratory plasmas, an interchange instability occurs because the magnetic field can act as an interface separating light fluid (low density plasma) and a heavy fluid (high density plasma).

The pressure gradient in a tokamak causes a diamagnetic current, $\mathbf{j}^{dia} = -\frac{\mathbf{B}\times\nabla p}{B^2}$, that flows along the disturbed isobar. In a tokamak, the magnetic field strength increases from the outboard side (also known as the low field side, LFS) to the inboard side (known as the high field side, HFS) and therefore the gradient of the magnetic field is directed towards the inboard side as shown in figure 1.7. The diamagnetic drift, however, decreases with increasing magnetic field strength resulting in charge accumulation. A $\mathbf{j}^{dia}$ vector pointing towards the LFS, gives rise to negative charge accumulation while a $\mathbf{j}^{dia}$ vector pointing towards the HFS gives positive charge accumulation. This results in charge separation which in turn gives rise to an electric field and the $\mathbf{E}\times\mathbf{B}$ drift. The $\mathbf{E}\times\mathbf{B}$ drift amplifies the disturbance in one case and stabilises it in another. If the pressure gradient and the gradient of the magnetic field are in opposite directions the perturbation is stabilized by the magnetic field, hence defining the 'good curvature' side (see the scheme in figure 1.7 (a)). However, if the directions of both gradients are same this leads to the amplification of the instability, therefore the 'bad curvature' side (fig. 1.7 (b)).

1.4.3 Drift-wave instability

Drift-wave instabilities can arise in any arbitrary magnetic field configuration. Figure 1.8 illustrates the drift-wave mechanism. A homogeneous magnetic field $\mathbf{B}$, perpendicular to the equilibrium density n_0 is considered. The density is perturbed by a sinusoidal density

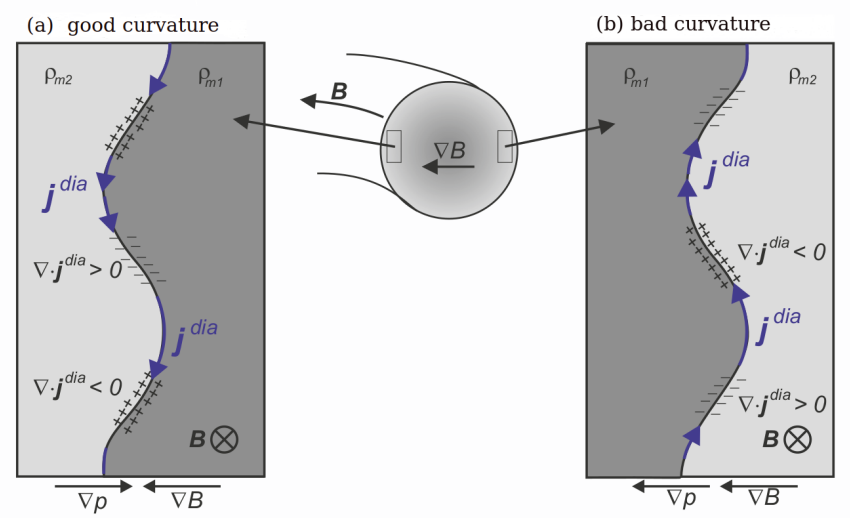

Figure 1.7: Stability of interchange modes in two configurations. When the pressure gradient is antiparallel (a) and parallel (b) to the gradient of the magnetic field. The latter destabilizes the instability. Adapted from [35] pg. 119.

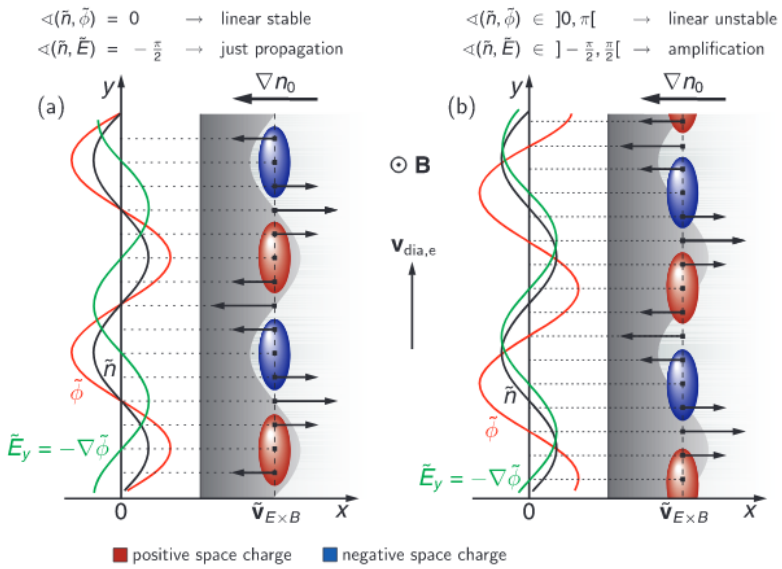

Figure 1.8: Mechanism of linear drift-wave instability in the local slab geometry. (a) for *adiabatic* electrons showing a linearly stable situation and (b) for non-adiabatic electron which leads to the amplification of the initial perturbation. Taken from [36] pg 6.

oscillation (shown by the black curves). It is important for the dynamics of the drift-wave turbulence that the electrons with thermal speed react to the parallel pressure gradient and causes the charge distribution as shown, i.e, the ions create positive charge in regions of positive density perturbation and vice versa for the electrons. An electric field arises naturally from the charge separation and it is perpendicular to the magnetic field. Thus, it results in $\mathbf{E} \times \mathbf{B}$ drifts (green curve) that have the same speed as the diamagnetic drift of the electrons. For adiabatic electrons, the density and potential perturbations are in phase, as shown by the red and black curve in figure 1.8 (a). Adiabatic electrons are those that react immediately to the parallel pressure gradient and creates an equilibrium with the parallel electric field. The $\mathbf{E} \times \mathbf{B}$ drifts are shifted by $\pi/2$ relative to the density and potential perturbations and cause the perturbation to drift downwards (therefore the name: drift-wave). For adiabatic electrons there is no net radial transport and hence the amplitude of the perturbation is not suppressed, making the perturbation stable. The drift-wave is unstable when the electrons do not respond immediately to the perturbation, i.e, they are non-adiabatic. The delayed parallel dynamic causes a lag in the propagation of the potential perturbation relative to the density propagation. The cross-phase between the potential and density increases and the $\mathbf{E} \times \mathbf{B}$ drifts have a phase shift of less than $\pi/2$ relative to the density (fig. 1.8 (b)). As a consequence, the non-adiabatic electrons cause a net transport radially and the $\mathbf{E} \times \mathbf{B}$ drifts amplify the initial perturbation. Hence, resulting in an unstable propagating drift-wave.

1.5 Fluctuation measurements

As discussed in previous section, the anomalous transport in tokamaks is now known to arise from turbulent transport caused by fluctuations in the plasma. To understand the turbulence in tokamaks it is, therefore, important to characterise the fluctuations of the different quantities like density fluctuations, electric field, temperature, plasma potential and so on. There are different methods for measuring fluctuations such as probes-, scattering-, spectroscopy-, reflectometry- diagnostics and many more [37–39].

A common way of performing fluctuation measurements is by using Langmuir probes. This is the method used to obtain fluctuation measurements in this thesis. The theoretical background of the Langmuir probe and its different operation modes are given in the following section.

1.5.1 Langmuir probe theory

In its simplest form, a Langmuir probe consists of a single electrode of radius a inserted into the plasma. One way of operating a Langmuir probe is to sweep it, i.e, to vary the voltage over time. A sweeping voltage is applied to the probe with respect to the grounded vessel. When performing measurements the current and voltage is simultaneously measured. From the current-voltage (I-V) characteristics of such a probe the plasma parameters can be deduced. From the I-V characteristics one can estimate the effective ion-saturation current $I_{\mathrm{sat,eff}}$, the floating potential V_{float} and the electron temperature T_{e} by the following

equation [8]:

$$I_{\text{probe}} = A(I^{+}_{\text{sat}} + I^{-}_{\text{sat}}) = AI^{+}_{\text{sat}} \left(1 - \exp^{\frac{e(V_{\text{probe}} - V_{\text{float}})}{k_{\text{B}} T_{\text{e}}}}\right), \tag{1.7}$$

where I^{+}_{sat} and I^{-}_{sat} are the ion- and electron-saturation current, respectively. I_{probe} and V_{probe} are the measured current and applied voltage, e is the elementary charge, k_{B} is the Boltzmann constant and A is area of the exposed probe surface. The potential, at which the probe current vanishes, is known as the floating potential V_{float}. The model (eq. (1.7)) describing the I-V characteristics is based on the given assumptions:

- The bulk plasma is homogenenous, stationary and quasineutral ($Zn_i \simeq n_e$) where Z is the ion charge.
- The particles (ion and electron) energy follows a Maxwellian distribution.
- The electron density obeys the Boltzmann factor relation $n_e = n_0 \exp(eV/k_{\text{B}}T_{\text{e}})$, when V is negative such that T_{e} can be deduced from the exponential slope of the I-V characteristics. n_0 is the electron density far from a potential perturbing charge where the plasma potential is null.
- Bohm criterion is valid, i.e., the particles reaches the sheath at ion sound speed c_{s}.
- In the vicinity of the probe the particles are collisionless, i.e, $\rho_i \gg a$ and $\lambda_{\text{mfp}} \gg a$. ρ_i is the Larmor radius and is defined as the radius of the helical movement of the ions around the magnetic field. λ_{mfp} is the mean-free-path and $\lambda_{\text{D}} = \left(\frac{\varepsilon_0 k_B T_e}{n_e e^2}\right)^{1/2}$ is the Debye length which specifies the range of an electrostatic potential in a plasma.
- The sheath is very thin compared to the probe radius, such that the edge effects are negligible. The sheath is defined as a region with a thickness of a few Debye lengths around the probe.

Figure 1.9 shows the ideal I-V characteristic curve of different Langmuir probes geometries, namely planar, cylindrical and spherical. The I-V curve can be separated in three regions:

1. The ion-saturation region, A
2. The electron-retardation / transition region, B and,
3. The electron-saturation region, C

that are now described in turn:

Ion-saturation region

When the Langmuir probe with surface area of A is biased increasingly with a negative voltage with respect to the plasma potential, a point is reached where all the electrons are repelled and eventually only positive ions are collected. This region is called the ion-saturation region. The ion-saturation current I^{+}_{sat} is defined as follows:

$$I^{+}_{sat} = Zn_{\text{i}} e c_{\text{s}} A, \tag{1.8}$$

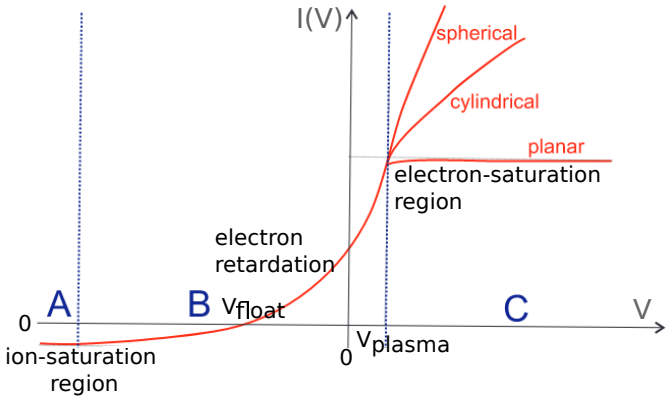

Figure 1.9: shows the ideal I-V characteristics of a different Langmuir probe. Adapted from [40].

where n_i is the local ion density, Z is the ion charge, e the elementary charge and the ion sound speed is $c_\mathrm{s}^2 = \left(ZT_\mathrm{e} + \gamma T_\mathrm{i}\right)/m_\mathrm{i}$. T and m are the temperature and mass of the species. The subscripts i and e represent the ion and electron species, respectively. γ is the adiabaticity parameter.

Transition region

In this region the probe is still biased negatively with respect to the plasma potential and the probe starts to absorb electrons that are sufficiently energetic to cross the potential barrier of the applied voltage. This region is known as the electron-retardation or transition region as most of the impinging electrons are reflected due to the negative voltage. The current I_e increases exponentially at a rate determined solely by the electron temperature T_e shown in figure 1.9. Therefore, the exponential curve of the electron retardation I_e gives the electron temperature and can be described by [41]:

$$I_\mathrm{e} = I_\mathrm{sat}^- \exp^{\frac{e\left(V_\mathrm{probe} - V_\mathrm{float}\right)}{k_\mathrm{B} T_\mathrm{e}}}, \tag{1.9}$$

with k_B being the Boltzmann constant and I_sat^- the electron-saturation current. In this region, a point is reached where there is a balance between the ion and electron current, resulting in a vanishing net current through the probe. At this specific potential V_float the probe is electrically isolated, i.e, it floats.

Electron-saturation region

In this region, the probe is biased positively with respect to the plasma potential V_plasma, causing the electrons to move towards the probe, resulting in electron saturation. Thus the name, electron-saturation region. The electron-saturation of a probe with surface area

A is given as:

$$I_{\rm sat}^{-} = -\frac{1}{4} n_{\rm e} e c_{\rm e} A. \tag{1.10}$$

The electron thermal speed is defined as $c_{\rm e} = (8T_{\rm e}/\pi m_{\rm e})^{1/2}$. If two straight line are drawn, one on the electron-saturation region and the other on the slope of the I-V characteristics, there is a point where both lines intersects. The bias voltage corresponding to the intersection point gives the plasma potential, $V_{\rm plasma}$. This is the potential acquired by an isolated plasma without any magnetic field.

Since the electron velocities are $\approx (m_{\rm i}/m_{\rm e})^{1/2}$ times larger than ion velocities for the same temperature, it is expected that $I_{\rm sat}^{-}$ is much larger than $I_{\rm sat}^{+}$ [8, 41, 42]. Therefore, in magnetized plasma the electron-saturation current is difficult to obtain as the sheath around the probe keep increasing. The electron-saturation will occur at a very high voltage, however, the electronics cannot supply it. For this reason the electron-saturation branch is not observed in strongly magnetized plasmas. Also, drawing an electron-saturation current using a planar probe in a strongly magnetized plasma may excites instabilities. The electron density is instead determined by using the ion-saturation current measured, under the assumption that a strongly magnetized plasma is quasi-neutral, i.e, $Zn_{\rm i} \simeq n_{\rm e}$. The electron density is then [8]:

$$n_{\rm e} = \frac{I_{\rm sat}^{+}}{A\, e} \left(\frac{m_{\rm i}}{2T_{\rm e}} \right)^{1/2}. \tag{1.11}$$

It is not clear how to obtain the plasma potential from I-V characteristics obtained from a strongly magnetized plasma. However, it can be calculated from the floating potential $V_{\rm float}$ and electron temperature $T_{\rm e}$ [8, 42]:

$$\begin{aligned} V_{\rm plasma} &= V_{\rm float} + \alpha T_{\rm e}, \\ \alpha &= \frac{1}{2} \ln \left[\frac{m_{\rm i}/m_{\rm e}}{2\pi \left(Z + T_{\rm i}/T_{\rm e} \right)} \right], \end{aligned} \tag{1.12}$$

where α is a constant that accounts for ions adiabatic cooling in the sheath. Under the assumption that $T_{\rm i} = T_{\rm e}$, α is approximately 2.8 for deuterium plasma and 3.2 for helium-4 plasma.

A second operational mode of the Langmuir probe is to bias the electrode to a large negative voltage relative to $V_{\rm float}$. In this method, the Langmuir electrode measures the $I_{\rm sat}^{+}$ (eq. (1.8)). Since the $I_{\rm sat}^{+}$ is proportional to the density $n_{\rm e}$, biasing the electrode allows the measurement of the density fluctuations. It should be noted that there is in general a dependency on $T_{\rm e}$. However, for equal relative fluctuations of both $n_{\rm e}$ and $T_{\rm e}$, the contribution of the $n_{\rm e}$ is twice compared to $T_{\rm e}$, due to the square-root dependence of the temperature.

A third way to operate a Langmuir probe is by electrically isolating the electrode. This method allows the measurement of fluctuation in the $V_{\rm float}$. From equation (1.12), one can see that the fluctuations in the $V_{\rm float}$ are due to the $V_{\rm plasma}$, $T_{\rm i}$ and $T_{\rm e}$. However, the

T_i is not measured using Langmuir probes. This method has the challenge that there is a scarcity of fast measurements of T_e in cold region of fusion devices. Therefore, it can become difficult to characterise the contribution of the fluctuations from the temperature to that of the plasma potential.

For completion, a way to measure the fluctuation in V_plasma is to heat a Langmuir probe and make it emmissive. These are known as emissive probes [43]. However, one still need to combine data from multiple Langmuir probes in order to obtain the electron temperature. In this work, no data from emissive probes is used.

1.5.2 Mach probe

A Mach probe (MP) is one of the cheapest and easiest probe system that is used to determined the Mach number M from the ion-saturation current measurements [44]. There exist different types of Mach probes:

- Parallel MP
- Rotating MP
- Gundestrup probe
- Perpendicular MP
- Visco-Mach probe

The parallel MP is also simply known as MP. This electric probe system consists of two directional Langmuir probes with an insulator separating them. An example of a MP is shown in chapter 2 (fig. 2.6), where a graphite wall act as an insulator. In this configuration both Langmuir probes are biased at the same negative voltage to collect ions in the parallel direction with respect to the direction of the magnetic field. The ratio of the ion-saturation current measured upstream and downstream is related to the Mach number as given:

$$R = \frac{I_\mathrm{up}}{I_\mathrm{down}} = \exp\left(KM\right), \tag{1.13}$$

where K is a proportionality factor. By taking the logarithm on both sides, the Mach number is evaluated:

$$M = \frac{1}{K} \log\left(\frac{I_\mathrm{up}}{I_\mathrm{down}}\right). \tag{1.14}$$

From Hutchinson *et al.* [45] and Müller *et al.* [46], the proportionality factor K is estimated to be 2. When there is no plasma flow, the Langmuir probe on each side collects equal amount of ion-saturation current due to the probe symmetry and hence resulting in $M = 0$, whereas in the case of a direction plasma flow the Mach number is larger than zero. In this work only the parallel MP has been used. The other types of MPs are beyond the scope of this work and therefore will not be described here. For further reading, the interested reader is recommended the work of Chung *et al.* [44].

Chapter 2

Experimental Setup

In this section, the ASDEX Upgrade tokamak is briefly described together with a short overview of the auxiliary heating systems. In section 2.4 and 2.5, the X-point manipulator (XPM) and the probe head used to collect data are introduced and lastly, the challenges faced during the experimental campaign are discussed.

2.1 ASDEX Upgrade

The **A**xial **S**ymmetric **D**ivertor **EX**periment **U**pgrade (ASDEX Upgrade) has been in operation since 1991 at the Max Planck Institute for Plasma Physics in Garching near Munich, Germany [47]. ASDEX Upgrade is the largest fusion experiment, of the tokamak type, in Germany. It has a plasma volume of around 13 cubic metres and it can operate with a magnetic field strength of up to 3.9 T. The tokamak has a major radius of 1.65 m and a minor radius of 0.5 m. ASDEX Upgrade has three different sources for auxiliary heating [47]:

- Neutral beam injection (NBI)
- Ion cyclotron resonance heating (ICRH), and
- Electron cyclotron resonance heating (ECRH).

ASDEX Upgrade initially started operating with carbon plasma facing components. In 2007, it was the first tokamak to demonstrate operation in a full metal environment with tungsten as first-wall-material [48]. The aim of ASDEX Upgrade is to investigate the behaviour of a magnetically confined plasma in a reactor relevant environment, which is especially important for ITER [5, 49]. Figure 2.1 (a) shows the divertor region of ASDEX Upgrade. Presently ASDEX Upgrade operates with a closed divertor configuration which is illustrated in figure 2.1 (b). At ASDEX Upgrade the divertor is coated with tungsten and consists of a belt of tungsten tiles on the inner and outer target plates at the position of the strike line [24]. The outer divertor is made up of bulk tungsten while the inner targets are made up of fine-grained graphite coated with a tungsten layer to prohibit

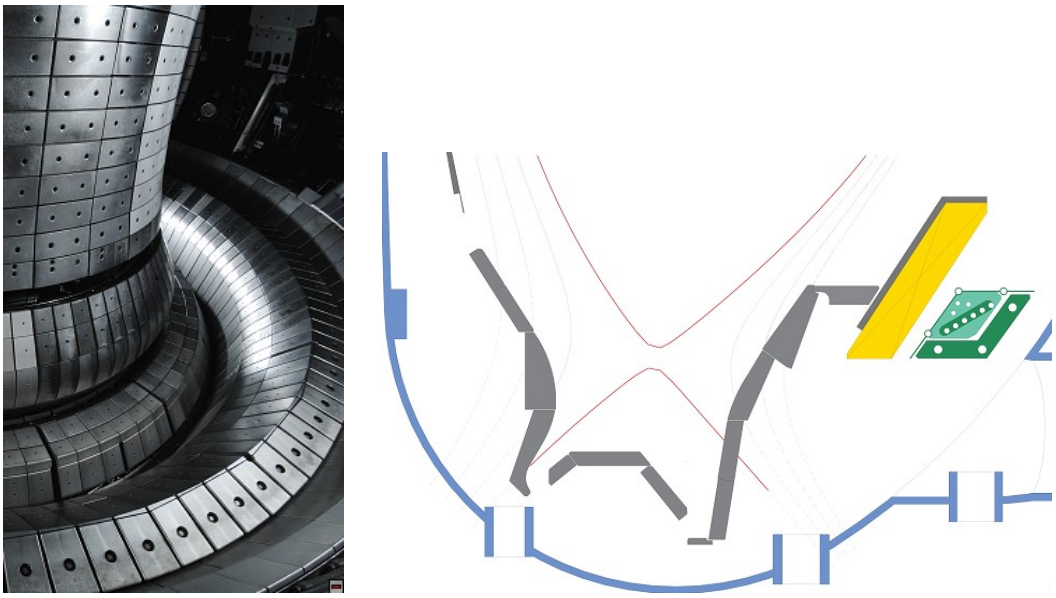

(a) (b)

Figure 2.1: (a) The divertor region in ASDEX Upgrade. (b) The closed divertor sketch of ASDEX Upgrade. Both pictures are taken from [50].

its embrittlement. Targets usually denotes the divertor plates where the power deposition occurs. In the toroidal direction, the divertor targets are slightly inclined to obtain shadow edges to prevent direct power deposition on the edge of the targets. The divertor targets at ASDEX Upgrade are designed to handle a heat load of about 10 MWm^{-2}. This is generally an acceptable limit that can be accommodated and it is used in the design for ITER.

2.2 Neutral beam injection

ASDEX Upgrade is equipped with a NBI system that is able to inject a power of 20 MW into the vacuum vessel. This auxiliary heating system consists of two injectors and works by utilizing the Coulomb-collision mechanism to heat the plasma. When the neutral particles of the NBI collide with the ions or electrons in the plasma, their energy is transferred to the ionized particles thereby heating the plasma. Whether the ion or the electrons are heated depends on the energy of the plasma particles (i.e, electron and ions) and on the initial beam energy. Since the tokamak is a magnetic confinement device, it is impossible to heat the plasma by ion-injection as they will be deflected by the magnetic field before reaching the core of the plasma. As neutrals are unaffected by the magnetic field, they are ideal for delivering the heating power. Figure 2.2 illustrates a schematic of the working principle of the NBI system. Initially a hydrogen (H) or deuterium (D) gas is ionized and these ionized particles are made energetic by accelerating them over an electrical grid. These energetic

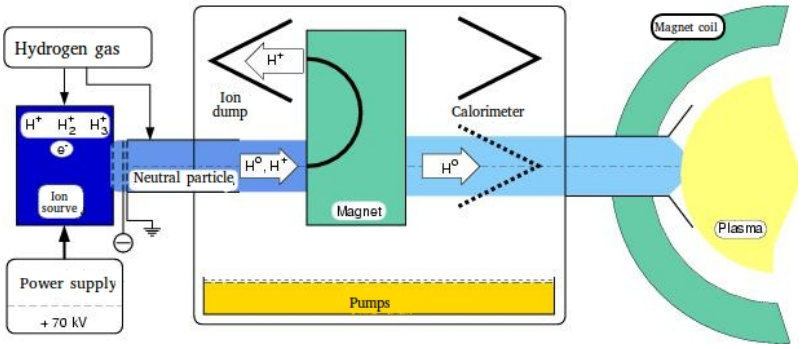

Figure 2.2: Schematic of the neutral beam injection at ASDEX Upgrade. Taken from [3].

particles are neutralized in a component known as the gas target neutralizer [3]. If there are still ions present in the neutral beam, these are then deflected onto ion dumps by a 180-degrees bending magnet. To measure the NBI heating power, a movable calorimeter is mounted in front of the torus duct as illustrated in figure 2.2. The neutral beams are shot into the plasma, where they get ionized, and lose their energy by Coulomb collisions which results in plasma heating. The two injectors of ASDEX Upgrade have four neutral beam sources each and the calorimeter is also used to calibrate these sources. One of the NBI injector can inject particles with energies in the range of 30 keV to 60 keV, while the second box delivers particle energy in the range of 50 keV up to 93 keV.

2.3 Wave heating

ECRH and ICRH are methods for heating a medium at two different frequencies by launching external radio frequency (RF) waves into the plasma. RF waves are electromagnetic waves (EM) occurring in the range of 20 kHz up to 300 GHz. ECRH operates in the high end of this range at 50 - 150 GHz while, ICRH operates at the low end range at 30 - 100 MHz. The cyclotron resonance is inversely proportional to the mass of the species heated. Therefore, ICRH occurs at lower frequencies compared to the ECRH because the ion mass is much larger than the electron mass, i.e., 1/1837. When the applied RF wave matches the resonant frequency of the medium to be heated, the energy of the wave is amplified and converted into heat. The cold plasma model is a reasonable approximation for describing the propagation of RF waves in magnetically confined plasmas, while the absorption of the energy depends on the cyclotron and collisionless Landau damping [4, 8]. The ECRH and ICRH, as implied in their names, rely on resonances with the cyclotron motion of the electrons and ions, respectively. A magnetized plasma allows the propagation of two plasma modes, namely the ordinary mode (O-mode) and the extraordinary mode (X-mode). O-mode waves are those whose electric field are parallel to the background magnetic field while the X-mode waves have an electric field perpendicular to the background magnetic

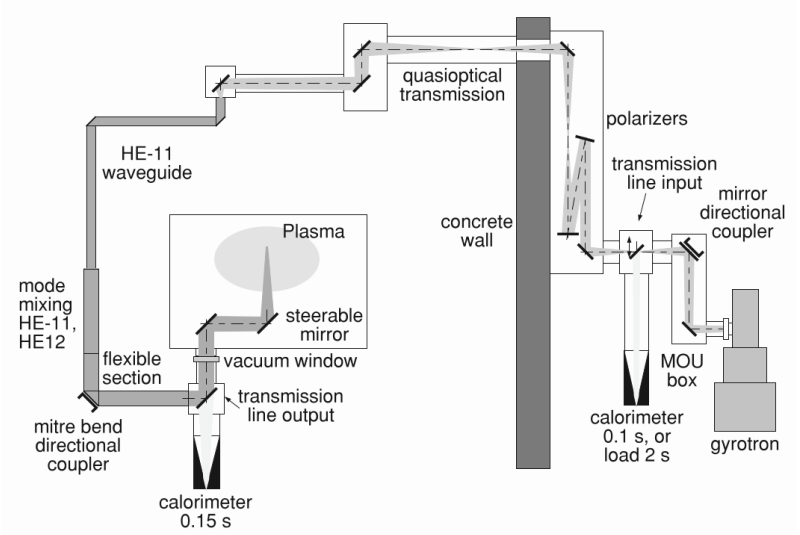

Figure 2.3: Illustration of electron-cyclotron resonance heating system of ASDEX Upgrade. Taken from [51].

field. These two modes obey two different dispersion relations and therefore propagate differently under specific conditions.

2.3.1 Electron cyclotron resonance heating

ECRH allows localized electron heating and current drive in the plasma. The latter can improve the confinement of the plasma and promote long-pulse operation used to study the electron transport. ECRH also have the advantage of being capable of stabilizing neoclassical tearing modes and it allows transitions of confinement regimes such as L- to H-mode. Figure 2.3 illustrate the ECRH heating system of ASDEX Upgrade. The power needed for ECRH heating is generated in the frequency range of the electron cyclotron resonance ($\omega \approx \omega_{c,e} = \frac{eB}{m_e}$) by gyrotrons, in which the EM wave is coupled to the gyrating electrons in a steady magnetic field. The EM wave is amplified by the electrons that are bunched in phase. The power is coupled out of the gyrotrons via wave-guides. ASDEX Upgrade uses a diamond window as interface between vacuum and air because it has the advantage of high thermal conductivity and minimal absorption, which allows edge cooling. The high power EM wave is transmitted via wave guides that have different mode convertors that change the output mode of the gyrotron to the required heating mode (O-mode or X-mode) [52]. At ASDEX Upgrade, the EM waves are transmitted as Gaussian beams by using quasi-optical lines. The power loss during the transmission of the wave is determined by the calorimeters [51]. To deliver the power accurately at the position desired, movable mirrors are installed inside of the vacuum vessel. These are used to change the wave direction and off-axis heating, while keeping the same magnetic field and frequency.

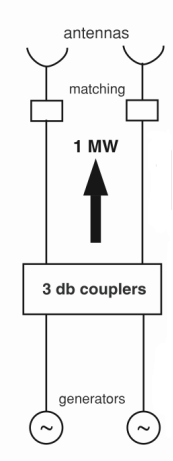

Figure 2.4: Schema of the ion-cyclotron resonance heating system of ASDEX Upgrade. Taken from [51].

2.3.2 Ion cyclotron resonance heating

Some interesting aspects of ICRH, other than just heating, is the possibility of studying fast ions and heating of the particles without input of momentum and refuelling. The power are supplied by four generators at ASDEX Upgrade. Figure 2.4 illustrates the basic components of the ICRH system. Each of the generators are made up of a broad-band-transistor amplifier and an oscillator. The generators can be tuned to deliver a maximum power of 2 MW and the frequency can be adjusted between 30 - 120 MHz such as to be able to heat at different location in the plasma. At 120 MHz the output power decreases to 1 MW. From the generators the power is transmitted to the antenna via coaxial cables. As shown in figure 2.4, two-sub tuner matching system are placed near the vacuum vessel to transform the impedance of the antenna to that of the transmission line and generator output [51]. The matching system behaves as a resonance circuit with high voltage and standing waves. Since the sub-tuner matching system cannot adjust to the antenna impedance during a plasma shot, the power can be reflected back to the system. This reduces the power significantly and can cause the generator to shut down to prevent damage. To avoid the generators shut down, while protecting them as well, the ICRH system is modified by adding two 3 dB couplers. Each of the coupler combines two generators and two antennas as the power reflected from two antennas are roughly the same. Therefore, the reflected power can either be transferred to a dummy load or compensated in a power splitter. Finally, the four antennas in the vacuum vessel couple the power to the plasma.

2.4 X-point manipulator

The X-point manipulator (XPM) in ASDEX Upgrade increases the poloidal diagnostics coverage as shown with the black line in figure 2.5 [53, 54]. The XPM is located in sector

10 at $z = -0.965$ m in ASDEX Upgrade and it reciprocates horizontally below the X-point through the divertor entrance. This provides the unique opportunity to measure in both the LFS, the HFS SOL as well as in the PFR. Figure 2.5 shows an example of a magnetic field equilibrium as reconstructed from the EQH (an equilibrium reconstruction from CLISTE code [55]). The blue line represent the separatrix. Two motors are responsible for the motion of the XPM. The first motor brings the XPM to the experimental position while the second motor is used to make plunges during discharges and therefore moves at a maximum speed of 3 ms^{-1}. After each plunge the XPM is retracted up to the experimental position. A full probe plunge covers approximately 30 cm in the vacuum vessel, starting from the LFS divertor entrance at a major radius of $R_m = 1.645$ m with a maximum insertion distance of $R_m = 1.356$ m on the HFS. To avoid overheating of the probe head a maximum of three plunges per experimental discharges are carried out [46, 56].

2.5 XPM probe description

A probe head consisting of three Langmuir probes was mounted on the XPM during the experimental campaign of 2019. Figure 2.6 (a) shows a picture of the tip of the probe head as seen from above. Figure (b) illustrates the Langmuir probes on the probe head as seen from the plasma and the direction of the magnetic field line striking the Langmuir probes. All the three Langmuir probes are cylindrical graphite probes of approximately 2 mm in length with a diameter of 1 mm. Langmuir probe 1 and 2 are mounted in the Mach-probe configuration and are separated by a 4 mm high and 0.9 mm wide graphite wall (marked by the number 4 in fig. 2.6 (b)). The distance x of probe 1 and 2 from the center of the graphite wall is 1.15 mm, while the distance y of probe 3 to the center of the graphite wall is 2.55 mm. The diameter of the front of the probe head is 10 mm while, the main graphite shaft that holds the probe is 29 mm wide. From the magnetic field direction, Langmuir probe 1 is measuring the upstream plasma while, Langmuir probe 2 is measuring the downstream plasma. The two Langmuir probes are DC biased at a constant voltage of approximately -170 V. Langmuir probe 3 is a freestanding probe which is swept at a frequency of 1 kHz, using a triangular waveform, at a given DC voltage of $\pm$ 130 V and simultaneously the probe current is measured. The voltage of all the Langmuir probes are set by KEPCO bipolar operational power supplies (BOP 100-4M and BOP 200-1M), while the current is measured by current probes from Tektronix (AM503 current amplifier). The MPs are connected in series by two BOP 100-4M such that they can be biased at a voltage of approximately -200 V and a maximum current of 8 A can be measured, while the power supply for probe 3 is the BOP 200-1M, which can provide a maximum voltage of $\pm$ 200 V and a maximum current of 1 A.

The Langmuir probes tend to erode when having plasma contact and therefore the probes have to be changed several times during an experimental campaign. Table 2.1 gives the details about the length of the probes for all the assembly performed during the experimental campaign of 2019.

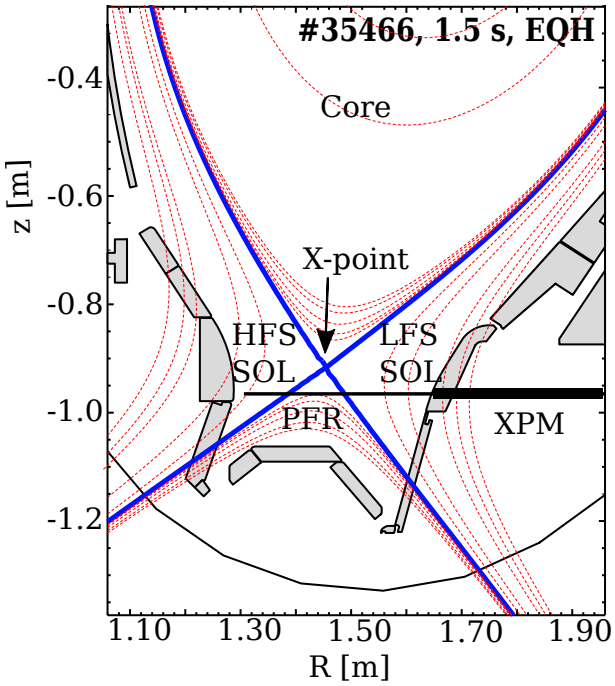

Figure 2.5: Location of the X-point manipulator (XPM) in the divertor region on the poloidal cross-section of ASDEX Upgrade. The X-point is shown by the arrow and the different regions are labelled.

Assembly number	Length [mm]		
	probe 1	probe 2	probe 3
#1	2.7	2.5	2.0
#2	2.4	2.4	2.1
#3	2.1	2.5	2.0

Table 2.1: Details of each probe for every assembly made during the experimental campaign.

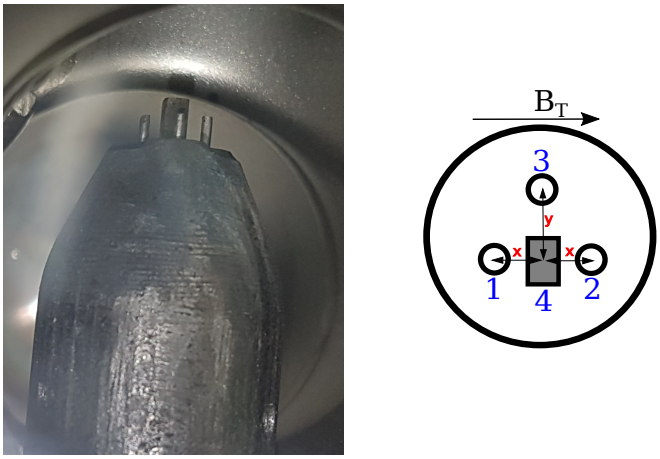

(a) (b)

Figure 2.6: (a) Top-view of the probe mounted on the XPM and (b) sketch of the probe head as seen from the plasma.

2.6 Experiments and challenges

Langmuir probes are cost effective diagnostics and on the other hand intrusive. Since they get in contact with the plasma, they have to be designed such that the probes are neither interfering with the plasma nor damaged by it. However, in hot plasma the Langmuir probes will gradually and eventually erode away. The Langmuir probe theory (see sec. 1.5) is based on a known surface area of the probe and a thin sheath approximation and these make the interpretation of the I-V characteristics laborious. It is challenging to determine the surface area of the Langmuir probe after every experiment or experimental day. To do so, one would have to dismount the XPM-diagnostics completely which is not feasible. Firstly, dismounting the diagnostic makes the probe head prone to accidents like breaking of the Langmuir probes or damaging the probe head itself. This would lead to no experiments until the Langmuir probes are replaced or the probe head is repaired. This could cause a delay of two weeks up to three months depending on the severity of the damage. Secondly, the diagnostics will be removed from vacuum and it takes approximately three days to reestablish the vacuum so that it is safe for plasma operation. This would limit the operation of the XPM. Another challenging issue is the Langmuir probes themselves. They are very delicate, hence it is not easy to make them exactly the same length at every assembly. For single probe operation, variable length of Langmuir probes is acceptable. However, for Mach probe (see sec. 1.5.2) operation one ideally wants both Langmuir probes to be of the same dimension such that both Langmuir probes measure the same magnitude of current. However, as shown in table 2.1, this is usually not the case. For the data analysis to determine the plasma flow using the Mach number, the surface area dependence for both the upstream and downstream ion-saturation current has to be taken into account.

While planning the experiments it has been essential to estimate the risk of operation. The

XPM was not operated when the following were foreseen in an experiment:

1. Plasma disruption or high probability of disruption to occur
2. Pellets (frozen hydrogen) for plasma fuelling
3. High power H-mode
4. ELM (Edge-localized mode) production in the range of 10 Hz
5. NBI-blips (pulses of NBI power)
6. ICRH at a frequency of 55 MHz

The first five key points cause large currents during experiments and in addition NBI-blips create torque in the plasma while ELMs release a large pressure which together with the current changes the magnetic equilibrium. A large torque or current, especially during a disruption can damage the XPM. The 30 cm long shaft holding the probe could break-off or be bent. The XPM reciprocates in and out of the plasma via a 30 mm wide entrance in the divertor. If the XPM shaft is bent, it can become tremendously difficult to retract it out of the vacuum vessel. In extreme case, the vacuum vessel would have to be opened to remove it. In the case of ICRH operation at 55 MHz, reflected waves have been triggering the safety switch of the XPM which resulted in a premature plasma shutdown. Before planning a experiment, it is vital to choose a magnetic configuration in which the XPM is always below the X-point, as otherwise the XPM will be in the confined region where the temperature is much higher than in the SOL or PFR. Piggy-back measurements were carried out in H-mode and high-density plasmas close to the X-point, however, the electronics could not hold the voltage and a voltage break-in was observed in the measurements. In most cases, the current also went into saturation, i.e, the current measurement reached the maximum limit of the electrical system. Due to the large potential applied on the Langmuir probes arcing is very often observed in the L-mode plasmas. Arcing can cause the erosion of the Langmuir probes. An 'arc detector' is built into the electrical circuit such that when a current threshold is exceeded, the power supply will switch-off for 2 or 10 ms before reconnecting to the circuit. In several shots arcing was observed the closer the probe head was to the X-point. Hence, making the X-point region a harsh environment for probe measurements. Therefore, the dedicated shots (during the 2019 experimental campaign) were carried out only in L-mode and low power plasmas. The most useful shots, in which plunges were performed without observing voltage break-in, are listed in table 2.2 together with the corresponding probe assembly number.

Shot #	Gas	B_{T} [T]	$\overline{n}_{\mathrm{e}}[10^{19}\mathrm{m}^{-3}]$	I_{p} [MA]	Power [MW]	Source	Assembly
35466	D	-2.56	3.75	1.0	0.410	ECRH	#1
36736	He	-2.56	3.13	1.0	0.444	ECRH	#3
36744	He	-2.56	3.10	1.0	0.444	NBI	#3

Table 2.2: L-mode, medium density shots in a lower single null configuration used in this work. The table gives an overview of the fuelling gas used, the magnetic field strength B_{T}, the averaged-density $\overline{n}_{\mathrm{e}}$, the plasma current I_{p}, the power, the type of auxiliary heating used and lastly the assembly number of the probes.

Chapter 3

Data Analysis Techniques

An introduction to the methods used for the data analysis is given in this chapter. In section 3.1, elements of Bayesian statistics are introduced which have been used in most of the curve fitting-routines. Descriptive methods (such as moving average, autocorrelation function, spectral analysis and more) used to analyse time series are given in section 3.2. Furthermore, a brief summary of a stochastic model used to describe the measured data is presented in section 3.3. In section 3.4 examples of the methodological approaches on measured signals at ASDEX Upgrade are given.

In general, there are two statistical approaches to deal with data analysis, the frequentist (classical) and the Bayesian way. This division in statistics fundamentally exists due to the different definition of probability. The frequentist approach defines probability as the frequency of repeated events while the Bayesian approach relates probability to our own certainty or uncertainty of events. For simple problems both methods are indistinguishable, i.e, they give the same estimate of a true value. However, for more complicated problems, with many unknown parameters, Bayesian statistics tends to be more convenient as nuisance parameters (parameters that is not of immediate interest but still necessary for the data analysis) can be removed easily by marginalization. Marginalization is the procedure of integrating out the uninteresting parameters. Also, comparison and evaluation of models are easier with the Bayesian method as it assumes that the data is fixed and the model can vary around the data. The frequentist approach is usually assuming a fixed model and the data vary about it. For the data analysis conducted in this thesis, the Bayesian method is chosen as the incorporation of prior knowledge allows for a more general approach (which is better for automated routines) and the interpretation of uncertainties are more intuitive compared to the frequentist method.

3.1 Bayesian statistics

To determine the different unknown parameters of a model, Bayesian statistics is used as these can be described probabilistically [57]. Bayesian probability involves handling of

conditional probabilities. The probabilities can be manipulated by the sum and product rules as they give the desired logic to handle a situation with lack of information

$$\text{Sum rule :} \qquad \mathrm{p}(H|D) + \mathrm{p}(\overline{H}|D) = 1, \tag{3.1}$$

$$\text{Product rule :} \qquad \mathrm{p}(H, D|I) = \mathrm{p}(H|I)\mathrm{p}(D|H, I), \tag{3.2}$$

$$= \mathrm{p}(D|I)\mathrm{p}(H|D, I), \tag{3.3}$$

where H is the proposition asserting that a hypothesis of interest is true, I is the proposition representing the prior information, D is the proposition representing the data. The symbol $\mathrm{p}(H|D)$ denotes the probability that a hypothesis is true given the data and a comma separation means that both instances are true. For example, $\mathrm{p}(H|D, I)$ gives the probability that the hypothesis is true given that both the data and the prior knowledge is true. A complementary proposition is given as such: $\overline{H}$. Bayes' theorem comes directly from equation (3.2) and (3.3) and is [57]:

$$\mathrm{p}(H|D, I) = \frac{\mathrm{p}(H|I)\mathrm{p}(D|H, I)}{\mathrm{p}(D|I)}, \tag{3.4}$$

where the *likelihood* function $\mathrm{p}(D|H, I)$ estimates the probability of the observed data given the hypothesis H, $\mathrm{p}(H|I)$ is the *prior* and it incorporates the knowledge about the parameters before analysing the data. Lastly, the *posterior probability* is $\mathrm{p}(H|D, I)$ and gives the probability of the hypothesis after the data has been taken into account. $\mathrm{p}(D|I)$ $= \sum_{i=1} \mathrm{p}(H_i|I)\mathrm{p}(D|H_i, I)$ and can be seen as an ignore-able normalizing constant as it does not alter the shape of the posterior probability distribution.The subscript i represent a set of possibilities. The shape of the posterior probability distribution can simply be written as:

$$\mathrm{p}(H_i|D, I) \propto \mathrm{p}(H_i|I)p(D|H_i, I). \tag{3.5}$$

3.1.1 Likelihood and priors

Under the assumption of normal distribution and the Central Limit Theorem (CLT), the likelihood is

$$\mathrm{p}(d|D(H), \sigma) = \frac{1}{\sigma\sqrt{2\pi}} \exp\left(-\frac{(d - D(H))^2}{2\sigma^2}\right), \tag{3.6}$$

where d is the data measured with an uncertainty σ and $D(H)$ is the predicted data given by hypothesis H. The CLT states that the sampling distribution of random variables approximates to a normal distribution independent of the original distribution of the variables themselves.

As mentioned earlier, one of the advantages of Bayesian statistics is the possibility to implement prior knowledge, as state by the name itself *prior* and these are needed to evaluate the posterior probability. There are different types of priors [57], however, in this work Bayesian statistics is used to estimate the plasma parameters p_i. Since these are unknown, non-informative priors such as uniform and Jeffreys' are used and these are

given as follows

$$\text{Uniform prior} : \mathrm{p}(p_i|I) = \frac{1}{p_{i,\max} - p_{i,\min}}, \tag{3.7}$$

$$\text{Jeffreys}' \text{ prior} : \mathrm{p}(p_i|I) = \frac{1}{p_i \ \ln(p_{i,\max}/p_{i,\min})}. \tag{3.8}$$

Here $p_{i,\max}$ and $p_{i,\min}$ refers to the assumed interval in which the values of the parameter p_i should lie. Jeffreys' prior is the logarithmic equivalent of the uniform prior and it has the advantage of being invariant to monotonic transformations. A uniform prior has the disadvantage that if the domain of parameter p_i is chosen to be too large, then the value of the parameters p_i can be overestimated. Examples can be read in [58]. The posterior probability, that evaluates p_i, is proportional to the product of the likelihood and the priors.

3.1.2 Numerical application of Bayesian statistics

As shown above, for the estimation of the unknown parameters both the likelihood and the priors need to be defined. From equation (3.6), it is seen that the likelihood depends on three parameters, namely, the measurement, the estimated uncertainty of the measurement and the distribution of the uncertainty. As a consequence of the CLT, the uncertainty distribution is taken to be normally distributed. The likelihood is determined by minimizing the negative logarithm of the likelihood (eq. (3.6)). For numerical implementation, using a negative logarithm is better than the usual probability form as the logarithmic probability provides a wider computing range, i.e. -∞ to zero, while the usual probability varies in the interval [0,1]. The negative logarithm of the normal distribution is:

$$-\ln\left(\mathrm{p}(d|D,\sigma,I)\right) = \frac{(d - D(H))^2}{2\sigma^2} + C, \tag{3.9}$$

where C is a constant. The negative logarithm of priors (eq. (3.7) and (3.8)) are implemented as

$$-\ln\ \mathrm{p}(p_i|I) = \ln\left(p_{i,max} - p_{i,min}\right), \tag{3.10}$$

$$-\ln\ \mathrm{p}(p_i|I) = \ln\left(p_i \cdot \ln(p_{i,max}/p_{i,min})\right). \tag{3.11}$$

Using the negative logarithm of both the likelihood and priors, the negative logarithmic posterior probability is then

$$-\ln(\mathrm{p}(H|D,I)) = -\sum_i \ln(\mathrm{p}(H|I)) - \sum_j \ln(p(D|H,I)). \tag{3.12}$$

Quality assessment of the fits

The methods used to assess the quality of a given model D in describing the measured data d are:

1. The residual
2. The coefficient of determination R^2

The residual gives the differences between the measured data d_i and the values estimated by the model D_i:

$$\text{residual}_i = d_i - D_i, \tag{3.13}$$

where the index i represent i^{th} data point. The value R^2 provides a measure for the goodness of the fit for the model. It lies between zero and one and is defined as[1]:

$$R^2 = 1 - \frac{\sum_{i=1}^{n} (D_i - d_i)^2}{\sum_{i=1}^{n} (d_i - \langle d \rangle)^2}, \tag{3.14}$$

where $\langle d \rangle$ is the mean of the measured data. The larger the value of R^2 is, i.e the closer it is to one, the greater a proportion of the measured data is explained by the model. The two methods are used through out the thesis to check the quality of how well models are describing the measurement.

3.2 Moments and statistical analysis techniques

The common methods used to quantify the various aspects of the fluctuations in a time series are the probability density function, the power spectral density and the autocorrelation function are discussed in section 3.2.1, 3.2.4 and 3.3.1, respectively. The latter are briefly described in the following section. Time series analysis are performed on statistically stationary data and a method to remove trends from a time series is given in section 3.2.2

3.2.1 Probability density function

The probability density function (PDF) gives the statistical measure of the most likely outcome of a continuous random variable. An approximation of a PDF can be obtained using the histogram method [59]. The value of the probability 'mass' at a point x with width Δx is obtained from the density function $f_X(x)$ as

$$f_X(x) \approx \frac{P(X \leq x + \Delta x) - P(X \leq x)}{\Delta x}, \tag{3.15}$$

where P$(\cdot)$ is the cumulative distribution function. To create the histogram, the range of data points N is divided into equal sized sub-intervals of length Δx or equident into the desired number of bins K, given by

$$\text{Number of bins } K = \frac{\text{range of data } N}{\text{bin width } \Delta x}. \tag{3.16}$$

The number of data points $\{n_i, i = 1, \ldots, K\}$ falling into each bin is then counted and divided by the total number of observations N and multiplied by the bin width Δx. Thus,

[1]This value can actually be negative and it means that the fit is doing worse than the mean value.

the area under the histogram equals one by construction. This histogram method has been implemented from the existing module in Python Numpy library [2].

The *running* moments (i.e, mean, standard deviation, skewness and flatness) of a time series can be calculated by dividing it into overlapping windows, each having its separate moments. The first raw- and the second central-moment of a stochastic process are the mean and the variance, respectively. The definitions of the following moments have been adapted from [59]. For any random variable X with probability density f_X, the **mean** $\langle X \rangle$ is defined as follows:

$$\langle X \rangle \equiv \int_{-\infty}^{\infty} x f_X(x)\, \mathrm{d}x. \tag{3.17}$$

The **variance** σ_X^2 shows the variability of the random variable X about its mean value, $\langle X \rangle$ and is defined as:

$$\sigma_X^2 \equiv \int_{-\infty}^{\infty} (x - \langle X \rangle)^2 f_X(x)\, \mathrm{d}x. \tag{3.18}$$

A small σ_X^2 indicates that the variables are close to the mean value while a large σ_X^2 indicates a large variability from the mean value. The **standard deviation** σ_X, is the square root of the variance σ_X^2.

The mean and the variance constitutes the first and second order moments. In general, the kth-order central moments are defined as

$$\mu_k = \int_{-\infty}^{\infty} (x - \langle X \rangle)^k f_X(x)\, \mathrm{d}x. \tag{3.19}$$

The **skewness** S measures the lack of symmetry of the tails of a distribution. The skewness of a random variable is defined as:

$$S \equiv \frac{\mu_3}{(\sigma_X^2)^{3/2}}, \tag{3.20}$$

where μ_3 is the third central moment and σ_X is the variance (see eq. (3.19)). Vanishing skewness means that the distribution is symmetric, e.g a Gaussian distribution. A distribution function can be positively or negatively skewed. A positive skewness means that the right tail is longer compared to the left one, while a negative skewness means that the left tail is longer.

The **flatness** or **kurtosis** measures the 'peakness' of a distribution and the 'heaviness' of its tail relative to a normal distribution. Together with the fourth central moment μ_4, the flatness F is defined:

$$F \equiv \frac{\mu_4}{\sigma_X^4}. \tag{3.21}$$

A distribution with low flatness will have a flat top and a high flatness will display a peak near the mean. A Gaussian distribution has a flatness of 3. The moments of a discrete time series can be obtained numerically using the Python Scipy library [3].

[2] https://docs.scipy.org/doc/numpy/reference/generated/numpy.histogram.html
[3] https://docs.scipy.org/doc/scipy/reference/generated/scipy.stats.moment.html

In a turbulent environment where the fluctuations satisfy a Gamma distribution, a parabolic relation between S and F has been observed:

$$F = \frac{3}{2}S^2 + 3. \tag{3.22}$$

In an environment with only Gaussian fluctuations the above relationship reduces to a fixed point where $S = 0$ and $F = 3$. This relationship between the third and fourth moment has also been observed in different turbulent systems other than plasma physics, e.g. in [60–62].

3.2.2 Normalization of time series

Time series analysis are very often described for statistically stationary signals, i.e., a signal without trends. A method to remove trends from a time series Φ is by subtracting the individual mean $\langle\Phi\rangle$, of each window and normalizing it by its standard deviation σ_Φ:

$$\tilde{\Phi} = \frac{\Phi - \langle\Phi\rangle}{\sigma_\Phi}. \tag{3.23}$$

This is a standard method of normalizing signals before performing any analysis. This effectively removes the mean and puts the variance to unity. In the following, this method will be implemented unless specified otherwise.

3.2.3 Autocorrelation function

The autocorrelation function (ACF) is the correlation of a signal with itself at a lag time τ. It can be estimated as [63]:

$$ACF = \frac{1}{(N-\tau)\sigma^2} \sum_{t=1}^{N-\tau} \left(x_t - \langle x\rangle\right)\left(x_{t+\tau} - \langle x\rangle\right). \tag{3.24}$$

The ACF can take values in the range of [-1,1]. If the value of the ACF at a time $t + \tau$ is -1, then the signal is perfectly anticorrelated, while an ACF of 1 indicates that there is perfect correlation, as there is a positive linear relation between the signal at time $t + \tau$ and time t. A value of 0 indicates that there is no correlation at all and in this case, the ACF will indicate random Gaussian process such as white noise.

The ACF is also a measure of the stationarity of a signal. The short correlation time τ, compared to the length of the signal itself, indicates that the signal is stationary. The correlation of a signal has been implemented in the Numpy Module of Python [4].

[4] https://docs.scipy.org/doc/numpy/reference/generated/numpy.correlate.html

3.2.4 Power spectral density

To extract the dominant frequency components of a signal, it is useful to represent the signal in the frequency-domain. The fundamental application that transform the signal from the time domain to the frequency domain is the Fourier transform [64]:

$$F(\omega) = \int_{-\infty}^{\infty} f(t) e^{-i\omega t} dt, \tag{3.25}$$

where $F(\omega)$ is the Fourier transform of the continuous signal $f(t)$ and ω is the angular frequency. The power spectral density $PSD(\omega)$, is then [64]

$$PSD(\omega) = |F(\omega)|^2. \tag{3.26}$$

The PSD quantifies the strength of the fluctuations as a function of the frequency. The Fourier transform for discrete signals is computed using the fast Fourier transform (FFT) and a detailed implementation in Python can be found in the Numpy FFT module [5]. The PSD can also be determined using the Welch method [65] and an implementation can be found in the Python Library [6]. The Welch method estimates the power spectra by dividing the signal into overlapping segments. This division of the signal leads to noise reduction in the estimated power spectra, thus making the Welch method an improved approach compared to the standard periodogram.

Signals can be decomposed into two parts: background noise and physical measurement. For signals consisting of pure noise, the power spectrum is uniform and this is known as white noise. Signals of coherent measurements show a peak in the power spectrum, which corresponds to an oscillation in it. Such power spectrum usually follows a power-law behaviour of $PSD(f) \propto f^{-\alpha}$, where α is the slope of the PSD. For pure white noise, α is zero. The power-law behaviour has been observed in many fields and has lead to speculations that such spectra can be signatures of a universal mechanism. In this work, the slope of the PSDs will be fitted to investigate the power-law behaviour in the different regions of ASDEX Upgrade divertor.

The ACF is the inverse Fourier transform of the PSD, thus making them a Fourier pair. The Wiener-Khinchin theorem plays a key role in building this relation, which is given as follows [66]:

$$ACF(\tau) = \int_{-\infty}^{\infty} e^{i\omega\tau} S(\omega) d\omega. \tag{3.27}$$

For a detailed derivation of the above formula, the reader is referred to [66].

To interpret the I_{sat}^{+} time series measured in ASDEX Upgrade the filtered Poisson process is used [13]. This model provides a method to unify the observations (such as PDFs, ACF, PSD and wave-form shape) to characterize filamentary structures. Experimental observations and simulations of the SOL at the outboard mid-plane of several tokamaks

[5] https://docs.scipy.org/doc/numpy/reference/generated/numpy.fft.fft.html
[6] https://docs.scipy.org/doc/scipy/reference/generated/scipy.signal.welch.html#r34b375daf612-1

reveals that the PDFs of the ion-saturation current measurements and signals from gas-puff-imaging are skewed and flattened. Also an exponentially decaying ACF has been observed and the PSD spectra of these signals are Lorentzian, i.e the spectra falls as ω^{-2}. These are reported in the following publications [67–70]. From conditional averaging methods, the bursty nature of filamentary structures is shown to exhibit a strong asymmetric waveform with a fast exponential-growth and slow exponential decay [67–69, 71–73] This is a stochastic model that has been successfully tested on probe and gas puff imaging (GPI) measurements at the outboard mid-plane in other different tokamaks [72–75]. It has been shown that the model can describe the intermittent plasma fluctuation at the outboard mid-plane SOL satisfactorily. In the following section a brief summary of the filtered Poisson process and the conditional averaging method is given, for detailed derivation of the equations, the reader is deferred to [13, 72–74, 76–78].

3.3 The filtered Poisson process

For the filtered Poisson process (FPP), a given time series $\Phi(t)$ is modelled as the superposition of uncorrelated pulses K which are assumed to arrive according to a Poisson process.

$$\Phi(t) = \sum_{k=1}^{K} A_k \varphi\left(\frac{t - t_k}{\tau_{\mathrm{d}}}, \lambda\right), \tag{3.28}$$

where A_k is the pulse amplitude, time $t \in [0, T]$, $\lambda \in]0, 1[$ is the pulse asymmetry parameter, τ_d gives the pulse duration time and t_k are the arrival times of the pulse. The pulse amplitude are exponentially distributed and the pulses are assumed to be independent. The arrival time of the pulses are assumed to be distributed uniformly in the time interval t, as the Poisson distributed pulses arrive with a intensity of T/τ_{w} and τ_{w} is the mean value of the exponentially distributed waiting time between the arriving pulses [77].

Based on experimental observations [67], it has been postulated that the pulse shape is a two-sided-exponential function spanned by two parameters (λ,τ_d) and thus asymmetric:

$$\varphi(t, \lambda) = \begin{cases} \exp\left(-\frac{t}{(1-\lambda)\tau_{\mathrm{d}}}\right), & t \geq 0, \\ \exp\left(\frac{t}{\lambda\tau_{\mathrm{d}}}\right), & t < 0. \end{cases} \tag{3.29}$$

A pulse that rises faster than it decays has an asymmetry parameter of less than 0.5, i.e $\lambda < 1/2$. For $\lambda < 1/2$, the pulse is symmetric. One-sided exponential pulses are described by $\lambda = 0$ or $\lambda = 1$. Under the above assumptions and normalizing the time series according to equation (3.23), the process described by equation (3.28) is Gamma distributed

$$P_{\widetilde{\Phi}}(\widetilde{\Phi}) = \frac{\gamma^{\gamma/2}}{\Gamma(\gamma)} \left(\widetilde{\Phi} + \gamma^{1/2}\right)^{\gamma-1} \exp\left(-\gamma^{1/2}\widetilde{\Phi} - \gamma\right), \ \widetilde{\Phi} > -\gamma^{1/2}, \tag{3.30}$$

where γ is the intermittency parameter and gives the shape parameter of the probability density function (PDF), $P_{\widetilde{\Phi}}(\widetilde{\Phi})$. For the FPP model, the γ parameter is defined as the ratio

of the duration time to the mean waiting time, i.e, $\gamma = \tau_{\rm d}/\tau_{\rm w}$. The γ parameter resolve the degree of pulse overlap of the stochastic process, i.e., the degree of intermittency of the process. For exponentially distributed amplitudes, the intermittency parameter can also be calculated from the third and fourth moments of the original signal [13, 78]:

$$S_\Phi = \frac{2}{\gamma^{1/2}}, \tag{3.31}$$

$$F_\Phi = 3 + \frac{6}{\gamma}. \tag{3.32}$$

The power spectral density $PSD_{\widetilde{\Phi}}(\omega)$, of a normalized signal is given by:

$$PSD_{\widetilde{\Phi}}(\omega) = \frac{2\tau_{\rm d}}{\left[1 + (1-\lambda)^2\tau_{\rm d}^2\omega^2\right]\left[1 + \lambda^2\tau_{\rm d}^2\omega^2\right]}. \tag{3.33}$$

The PSD spectrum is flat for low frequencies. The PSD spectrum with an asymmetry parameter λ of zero or one falls off as ω^{-2} and at high frequencies it falls off as ω^{-4}. The autocorrelation function $ACF_{\widetilde{\Phi}}(t)$, of a normalized time series is:

$$ACF_{\widetilde{\Phi}}(t) = \frac{1-\lambda}{1-2\lambda}\exp\left(-\frac{|t|}{(1-\lambda)\tau_{\rm d}}\right) - \frac{\lambda}{1-2\lambda}\exp\left(-\frac{|t|}{\lambda\tau_{\rm d}}\right), \tag{3.34}$$

$$ACF_{\widetilde{\Phi}}(r;1/2) = \left(1 + \frac{2|r|}{\tau_{\rm d}}\right)\exp\left(-\frac{2|r|}{\tau_{\rm d}}\right), \tag{3.35}$$

where r is the time-lag. At $\lambda = 1/2$ there is a singularity and the ACF is given for a Gaussian signal in equation (3.35) [79]. It should be noted that the PSD and the ACF are independent of the intermittency parameter γ and therefore depends only on the asymmetry and the duration time of the pulse. This independence of γ arises from the assumption that the pulses are uncorrelated.

3.3.1 Conditional averaging

Conditional averaging (CA) is nowadays the standard method used to detect the average structure of large-amplitude bursts in a broad band and incoherent background of turbulent flows. Johnsen *et al.* [80] and Huld *et al.* [81, 82] were among the first to implement this method in plasma, where they showed the presence of long-lived vortex-like structures in a broadband turbulent background by using the CA technique. For a given time series $\Phi(t)$, a condition C is chosen. Whenever a large amplitude event fulfilling the given condition is detected a sub-window around the event is picked out from the original signal. To get the conditionally averaged wave-form, the sub-windows of all the events recorded are averaged over all the events. To ensure statistical independence of the events, overlapping of the conditional sub-windows are avoided [72]. Conditional averaging is also a good method to check whether the signal is a random Gaussian signal [83, 84]. Edwards *et al.* [83] showed that the CA can be rewritten in terms of ACF. The amplitude of the wave-form obtained by applying a condition in the CA method can be described by the product of the ACF

and the condition, if the signal is Gaussian. There is a vast literature available, where the derivations and methods are described in more details. In this work, we focus on giving a brief overview of the method. For further details, the interested reader is referred to [40, 72, 76, 84, 85]. The method used in this thesis is based on method described in [72, 76].

3.4 Example on measured data

In this section, an example of application of the discussed previously analysis methods is shown. The implementation of the Bayesian statistics to determined the plasma parameters from the I-V characteristic curves is presented in section 3.4.1 and the evaluated parameters are validated using the measurements of the Langmuir probes embedded in ASDEX Upgrade divertor. Section 3.4.2 gives an overview of the measurements collected by the biased Langmuir probe and discusses the error of determining the private flux region.

3.4.1 Sweeping Langmuir probe

An example of the time series measured by the sweeping Langmuir probe (3) is shown in figure 3.1. Figure 3.1 (a) shows the whole time series of shot #36744. The blue line (top) represents the XPM trajectory. The values of the major radius R_m, is decreasing as the XPM moves from the LFS towards the HFS. The black line (middle) shows the sweeping voltage. The current measured is shown in green (bottom). Due to arcing a voltage break-in is observed, annotated by the red arrows in middle figure. As discussed in section 1.5, instead of the electron-saturation current, the ion-saturation current is used to determine the electron density. The ion-saturation occurs at negative voltage and therefore for a good I-V curve, it is crucial that the voltage break-in does not occur in the negative voltage range, otherwise the data is neglected.

Figure 3.1 (b) shows the time series of the first plunge of shot #36744. An I-V curve can be created using each slope of the sweeping voltage and the corresponding current.

To determine the plasma parameters from the data collected by the sweeping Langmuir probe, a Bayesian approach is used to fit the I-V curves. The model D, used to represent the measured data is given by equation (1.7). The plasma parameters p_i, to be deduced from the I-V curves are: **1.** Effective ion-saturation current, $I_{\mathrm{sat,eff}}$, which is AI^+_{sat} from equation (1.7), **2.** Floating potential, V_{float} and **3.** Electron Temperature, T_{e}. To optimize the curve fitting the following priors are chosen:

- $T_{\mathrm{e}} \in [0, 100]$ eV. The electron temperature is constrained from above by results obtained from past experiments.
- $V_{\mathrm{float}} < +100$ V. This prior has chosen based on random visual I-V curves check.
- $I^+_{\mathrm{eff}} > 0$ A. For convention, I^+_{eff} is chosen to be positive.

Figure 3.2 shows an example of a fitted I-V curve at time $t = 1.662$ s and at major radius $R_m = 1.506$ m. The red line represent the model used to describe the I-V curve and the fitted parameters are also listed. Superfluous data points (in black) are observed on the

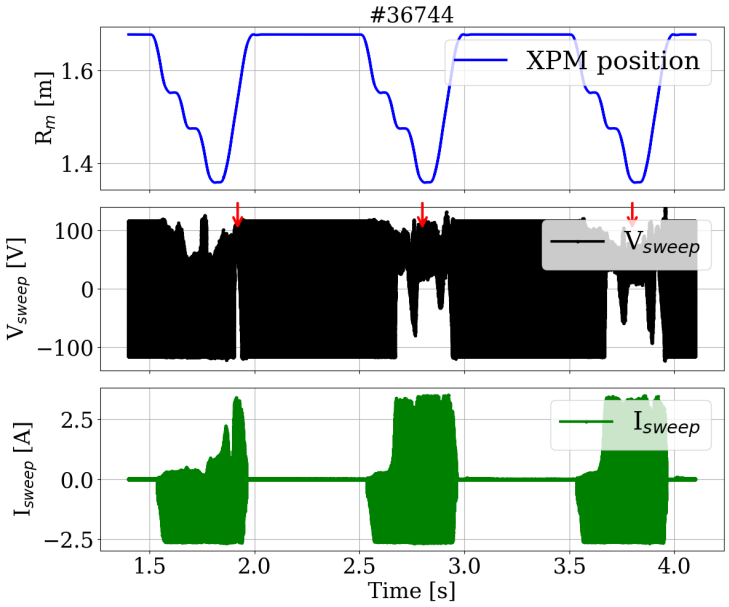

(a)

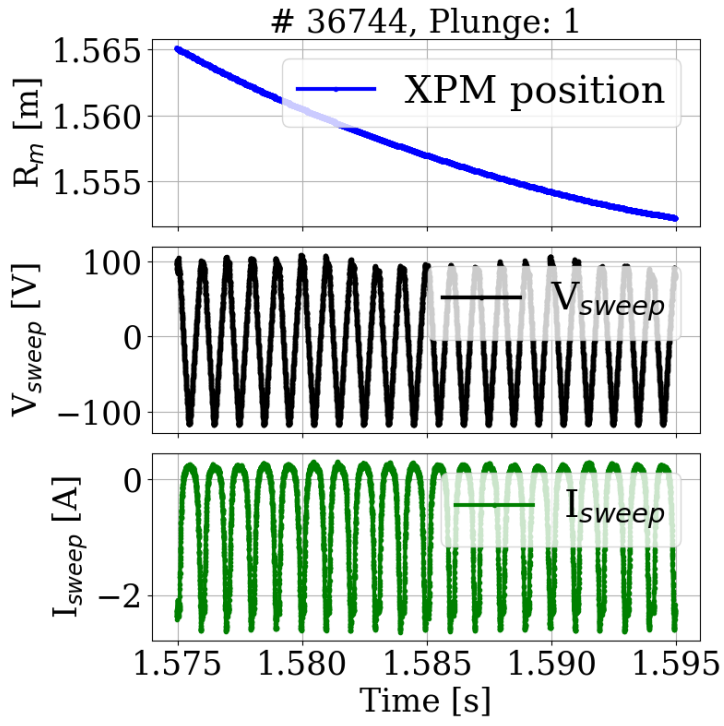

(b)

Figure 3.1: (a) the time series of the sweeping probe for shot #36744 and (b) Zoomed-in of postion, voltage and current measurement of the first plunge of shot #36744.

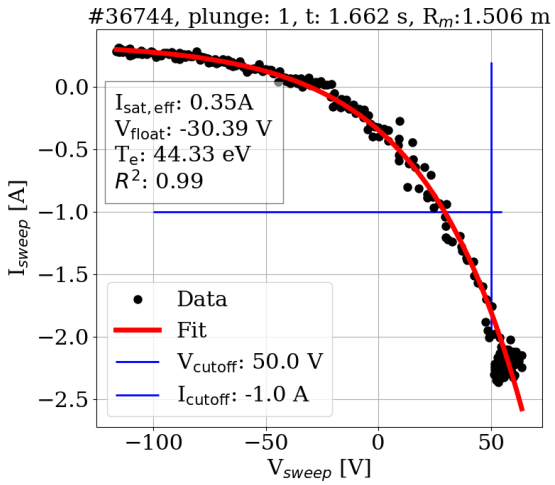

Figure 3.2: Example of an I-V curve obtained during the first plunge in shot #36744 with the corresponding fitted plasma parameters.

electron-saturation branch of the I-V curve. It is, therefore, important for the analysis to restrict the range of data set to be used for the curve fitting. The range in the data set is shown by cut-off values for the current and voltage and is shown by the blue lines. In some cases the electron-saturation 'branch' have scattered points up to +100 V. If those

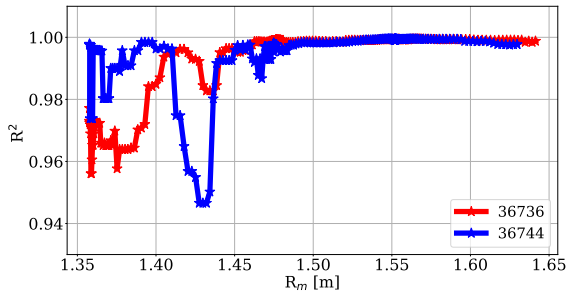

Figure 3.3: R^2 coefficient as a function of major radius R_m showing the goodness of of I-V curves fit for the first plunge of both shots #36736 and #36744.

scatter data points are blindly taken into account during the fit, the slope of the I-V curve is described poorly. This is avoided by choosing the range using cut-off values, which are chosen as a good compromise for all the I-V curves for a specific plunge. The quality of the fit is quantified by the parameter R^2, which in this example is 0.99 and indicates that the model describes most of the data. The quality of the I-V curve-fit are given by the R^2 coefficient as a function of the major radius R_m in figure 3.3, where it is observed that the R^2 coefficient varies between 0.95 - 1.0. Hence, showing that the fitting model is able to described the measured I-V characteristics satisfactorily.

Figure 3.4 shows the same I-V curve (top) as in figure 3.2 and its residual plot (bottom) to

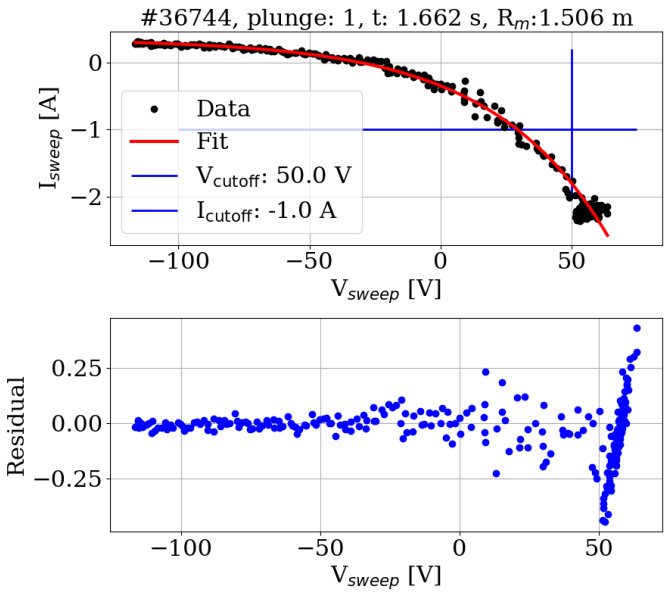

Figure 3.4: Example of an I-V curve obtained during the first plunge in shot #36744 and its residual.

show the goodness of the fit. The blue dots show the residual as a function of the measured voltage. It is observed that the residual of the data vary around zero until +10 V. This indicates that the parameters determined using the Bayesian analysis models the measured data with reasonable accuracy. The clump of the data points around -2.3 A and 55 V shows a larger residual, however the values are varying almost symmetrically between ± 0.25.

The plasma parameters obtained from the characteristics curve of the sweeping Langmuir probe have been validated using the data obtained from the embedded Langmuir probes in the divertor leg of ASDEX Upgrade and the comparisons are shown in figure 3.5. The plasma parameters are given as a function of the poloidal flux surface ρ_p and 1.0 represents the separatrix leg. The different colours of the plasma parameters of the divertor Langmuir probes represent three time ranges: before the plunge (1.1 - 1.5 s), during the plunge (1.5 - 2.0 s) and after the plunge (2.0 - 2.5 s). The XPM data is shown as black dots. It is observed that the plasma parameters determined are in good agreement with the divertor Langmuir probes and thus, showing that the assumptions and the method of analysis is plausible.

3.4.2 Biased Langmuir probe

The Langmuir probes (1 & 2) are biased at approximately -170 V and are used to measure the ion-saturation current along the XPM trajectory at a sampling frequency of 500 kHz. An example of the whole time series is shown in figure 3.6. Figure 3.6 (a) shows the measurements of the three plunges carried out during shot #36744. The top figure represents the XPM trajectory (in blue) during the plunge in the vacuum vessel. In the

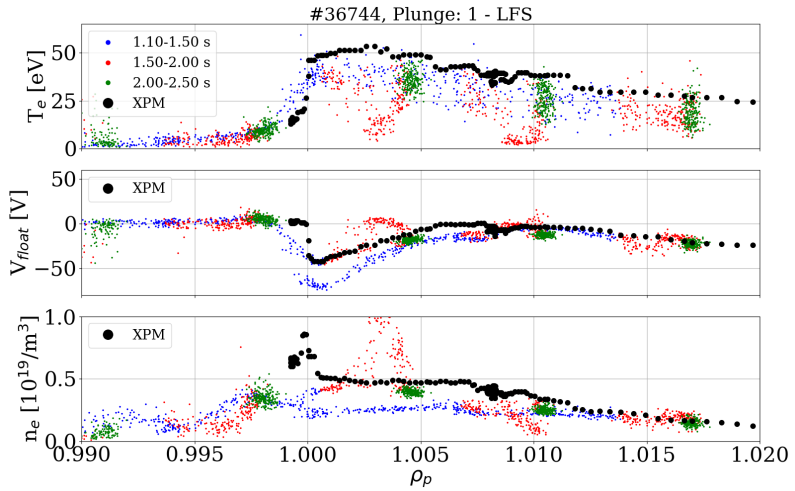

(a)

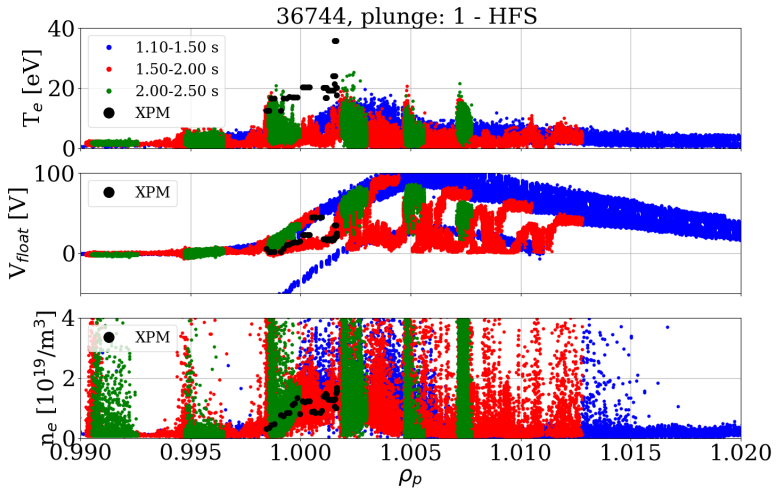

(b)

Figure 3.5: Validation of the plasma parameters of the first plunge of shot #36744 determined for the sweeping Langmuir probes with those embedded in the divertor legs (a) LFS data and (b) HFS data. Courtesy of D. Brida.

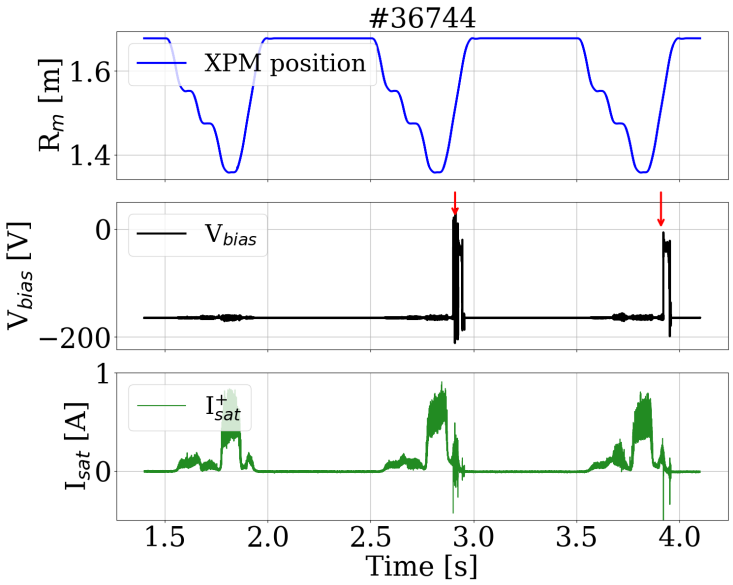

(a)

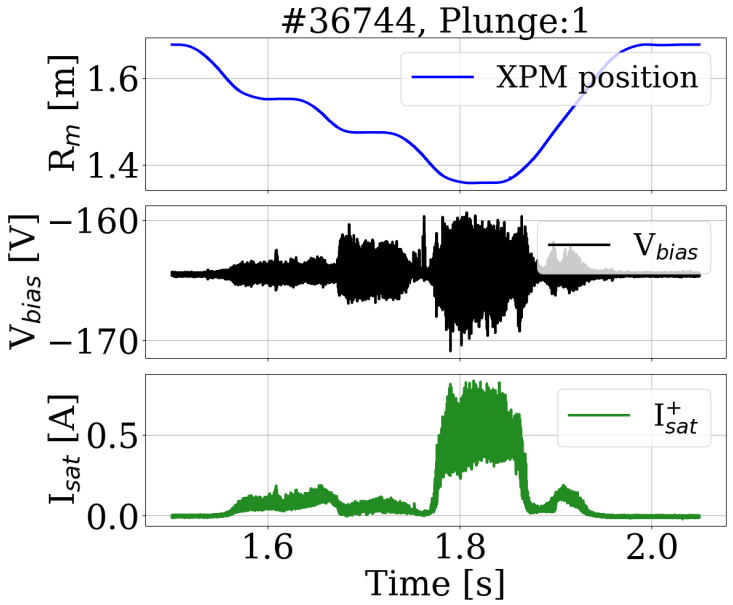

(b)

Figure 3.6: (a) The time series of the biased Langmuir probe for shot #36744 and (b) the biased voltage and ion-saturation current measurement of the first plunge of shot #36744.

middle, the time trace of the biased voltage is shown. During the experiments, we observed arcing very often and the times at which it occurred are shown by the red arrows. The bottom figure represents the determined ion-saturation current in green. In figure 3.6 (b) the time series for the first plunge is shown. During several plunges, the probe was held stationary at three planned positions for approximately 20 ms otherwise the probe moved with approximately constant speed. The data measured by the biased Langmuir probe can therefore be divided into two categories: 1. Probe-stationary phase, and 2. Moving probe phase.

Since most of the probability theory of time series are for stationary time series, often it is necessary to convert a non-stationary time series into a stationary one. A time series is defined as *stationary* if there is no systematic change in its mean and variance, i.e, trends have been removed. Therefore to be able to analyse the data collected when the probe is in motion, a quasi-stationary assumption is made. For a tip length of 2 mm, the time taken for the probe to move the length of the tip is ≈ 0.8 ms. However, such a small interval consists of merely 350 data points in our case. As a fair compromise for statistical significance and stationary assumption, the probe is therefore assumed to be quasi-stationary on time scales of 2.4 ms allowing fluctuation analysis while the probe is in motion. In the stationary probe phases, it is possible to get large variation in the current measurements which increases the mean value of the signal. To be able to compare the samples during the stationary probe phases it is important to account for such variation by normalising the data. This method removes the trends from the time series I^+_{sat} by subtracting its moving mean $\langle I^+_{\mathrm{sat}} \rangle$ and it is normalized by the moving standard deviation $\sigma_{I^+_{\mathrm{sat}}}$.

Figure 3.7 (a) shows the I^+_{sat} of the first plunge of shot #35466 as a function of the major radius R_m. The shaded region represent the private flux region (PFR) as determined from magnetic reconstruction codes IDE [86] and CLISTE (EQH). The private flux region has been determined by by using the EQH program. To investigate the reliability of the PFR position, the magnetic reconstruction of two codes are compared and the difference of the separatrix legs are determined. An example is given in figure 3.7 (b) for shot #35466 at time ≈ 1.59 s. It is observed that the low-field side (LFS) separatrix are mostly in perfect agreement using both codes as they lie on top of each other. The high-field side (HFS) separatrix leg showed a difference of ≈ 3 mm. It is determined that the LFS separatix leg can be determined with an accuracy of approximately $\pm$ 5 mm while the HFS separatrix is determined by approximately $\pm$ 10 mm. However, it is challenging to reconstruct the exact magnetic equilibrium close to the X-point and therefore, by plotting the PFR on top of the ion-saturation current measurements, it is examined how well the separatrix legs have been reconstructed. In general, we observe a decrease in the ion-saturation current when transiting from the LFS SOL into the PFR. Also, a peak is observed in the ion-saturation current when crossing the separatrices and these are used as a reference to locate the PFR. In case of a significant difference between the equilibrium code and the measurement is found, the PFR region is adjusted according to the measured ion-saturation current.

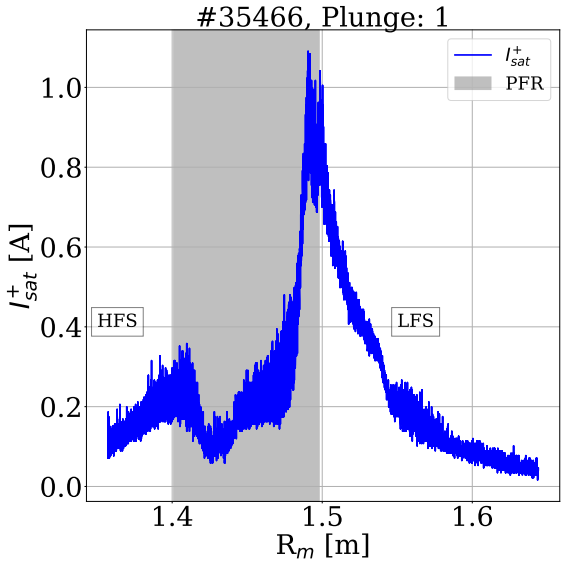

(a)

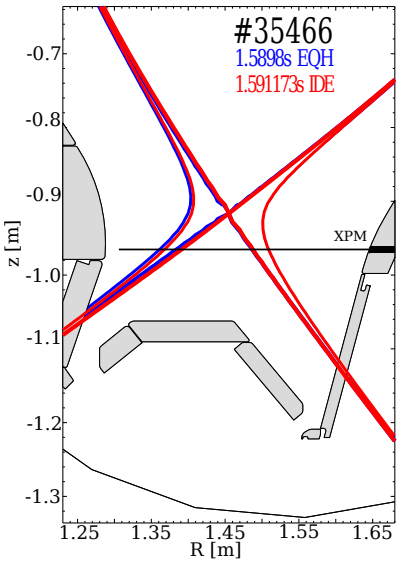

(b)

Figure 3.7: (a) Ion-saturation current as a function of major radius R_m of #35466 with the shaded area representing the private flux region and (b) the magnetic reconstructions using two codes for #35466.

Chapter 4

Synthetic Data Analysis

Before considering actual measurements in chapter 5, we consider an intermediate analysis of synthetic time series to characterise the technique of the filtered Poisson process (FPP). This will provide an understanding of the conditional averaging (CA) method, the power spectral density (PSD) and the autocorrelation function (ACF) pair, when it is later applied on actual measurements. In this chapter, we begin in section 4.1 by considering a signal consisting of Gaussian noise to illustrate the characteristics of white noise. We then move to section 4.2 to consider synthetic data generated by the FPP in such a way to mimic the ion-saturation current measurements of the Langmuir probes. Having the signal generation under full control allows us to gain insight on specific features of hand-crafted signals and the capability of the analysis tools. In section 4.3 we take the consequences, based on the learning from the synthetic data, into consideration and apply filtering on the measurements.

4.1 Gaussian distributed noise signal

In this section, a synthetic signal S, without loss of generality, is generated by a random walk of samples drawn from a Gaussian distribution with a mean of $\mu = 0$ and a standard deviation of $\sigma = 0.5$. The signal is generated with 10000 points, representing a sampling rate of 0.1 ms, to mimic a measurement with statistical significance. The analysis is carried out in a similar manner as meant for the actual measurements. Therefore, the signal S is normalized according to equation (3.23). This sets the variance to unity. A normalized signal $\tilde{S}$, is shown in figure 4.1.

To assess the behaviour of the CA, the method is applied for three thresholds: 1.5, 2.5 and 3.0 on the normalized signal.

Figure 4.2 (a) shows the resulting wave-forms obtained for the three different thresholds. Starting in the ascending order, the conditional events recorded for each threshold are 621, 59 and 11, respectively. Having more conditional events simply means that the wave-forms are smoother as there are more statistics available. It is observed that the peak at

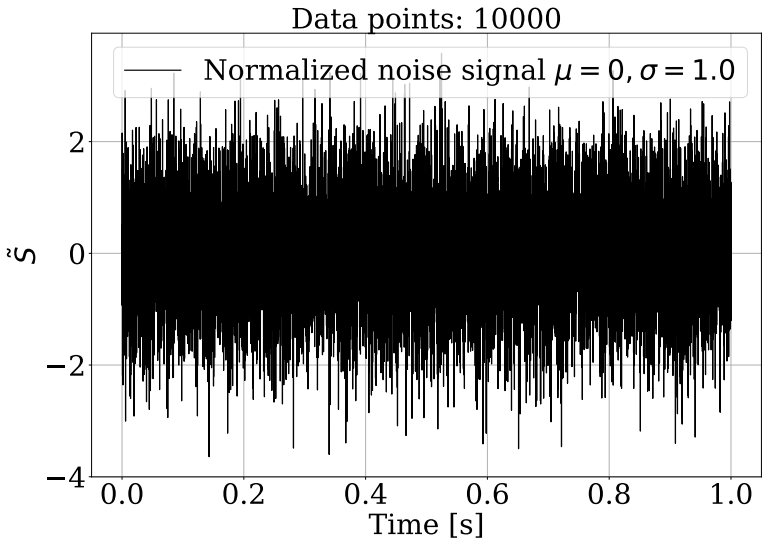

Figure 4.1: Noise signal normalized to its standard deviation with zero mean and a variance one.

$\tau_{CA} = 0$ of the wave-form increases slightly with increasing threshold. It should be noted that for a signal at very high sampling rate, the peak of the CA wave-form converges to a delta-peak. Note that when dealing with real measurements a threshold of 2.5 is chosen to make the comparison consistent with literature. Also, the wave-forms have been compared for different thresholds and no significant change in the shape was observed, which is in agreement with [72].

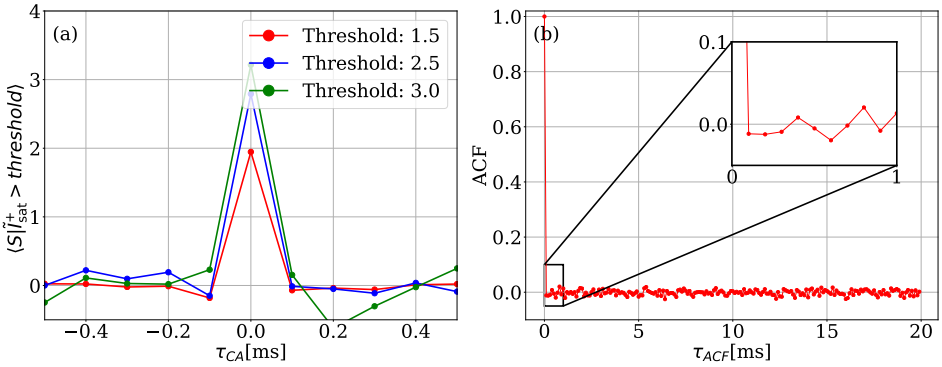

Figure 4.2: (a) Conditional averaged wave-form of a noise signal and (b) its autocorrelation function.

The corresponding autocorrelation function (ACF) is presented in figure 4.2 (b). The ACF decreases instantaneously to zero and fluctuates around zero for increasing time lag τ_{ACF},

showing that there is no correlation in the signal as expected. Figure 4.3 shows the power spectral density (PSD) spectrum (as given by the Welch method). A relatively flat PSD spectrum is obtained as expected for a noise signal, which otherwise would fall with a power law (sec. 3.2.4).

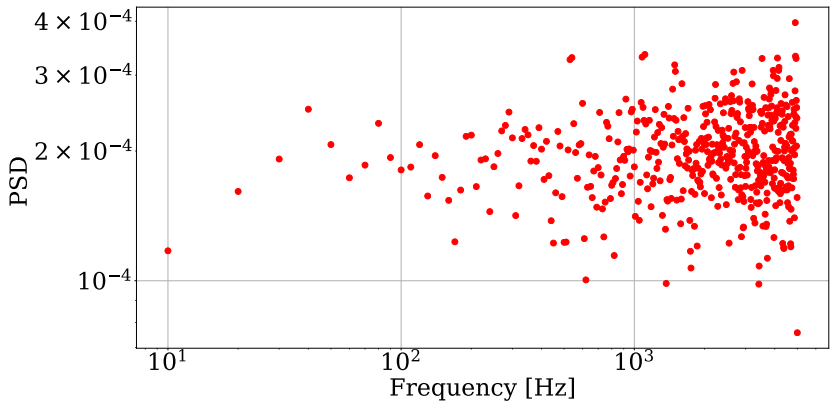

Figure 4.3: Power spectrum density of a noise signal.

4.2 Synthetic Langmuir probe signal

In the following section, the data analysis method is tried on synthetic signals in order to highlight how the pulse characteristics (i.e., its duration time τ_d and the asymmetry parameter λ) can be estimated from the CA wave-form. The synthetic signals are generated in such a way to imitate the measured data obtained from the probe measuring on the LFS in a stationary configuration. Two types of synthetic data signals are generated using the FPP model for two functions, seeded by one-sided exponential and a two-sided exponential, respectively. In order to generate plausible synthetic data, the analysis is ran side-by-side with an actual time series obtained from the LFS. This analysis is also used to estimate the relevant range of parameters for the synthetic data. From the LFS measurement, an intermittency parameter $\gamma = 20.2$, a duration time of $\tau_d = 12.0\,\mu$s and an asymmetry parameter $\lambda = 0.6$ are obtained. The intermittency parameter γ is estimated from the skewness of the signal (see eq. (3.31)).

The synthetic data is generated by the convolution of the seed function (either a one-sided- or two-sided- exponential) and a number of K delta pulses that are Poisson distributed. The Poisson distributed parameter K gives the number of arriving events (see eq. (3.28)). The length of the synthetic data is indirectly determined by the parameter K and γ. No additional noise has been added to the synthetic signal. For the presented (fig. 4.4 (b) and (c)) synthetic data K is chosen to be 105000. In addition to these parameters, the sampling rate dt of the diagnostics is used, i.e., dt = 2 μs.

Figure 4.4 shows the normalized signals, where (a) is the measured signal on the LFS with a length of approximately 30 ms while,(b) and (c) shows the two synthetic signals of

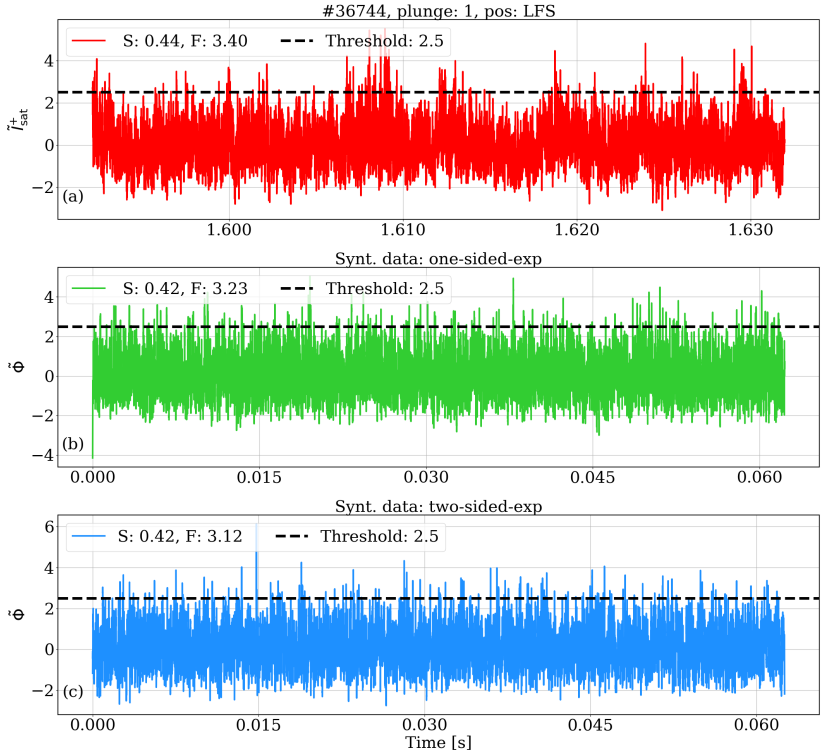

Figure 4.4: (a) Measured signal of the first plunge on the LFS of shot #36744. (b) Long synthetic data generated for a one-sided exponential function and (c) Long synthetic data for a two-sided exponential. The signal has been generated by the parameters: $\gamma = 20.2, \tau_d = 12\ \mu s, \lambda = 0.6$.

approximately 60 ms. For the CA analysis a threshold of 2.5 is used and this is marked by the black dashed line in fig. 4.4. Note that the generated signals have a time period of approximately double of the measured one. This gives the synthetic data a little more statistics. Synthetic signals of shorter period are considered in the appendix A.1.

The CA method is now applied on the normalized signals. The corresponding wave-forms together with the fitted parameters are shown in figure 4.5. The purple dashed line represents the parameters used to generate the synthetic signals and the black dashed line shows a double-exponential curve fit (see eq. (3.29)). Note that even though the data is generated by a one-sided exponential function, it is still fitted with a double-exponential. This is to represent a real-case scenario, where the function describing the measured signal is unknown. The number of conditional events obtained for the normalized signals are:

- LFS measured signal: 190,
- One-sided exponential synthetic signal: 248 and,
- Two-sided exponential synthetic signal: 176.

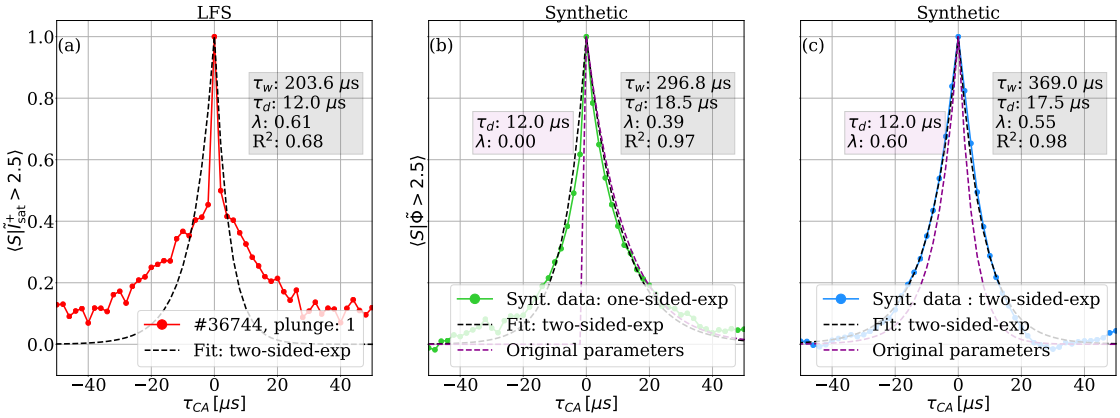

Figure 4.5: Conditionally averaged wave-form of (a) the measured signal, (b) the one-sided exponential function and (c) the two-sided exponential. The threshold is 2.5 and the wave-forms are normalized to their peak value.

In figure 4.5 (a), it is seen that the double-exponential fit does not describe the measurement properly with a bare R^2 of 0.68. From the CA wave-form it is evident that the data has a peak similar to the wave-form observed for the noise signal in figure 4.2 (a). In the next section (sec. 4.3), filtered measurements are considered. Figure 4.5 (b) shows that the double-sided-exponential fit does not seem to capture the underlying one-sided exponential function used for generation. However, that is interesting to note that if the double-exponential is mapped to a one-sided-exponential, the duration time obtained is much closer to the expected value ($(1-0.39)\cdot 18.5 = 11.3$). Nevertheless, the double-exponential fits the signal exceedingly well with $R^2 \approx 0.97$. It is observed that the wave-form obtained for the double-sided–exponential case is not described perfectly by the original parameters in figure 4.5 (c) and from the fitting function a larger τ_d value is obtained. This is likely due to pulse overlapping in the generated signal due to a non-skewed Poisson distribution (i.e, $\gamma \gg 1$). This will be discussed in more detail later.

The FPP model gives the opportunity to describe the PSD and the ACF with the parameters obtained from the CA wave-forms (see eq. (3.33) and eq. (3.34), respectively). This is shown in the PSD and the ACF of the three time series shown in figure 4.6 and 4.7, respectively. The PSD and the ACF are obtained from equation (3.33) and equation (3.34), respectively. Since, using the parameters obtained from the CA wave-form cannot reproduce the data (see black curve in fig. 4.6), an independent fitting to the PSD using equation (3.33) is performed. Note that the two data points, marked as stars in figure 4.6 (a), are due to electrical interference and have therefore not been considered while fitting the PSD spectrum. Only the slope of the determined PSD is used for this fit (data in black in fig. 4.6 (a) as the slope after approximately 80 kHz starts bending slightly upwards). From figure 4.6, it is observed that the PSD-fit (blue curve) describe the PSD spectra as expected.

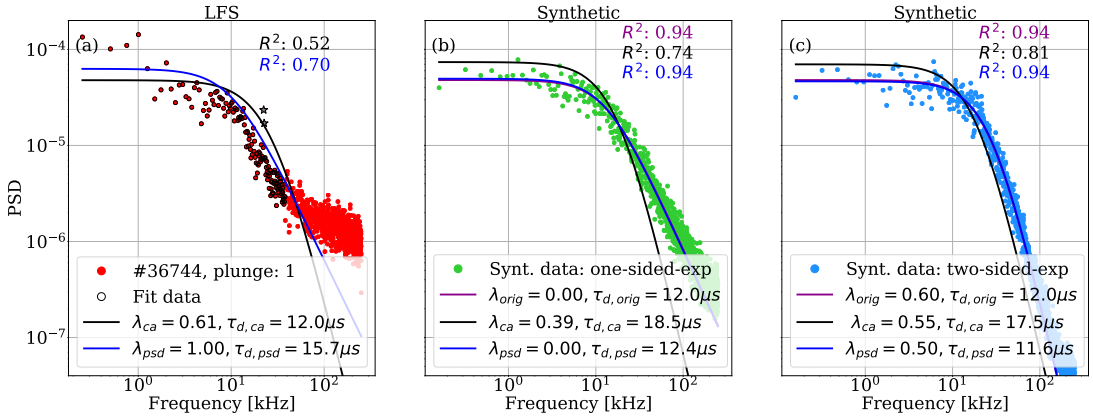

Figure 4.6: Power spectral density of (a) the measured signal with the grey stars representing electrical interference, (b) the one-sided exponential function and (c) the two-sided exponential. The blue line is an independent PSD-fit and the black line represents the curve obtained from the CA wave-form. Data points marked as stars are due to electrical interference and are not considered during the fit.

From the set of fitted parameters from both the CA wave-form and the PSD-fit the ACF can be obtained. As expected the PSD-fit parameters describe the ACF very well in the case of the synthetic data. The PSD spectra and the ACF function are related by the Fourier transform and it is expected that the set of parameters that describe the PSD describe the ACF as well. The CA wave-form overestimation of the duration time ($\tau_{d,CA}$) leads to a poor fit of the ACF as expected from the PSD. Comparing the ACF of the synthetic signals to the measured signal, it is seen that the latter has a longer correlation time. While, the ACF of the synthetic data are described well by a decaying exponential function, the ACF of the measured signal shows fast decay followed by long range correlation. The fast decay again points towards noise in the signal, while the long tail indicates that the signal is not well described by independent pulses. Also, the FPP model is based on the assumption of high intermittency, thus the ideal non-overlapping synthetic signal cannot imitate the measured signal.

To investigate whether the length of a time series plays a role for the FPP model, synthetic data with shorter time series are considered in the appendix A.1. The short synthetic data are generated using the same parameter specification as given above with the exception of the parameter K. In this case, the number of arriving events is $K = 19500$. The results of this study is similar to the one shown above, showing that the FPP model can still interpret each function (CA, PSD and ACF) separately but a global description using the CA wave-form parameters is not viable for data similar to those at the X-point.

The results from the double-exponential synthetic data presented above shows that the original parameters used to generate the synthetic data is not reproduced by the CA-wave-form. To explore this inconsistency, synthetic data using a smaller intermittency parameter

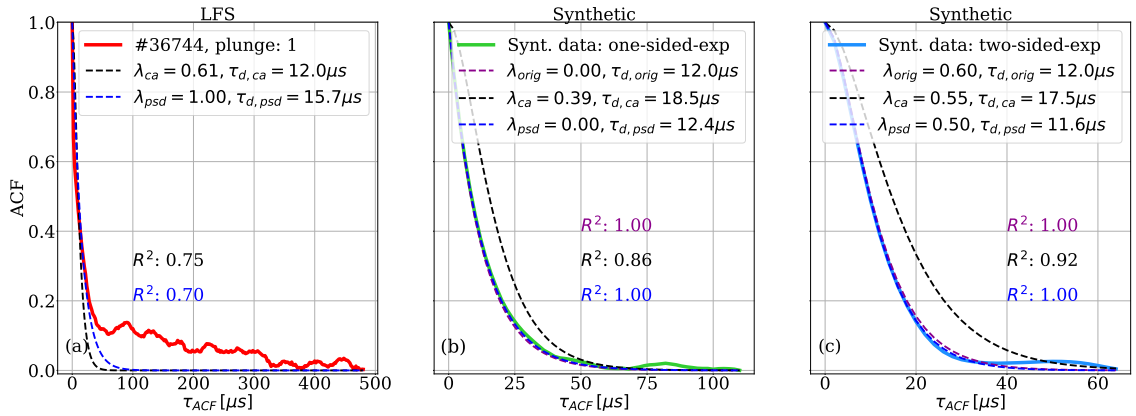

Figure 4.7: Autocorrelation function of (a) the measured signal, (b) the one-sided exponential function and (c) the two-sided exponential.

($\gamma = 1.5$) is considered (in Appendix A.2). It turns out that the smaller γ is, the more intermittent a signal is. This is because γ determines the degree of overlap in the arriving pulses. A small γ, therefore, means that there are less pulse overlapping occurring. The analysis in appendix A.2 shows that the CA wave-form agrees very well for small γ. Also, the parameters fitted from the CA wave-form and the PSD-fit describe the PSD spectra and the ACF equally good.

In the presented analysis, it was observed that the CA method overestimates the pulse duration time ($\tau_{d,CA}$ compared to $\tau_{d,PSD}$) in all cases. The γ of the measured signal on the LFS has been estimated from the skewness (based under the assumption of the FPP model) and seemed to be too large for the FPP model to work within its assumptions. In particular, the CA wave-form parameters seems to be unable to describe the PSD spectra due to pulse overlapping. The CA method averages over additional pulses that are in the tail of the primary pulse, thus, lifting the overall tail of the wave-form. In contrast, this does not occur when calculating the PSD spectra and the ACF directly. However, from figure 4.6 (a) it is seen that fitting the PSD spectra independently did not give the parameters that would describe the measured data, as the R^2 coefficient for both the PSD spectra and the ACF is 0.70. As mentioned, this is however due to noise in the measurement. Comparing figures 4.2 (a) and 4.5 (a), it seems likely that the peak in the CA wave-form is mainly due to noise. This is further reflected in the PSD spectra and the ACF (see fig. 4.6 (a) and 4.7 (a)). It is found that the FPP model works best for very intermittent signals when there is little to no pulse overlap.

4.3 Consequence for the measured data

From the synthetic data study presented in the previous section, it appears like none of the fits described the LFS measurement in the X-point region very well (as quantified by

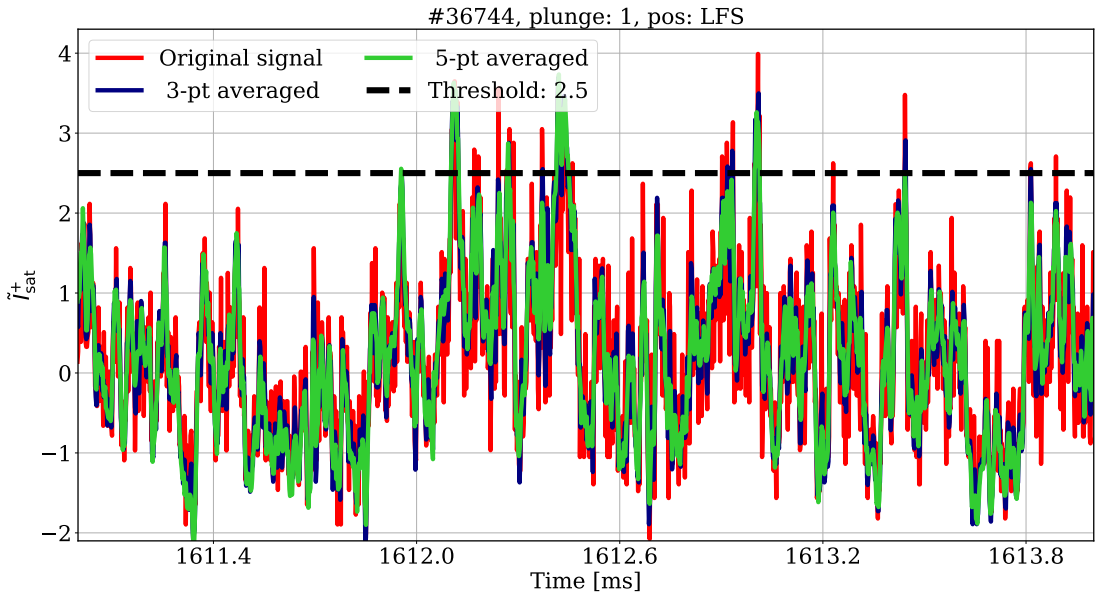

Figure 4.8: The zoomed-in of the normalized time series of the first plunge of shot #36744 in the LFS. The original time series is shown in red. The dark-blue and green colour show the 3- and 5-point average signal, respectively, before performing the normalization. The black dashed line represents the threshold value used for the conditional averaging method.

the R^2 coefficients). This is partly due to the white noise characteristics observed. In this section it is shown that this is indeed the case by running the signals through a filter. In particular, the noise reduction filter implemented is an average over a certain number of data points before normalizing the signal (see eq. (3.23)).

A simple filter is applied to the data by averaging the raw signal over 3-point and 5-point. After the filtering, the raw signals are then normalized such that the mean vanishes and the variance is one. Figure 4.8 shows a short period of the normalized LFS signal of the first plunge of shot #36744. The red line shows the raw data, i.e., without any additional noise filtering. The dark-blue and the green lines show the signal on which a 3- and 5-point averaging has been conducted, respectively. It is observed that the filtering method suppresses the spikes. The black dashed line represents the threshold value set for the conditional averaging method. The number of conditional events of the original signal reduces from 190 to 88 and 59, respectively, for the 3- and 5-point averaging method. The statistics therefore worsen with increasing filtering as expected.

The conditional averaging with a threshold of 2.5 is applied on the normalized signals and the resulting wave-forms are shown in figure 4.9. It is observed that with increasing noise filtering the peak of the original signal is broadened and the wave-form takes an exponential shape. The filtering does not seem to affect the amplitude of the waveform significantly. In figure 4.10 the wave-forms, normalized to unity by their peak value, are

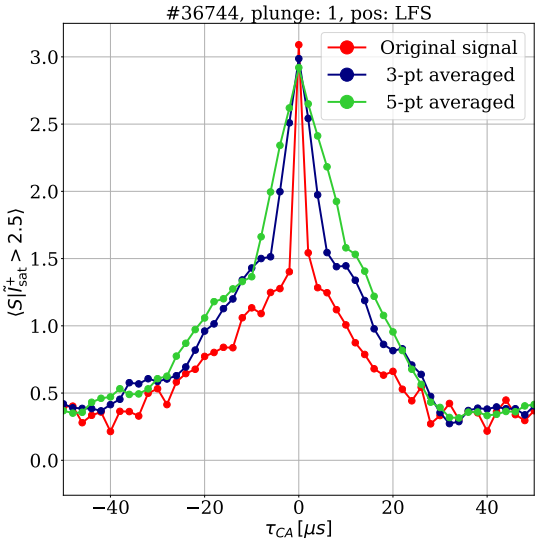

Figure 4.9: Conditionally averaged wave-form of the normalized time series for a threshold of 2.5. The wave-form of the original data is shown in red. In dark-blue and green are the wave-forms of the 3- and 5-point averaged signal, respectively.

fitted to a double-exponential. The R^2 coefficient shows that quality of the fit increases with increasing filtering but at the cost of less statistics.

In figure 4.11, it is seen that the PSD-fit (blue curve) describes the data better when noise is reduced. However, the curve obtained from the parameter of the CA wave-form (black line) still deviates from the PSD spectra. The data acquisition system has a sampling frequency of 500 kHz and the Nyquist frequency (which is half of the sampling frequency), accordingly, is 250 kHz. The averaging method works as a low-pass filter and has a cutoff of $\approx$ 83 kHz and $\approx$ 50 kHz for the 3-point and 5-point averaging, respectively. This is indicated by the purple line in figure 4.11 (b) and (c), where a steep fall and non-physical features are observed in the PSD spectra. The more data-points that are used for the averaging method, the lower the Nyquist frequency is. Thus, in order to get a better CA wave-form, the high frequency data in the PSD spectra is compromised. When fitting only the data in black is used, as the data below the 10^{-6} are effects due to the filtering. The two sets of parameters (τ_{d} and λ) obtained from the CA wave-form and the PSD are used to calculated the ACF (see eq. (3.34)). It is observed that the slope of the ACF is described better by the PSD-fit parameters after reducing the noise from the measurement. Still, the rest of the ACF ($\tau \approx 50$ - 300 μs) has not been smoothen out, showing that this is not an effect due to noise.

To summarize, as a consequence of the synthetic data study, a low-pass filter is applied on the measurements before the FPP method can be applied. It is observed that the 5-point averaging method provided the best results and, therefore, for the data analysis this method is chosen to reduce the noise. This method is used at the expense of neglecting

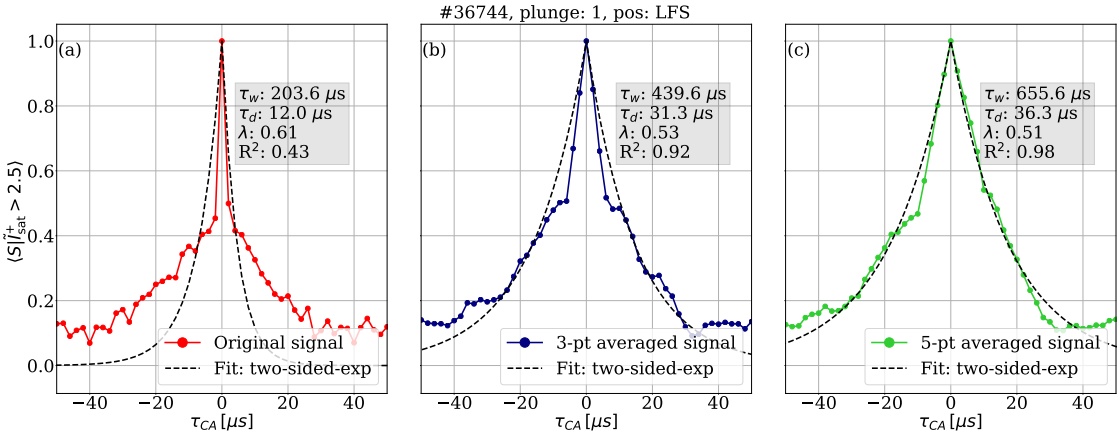

Figure 4.10: Conditionally averaged wave-forms normalized to the peak value. (a) shows the wave-form of the original signal, (b) the wave-form of the 3-point averaged signal and (c) the wave-form of the 5-point averaged signal. The black dashed line shows the double-exponential fit.

high frequency data. The 5-point averaging reduces the Nyquist frequency from 250 kHz to approximately 50 kHz. Also, most of the energy appears to be on at low frequencies and therefore, it is reasonable to cutoff at high frequencies.

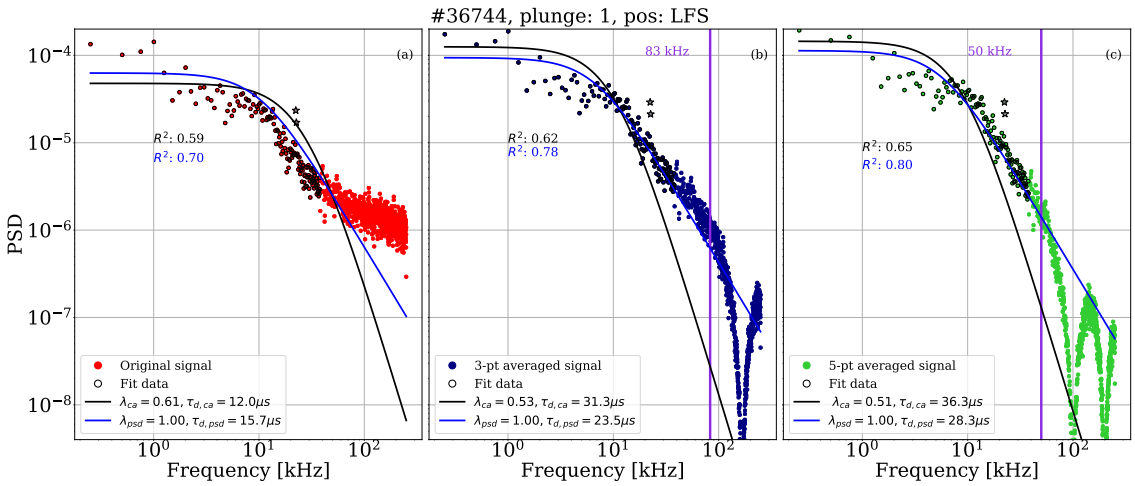

Figure 4.11: Power spectral density of (a) the original signal (b) the 3-point averaged signal and (c) the 5-point averaged signal. The fitting curves are show in black and blue colour. The purple line in (b) and (c) indicates the new Nyquist frequency as a consequence of averaging the signal.

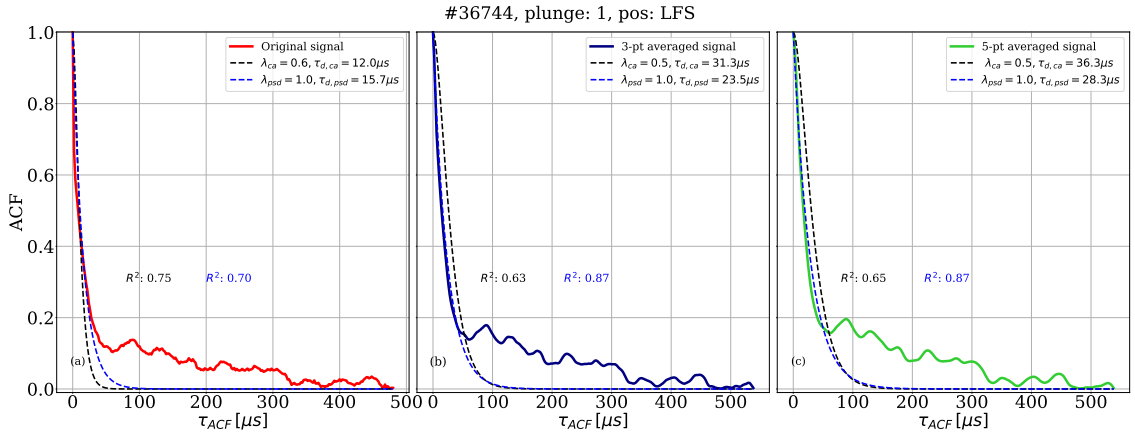

Figure 4.12: Autocorrelation function of (a) the original signal (b) the 3-point averaged signal and (c) the 5-point averaged signal. The fitting curves are shown in black and blue colour dashed lines.

Chapter 5

Results

In this chapter we present the data analysis (introduced in chapters 3 and 4) of the time series measured during shot #35466, #36736 and #36744 at ASDEX Upgrade. During the deuterium (D) shot #35466, two probe plunges were performed, while in the helium (He) shots #36736 and #36744 three plunges were made for each. The details of these experiments are listed in table 2.2 in chapter 2. We start in section 5.1 by giving an overview for determining the relative fluctuation level. In section 5.2, we discuss the time series analysis of the shots as a whole and the results are presented in the format of a paper. The fluctuations analysis of the measurements obtained during the probe-stationary phases are discussed in section 5.3 and in section 5.4 a comparison between the different plasmas are presented. Lastly, the results are discussed in section 5.5.

5.1 Relative fluctuation level

We account for shifting means in the probe-stationary time series by subtracting its running mean and normalizing by its running standard deviation. The running-moments of a signal is determined as described in section 3.2. From the first and second moments, the relative fluctuation level of the ion-saturation current $\hat{I}^+_{\mathrm{sat}}$ is given by

$$\hat{I}^+_{\mathrm{sat}} = \frac{\sigma_{I^+_{\mathrm{sat}}}}{\langle I^+_{\mathrm{sat}} \rangle}, \tag{5.1}$$

where $\langle I^+_{\mathrm{sat}} \rangle$ and $\sigma_{I^+_{\mathrm{sat}}}$ denote the mean and standard deviation, respectively.

It should be noted that during the experiments, events (like arcing) that are not related to the turbulent flow of the plasma occurs in specific periods. Data collected during these occurrence are unsuitable for analysis. In the data presented here, the probe arcing has mostly been observed during the probe retraction phases. An example of the arcing is shown in figure 3.6 (a), indicated by red arrows. Therefore, only the insertion phase is considered for analysis.

5.2 Quiescent regions at ASDEX Upgrade

5.2.1 Prelude

With the help of a fast visible imaging camera, Walkden *et al.* [87] first reported the observation of a region with very low fluctuation level located on the LFS near the X-point of MAST. A similar region has also been observed in TCV, NSTX as well as in turbulence code simulations TOKAM3X [88–91]. Since the region has only been observed by means of passive diagnostics, a study has been conducted at ASDEX Upgrade to investigate its local characteristics. These local measurements were carried out using Langmuir probes. The results of the fluctuation analysis of the probe plunges, performed during the experiments, as a whole can be found in the submitted publication [92]: *Quiescent Regions Below the X-Point on ASDEX Upgrade*. The paper has three main sections. The first section introduces the diagnostics and the experimental details. The second part provides the methodological approach and the last discuss the findings of a second region of low fluctuation level located in the PFR. The existence of the second 'quiescent' region is seen in both helium and deuterium plasmas independent of the auxiliary heating source.

Quiescent Regions Below the X-Point in ASDEX Upgrade

R. D. Nem[1], P. Manz[2], N. Vianello[3], V. Naulin[1], N. Walkden[4], J. Juul Rasmussen[1], B. Sieglin[2], A. Herrmann[2] and the ASDEX Upgrade Team[2,5]

[1]Technical University of Denmark, Kgs. Lyngby, Denmark
[2]Max Planck Institute for Plasma Physics, Boltzmannstr. 2, 85748 Garching, Germany
[3]Consorzio RFX, Padua, Italy
[4]CCFE, Culham Science Centre, Abington, OX14 3DB, United Kingdom
[5] H. Meyer et al. 2019 Nucl. Fusion 59 112014

E-mail: nishta@fysik.dtu.dk

Abstract. Probe measurements of plasma fluctuations in the divertor region of ASDEX Upgrade reveal the existence of *two* quiescent regions close to the separatrix: one in the low field side scrape-off layer and one in the high field side of the private flux region. The X-point manipulator at ASDEX Upgrade makes it possible to obtain continuous measurements of the ion-saturation current from the low field side scrape-off layer through the private flux region and into the high field side scrape-off layer. We observe a smaller fluctuation level of the ion-saturation current the closer the probe is to the low field side separatrix supporting the existence of a quiescent region similar to what is observed in other tokamaks. We also report the finding of a second quiescent region in the high field side private flux region. The formation of the quiescent regions is observed in both helium and deuterium plasmas and is independent of the heating source (electron-cyclotron resonance and neutral beam injection).

Keywords: X-point region, quiescent regions, private flux region, fluctuations, ASDEX Upgrade tokamak, Divertor region, X-point manipulator

1. Introduction

In tokamaks with a divertor configuration, plasmas are categorised into three regions: the core, the scrape-off layer (SOL) and the private flux region (PFR). The core is the region where the plasma is confined by magnetic field lines. The SOL is characterised by the flow of plasma along the 'open' magnetic field lines towards the plasma facing components (PFCs). The private flux region is located below the X-point and is geometrically restricted by the two legs formed by the separatrix. At the upstream SOL, the cross-field transport has been identified as being non-diffusive [1, 2]. Non-diffusive

turbulent transport is associated with filamentary structures also known as 'plasma blobs'. As a result of interchange turbulence, the filaments emerge from the low field side (LFS) edge of the plasma and subsequently flow into the SOL [3]. Measurements have shown that the filament properties change with density [4]. At high density, a regime of increased filamentary transport leads to a shoulder formation [4, 5]. The shoulder formation is an active field of research, since ITER and DEMO will be operated at high densities and will feature detached divertors [4]. The filamentary transport also influences the ratios of parallel to perpendicular particle and heat fluxes [6]. This determines the confinement of the plasma and the power-deposition area on the PFCs, which in turn, has a significant impact on the lifetime of the PFCs [7]. To be able to quantify the erosion of the PFC material, statistics of the plasma fluxes to the PFCs and measurements of the fluctuating quantities in the SOL turbulence are important. Whilst significant progress has been made towards a comprehensive understanding of SOL physics, some uncertainties remain in part due to a lack of measurements around the X-point.

The presence of the X-point influcences the filamentary structures and the turbulence in the SOL making it a crucial region to investigate. Strong magnetic shearing near the X-point causes the flux tubes to shear into ribbon like structures [8]. This makes it difficult for macroscopic instabilities to exist in the SOL close to the X-point [8, 9] and results in a quiescent region on the LFS. The presence of a quiescent region was first reported for MAST by Walkden et al. [12], where L-mode data taken with a high speed visible imaging camera showed fewer filaments in the vicinity of the X-point in the LFS SOL. In the near SOL this tubulence can be disconnected from the upstream filaments due to the presence of the X-point [10–12].

Measurements in MAST, NSTX and TCV show a quiescent region close to the X-point in the SOL in lower single null L-mode shots [12–15]. The quiescent region in the LFS SOL has also been seen in simulations carried out using the 3D fluid turbulence code TOKAM3X [16–18].

The X-point manipulator (XPM) at ASDEX Upgrade increases the poloidal diagnostics coverage and allows active measurements in the X-point region. In this paper, we present experimental data in the X-point region of ASDEX Upgrade tokamak to investigate the fluctuation amplitudes. Therefore, measurements through both the LFS and high field side (HFS) SOL as well as in the PFR are considered. This paper is structured as follows: the experimental setup is briefly described and the experimental details of the shots are given in section 2. Section 3 introduces the methodological approach. In section 4, the results obtained from Langmuir probes mounted on the XPM are presented. The latter are discussed in section 5.

2. Diagnostic and experimental details

The divertor region of the poloidal cross-section of ASDEX Upgrade is shown in Fig. 1 (a). The XPM trajectory, represented by the black line, is located at $z = -0.965$ m

in sector 10 of ASDEX Upgrade. The XPM reciprocates horizontally through the divertor entrance, starting from the LFS wall at a major radius of $R = 1.645$ m with a maximum insertion distance of $R = 1.356$ m on the HFS. For a typical magnetic equilibrium configuration the XPM moves just below the X-point. More information on the XPM can be found in [19–21]. A full probe plunge covers approximately 30 cm in the vacuum vessel allowing measurements in both the LFS- and the HFS SOL, as well as in the intermediate PFR. A maximum of three plunges are performed per plasma shot to avoid overheating of the probe head. The probe head consists of three cylindrical Langmuir probe pins. Two of which are in a Mach configuration (pin 1 and pin 2) and one freestanding (pin 3). The latter is swept at a frequency of 1 kHz between approximately $\pm$ 130 V to measure current-voltage (I-V) characteristic curves. The probe head configuration and the direction of the toroidal magnetic field are shown in Fig. 1 (b). The Langmuir probe pins are approximately 2 mm long with a diameter of 1 mm. The area A of the probes are $\approx 6.6 \times 10^{-6}\mathrm{m}^2$. The graphite wall is 4 mm high and 0.9 mm wide. The distances between the pins and the center of the wall are denoted by x and y, where $x = 1.15$ mm and $y = 2.55$ mm.

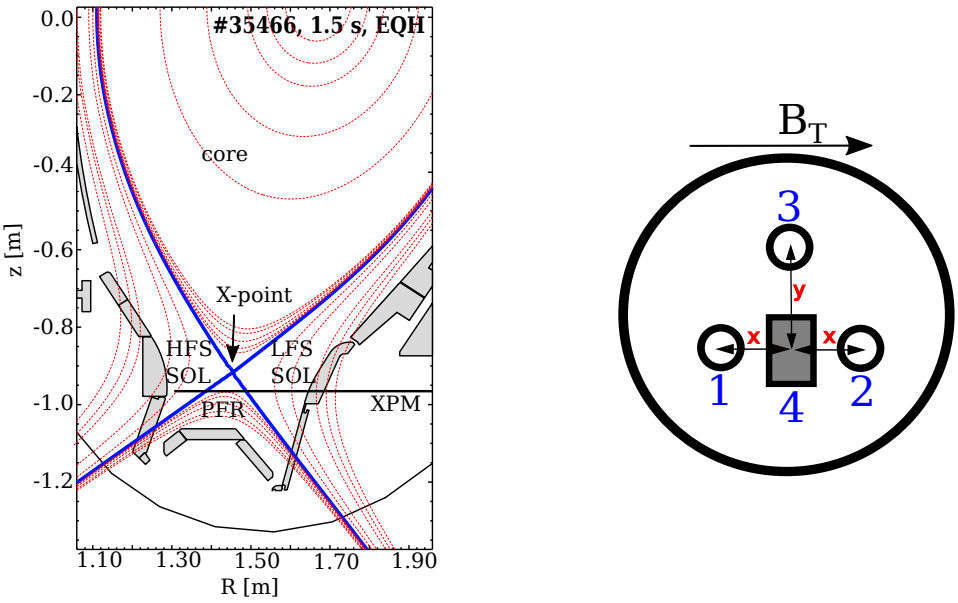

(a) (b)

Figure 1: (a) The divertor poloidal cross-section of ASDEX Upgrade together with the magnetic equilibrium-configuration of shot #35466 and (b) the mounted configuration of the probe head and the direction of the toroidal magnetic field B_T. Pin 1 and 2 are in Mach configuration, while pin 3 is swept and 4 represents a graphite wall. $x = 1.15$ mm and $y = 2.55$ mm.

We consider three different L-mode plasmas in a lower single null configuration. The details of the shots are listed in Tab. **??**. Shot #35466 is a deuterium (D) plasma with

electron-cyclotron-resonance heating (ECRH). Shots #36736 and #36744 are helium (He) plasmas with ECRH and neutral-beam injection (NBI) heating, respectively.

3. Data analysis

The time trace of the ion-saturation current I^+_{sat}, from the first plunge of the He plasma (#36744) is shown in Fig. 2 (a). It exhibits three stationary measurements of 20 ms in the insertion phase in each of the three regions below the X-point, namely the LFS SOL, PFR and the HFS SOL. The stationary phases can be identified by the plateaus in the XPM trajectory (shown in green). The PFR region is determined from equilibrium reconstruction. Only the insertion phase of the probe head is considered. During the retraction phase arcing is often observed making the data unsuitable for analysis. In Fig. 2 (b), the data used for the analysis is shown as a function of major radius R. The relative fluctuation amplitude of the ion-saturation current is defined as $\tilde{I}^+_{\mathrm{sat}} = \sigma_{I^+_{\mathrm{sat}}} / \langle I^+_{\mathrm{sat}} \rangle$, with $\langle I^+_{\mathrm{sat}} \rangle$ being the moving mean for a window of 2.4 ms and $\sigma_{I^+_{\mathrm{sat}}}$ the moving standard deviation for the same time window. The window size is chosen to be a balanced compromise between the statistics and the assumption of the probe head's stationarity. The maximum speed of the probe head is $\approx 3\,\mathrm{ms}^{-1}$. For a pin length of 2 mm, the time taken for the probe head to move the length of the pin is $\approx$ 0.7 ms. However, a window of 0.7 ms consists of merely 350 data points. In order to have sufficient statistics we therefore consider the probe head to be quasi-stationary in the window of 2.4 ms.

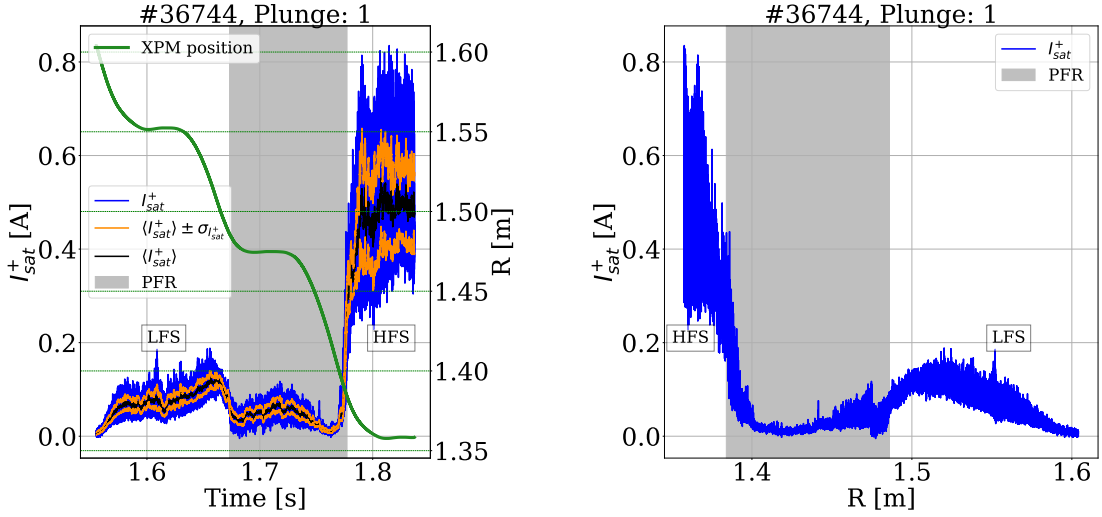

(a) (b)

Figure 2: (a) The I^+_{sat} measured by the biased Langmuir probe pin 1 during the insertion phase of the first plunge. The XPM trajectory is represented by the green line. (b) The analysis domain of I^+_{sat} is shown as a function of major radius R. The PFR is shown by the shaded region.

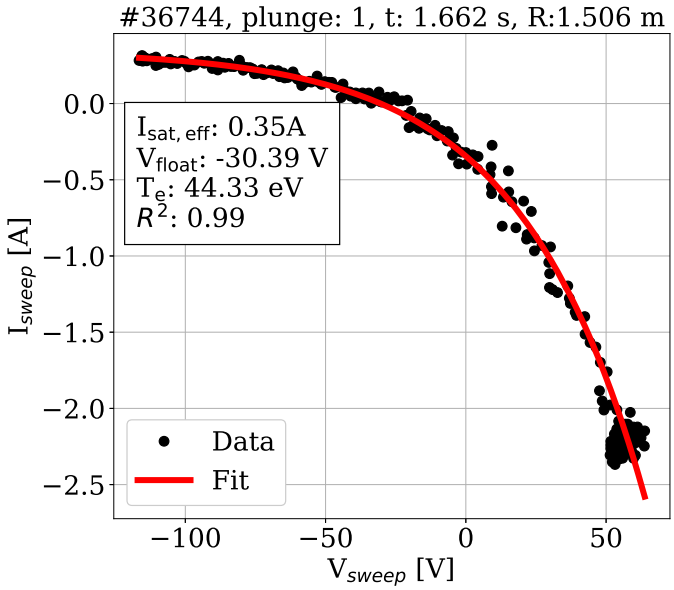

Figure 3: Example of an I-V curve (obtained at $R = 1.506$ m (see Fig. 4 (b) with $V_{\mathrm{plasma}} = 133$ V and $n_{\mathrm{e}} = 0.5 \times 10^{19}\mathrm{m}^{-3}$) during the first plunge in the He plasma #36744) and the corresponding plasma parameters.

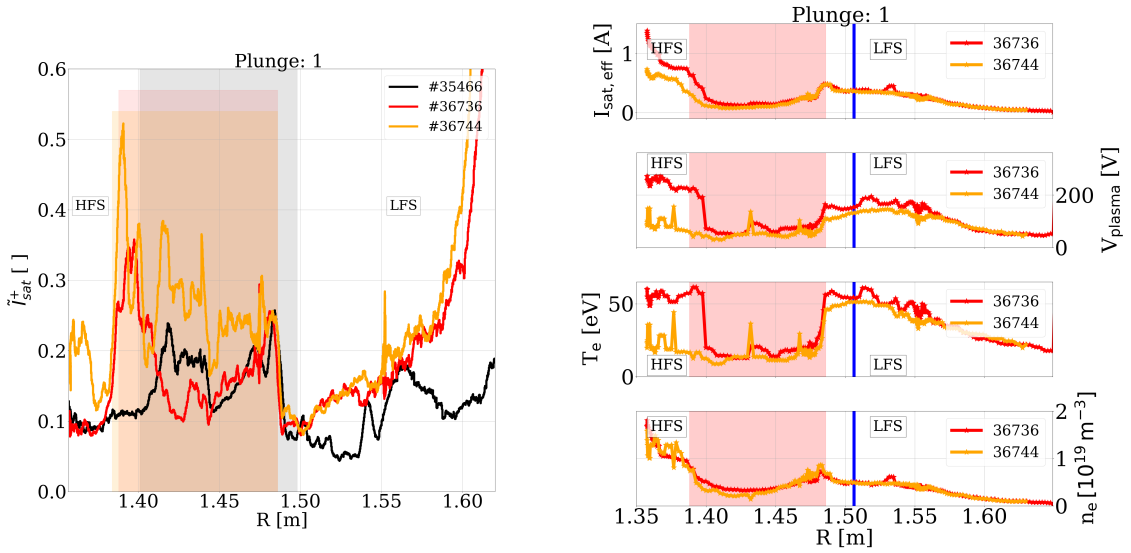

(a) (b)

Figure 4: (a) The relative fluctuation amplitude $\tilde{I}^{+}_{\mathrm{sat}}$ of the first plunge as a function of the major radius R, and (b) the profile of the plasma parameters from the swept Langmuir pin for the He plasmas (#36736 and #36744). There was no sweeping pin during the D shot #35466. The shaded regions represent the PFR of each shot and are in the same color-coding. The blue line represents the parameters of the I-V curve shown in Fig. 3.

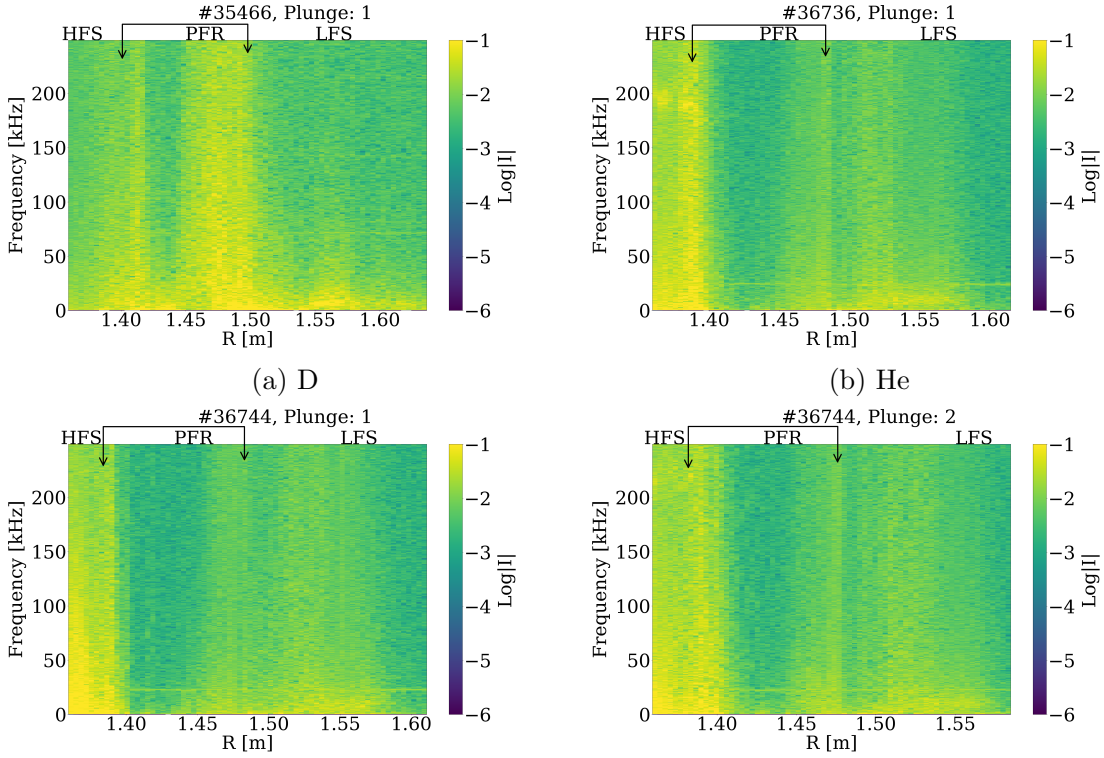

(a) D (b) He

(c) He (d) He

Figure 5: Spectrogram of I_{sat}^{+} of the first plunges of shot (a) #35466, (b) #36736 and (c) #36744, respectively, and the second plunge of shot (d) #36744. The color scale gives the amplitude I of the Fourier transform in the logarithmic scale. The private flux region is located between the arrows.

With the sweeping Langmuir probe pin, I-V characteristics are collected along the XPM trajectory. Using a standard fitting method [22], the following plasma parameters can be extracted: floating potential V_{float}, effective ion-saturation current $I_{\mathrm{sat,eff}}$, and electron temperature T_{e}. The local electron density profile n_{e}, and the plasma potential V_{plasma} are given as follows: $n_{\mathrm{e}} = \frac{I_{\mathrm{sat,eff}}}{A\,e}\left(\frac{m_{\mathrm{i}}}{2T_{\mathrm{e}}}\right)^{1/2}$ and $V_{\mathrm{plasma}} = V_{\mathrm{float}} + \gamma T_{\mathrm{e}}$, where A is the exposed area of the Langmuir probe pin and m_{i} is the ion mass. For He-4 and D plasma, γ is calculated to be approximately 3.2 and 2.8, respectively [22]. Since the electron-saturation branch is usually not measured in strongly magnetized plasma, cut-off values in the voltage and current ranges are determined to optimize the curve fitting. Fig. 3 shows an example of an I-V curve and the plasma parameters determined from fitting. Here, the cut-off values in the voltage and current range were +50 V and -1.0 A, repectively.

4. Results

The relative fluctuation amplitude of the ion-saturation current and the plasma parameters as a function of the major radius R are shown in Fig. 4. The probe head trajectory spans from the LFS (**large** R values) to the HFS (**small** R values). From the far SOL towards the LFS separatrix leg, a decreasing trend is observed in the relative fluctuation level. When entering the PFR the fluctuation level increases drastically. In fact, the lowest relative fluctuation level in the plasmas is reached at the LFS separatrix leg, providing a clear indication for the presence of a quiescent region just before the PFR. It should be noted that the difference in the trend of the fluctuation level in the LFS SOL between the He and D plasmas might be due to the different divertor conditions. Compressions of impurities in the divertor can be different depending on the fuelling gas [23]. The relative fluctuation levels are elevated in the PFR (shaded region). This is also observed in the second and third plunges of all three shots. Fig. 4 (b) indicates that the elevated fluctuation level is followed by a drop in both temperature and density. A steep temperature drop is observed in the PFR, but the density drop is not as significant as the temperature drop. The temperature drops by approximately 60% while the density changes by approximately 30%.

In the HFS SOL, the relative fluctuation level of the NBI heated plasmas (#36744) is double of that of the ECRH plasmas (#35466, #36736). This pronounced difference is also reflected in the plasma parameters. Analysis of data from Langmuir probes embedded in the ASDEX Upgrade divertor showed that none of the plasma scenarios presented were in full detachment. This indicates that detachment might not be the reason for the discrepency on the HFS SOL. The reason for large difference in fluctuation between the two heating schemes influencing only the HFS conditions is not clear and would need further dedicated investigations.

4.1. Spectral Analysis

A spectral analysis is performed on the ion-saturation current with the results presented in Fig. 5. The amplitude, I, on the HFS for the He plasmas (for $R < 1.40$ m for both plunge 1 and 2) is larger compared to that in the LFS SOL and PFR. A similar trend is observed for the density (see Fig. 2 and note that $n_e \propto I_{sat}^{+}$), where we see the ion-saturation current measured in the HFS SOL is larger compared to the LFS SOL for the He plasmas. For the D plasma, the amplitude is smaller on the HFS SOL compared to the He plasmas. This is due to the low ion-saturation current measured on the HFS SOL during the D plasma.

In general, we also observe an increase in the fluctuation level close to the inner separatrix leg on the HFS. The large fluctuation amplitudes could be interchange-driven turbulence as the pressure gradient and magnetic curvature vector are anti parallel in this region.

Interestingly, two bands with low fluctuation amplitudes are observed in all shots. Both of these bands extend to almost the entire frequency range. The first band appears

right before the PFR (i.e before crossing the LFS separatrix) and the second band, which is more pronounced, appears in the HFS PFR. In the He plasma (#36744), the first band is more visible in Fig. 5 (d) compared to Fig. 5 (c). The two bands are observed for all plunges made during the three shots. It should be noted that the turbulence appears rather broadband. No modes are detected with the exception of a mode appearing on the HFS around 200 kHz in Fig. 5 (b). This mode is also observed at the HFS midplane by reflectrometry. The interpretation of this mode will need further investigation and is beyond the scope of this paper.

The first band shows the presence of the quiescent region observed in Fig. 4 (a), whereas the second band indicates yet another quiescent region located in the PFR. We defer the discussion of this region to section 5.

Since the observed quiescent regions extend to the entire explored frequency range, we integrate the amplitude of the fluctuations over all frequencies to make them more visible, i.e $\int_f \mathrm{Log(I)}\,\mathrm{d}f$. Figure 6 (a) and (b) show the profiles of the integrated amplitudes for both the first and the second plunge. Both regions are now clearly visible. The drop in amplitude close to the LFS separatrix leg (right arrows in Fig. 6) supports the presence of a quiescent region as also observed in other tokamaks [12–15]. The second drop in amplitude in the HFS PFR (left arrows in Fig. 6) supports yet another quiescent region, which has, to the authors' knowledge, not been reported before.

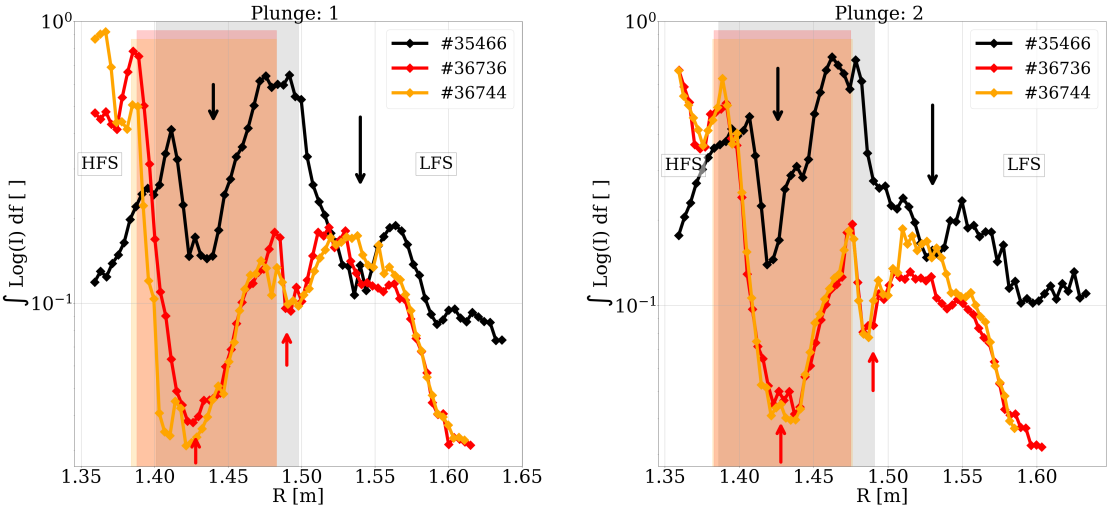

(a) (b)

Figure 6: The integrated amplitude I as a function of major radius R during (a) the first plunge and (b) during the second plunge of shots #35466, #36736, and #36744. The PFR is marked by the shaded areas.

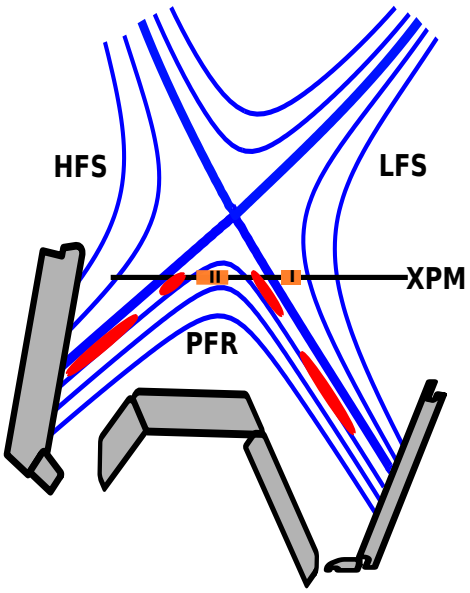

Figure 7: Schematics of the approximate position of the two quiescent regions in the poloidal cross-section of ASDEX Upgrade's divertor region. The magnetic field lines are represented in blue and the XPM trajectory is shown by the black line. Filaments that are generated in the HFS separatrix leg and propagating radially towards the LFS are coloured in red. The approximate position of the *two* quiescent regions are illustrated by the orange boxes and are marked by 'I' and 'II'.

5. Discussion and Conclusion

The X-point manipulator at ASDEX Upgrade increases the poloidal diagnostic coverage in the X-point region. Using a Langmuir probe, the ion-saturation current has been measured from the LFS to the HFS via the PFR. On the LFS, the relative fluctuation level decreases before the separatrix leg is crossed (see Fig. 4 (a)), giving the first indication of a quiescent region in ASDEX Upgrade. The first quiescent region (indicated by orange box 'I' in Fig. 7) is most likely caused by the strong magnetic shearing around the X-point. This is consistent with the experimental observations made in MAST [12], NSTX [14, 15] and TCV [13], as well as with simulations results [16–18]. Tanaka et al. [24] also reported a decreasing fluctuation level near the separatrix. The increase of fluctuation in the LFS PFR (Fig. 4 (a), shaded region) is consistent with the observations made at JET by García-Cortés et al [25]. They performed a strike point sweep of 4 Hz at the divertor targets to allow the measurements of fluctuation profiles in the SOL and PFR using Langmuir probes embeded in the divertor targets at JET. They reported an elevated fluctuation level in the PFR compared to the LFS SOL.

Furthermore, a decrease in the fluctation amplitude close to the HFS separatrix leg (1.40 m $<$ R $<$ 1.45 m) has been identified by the means of spectral analysis (see Fig. 5 and 6). This supports the existence of a quiescent region located in the PFR (indicated by orange box 'II' in Fig. 7). However, the underlying mechanism for the

existence of the second quiescent region in the PFR seems to be different from the first one observed in the LFS SOL. We observe that the decrease in the PFR (Fig. 6(a)) occurs at $R \approx 1.42$ m whereas at this position in Fig. 4 (a), the relative fluctuation levels are elevated, especially for shots #35466 and #36744.

Before crossing the HFS separatrix leg, the amplitude of the fluctuations increases again, indicating a turbulent HFS PFR at ASDEX Upgrade. Harisson et al. [26, 27] reported a turbulent PFR on the HFS in MAST, where primary filaments are created on the inner separatrix leg and eject secondary filamanets deeper into the PFR. A damping of filaments in the HFS PFR was observed by simulation [16] and has been related to an inefficient turbulent transport of filaments towards the PFR. The exact nature of the second quiescent region is unknown. However, a possible explanation is illustrated in Fig. 7. There is no source of instability in the center of the PFR as the gradients are relatively flat. Turbulence in this region, therefore has to be generated somewhere else and propagate into this region. In the PFR, the pressure gradients are only steep close to the separatrix legs. It is therefore, expected that filaments in the PFR are created in the region of bad curvature close to the inner separatrix leg on the HFS by the interchange instability as proposed in [26,27]. Also Kelvin Helmholtz instabilities may be excited across the inner separatrix leg due to sheared E×B flows generated by the electron temperature gradient at the inner divertor target. The filaments generated at the inner separatrix leg mainly propagate parallel to the magnetic field lines towards the inner and the outer divertor target. Therefore, they stay close to the separatrix leg. The filaments propagating from the inner leg to the outer divertor target are seen at the height of the X-point manipulator on the left hand side of region II. Primary filaments propagating close the X-point maybe shredded here. These might lead to secondary smaller filaments propagating to the outer leg generating the turbulence between region I and II. It is likely that the filaments do not propagate far enough into the PFR, thus resulting in a low turbulence, i.e a quiescent region.

To summarize, from the experiments carried out at ASDEX Upgrade, two quiescent regions are observed in both deuterium and helium plasmas. Two measurements from helium plasmas are presented, one with electron-cyclotron-resonance and another heated with neutral-beam injection heating. The formation of the quiescent regions is found to exist in both helium and deuterium plasmas and is independent of the heating source. It therefore seems likely that it is a consequence of the magnetic configuration and thus its formation should be independent of the heating source and plasma ion type. One interesting direction would be to carry out a similar experiment in a hydrogen plasma to investigate whether the formation of the quiescent region is independent of the plasma ion type. It is also possible that the quiescent region extends on the magnetic flux surfaces in the PFR and should be investigated with more experimental data. Also, for further experiments it can be more useful to plan the stationary measurements on the HFS PFR. It could be interesting to scan the PFR at different distance below the X-point, to investigate if there is any dependence of the second quiescent region in the vertical direction. Finally, it could be interesting to investigate whether the formation of

the quiescent regions has an effect on the power deposition on the PFCs. To investigate the mechanism behind the existence of the quiescent region in the HFS PFR, thus calls for more experimental data.

Acknowledgments

This work has been carried out within the framework of the EUROfusion Consortium and has received funding from the Euratom research and training programme 2014-2018 and 2019-2020 under grant agreement No 633053. The views and opinions expressed herein do not necessarily reflect those of the European Commission. We would like to thank D. Brida, M. Wiesenberger, L. Gil and A. H. Nielsen for their fruitful discussions.

References

[1] V. Naulin, *Turbulent transport and the plasma edge*, 2007 J. Nucl. Mater. 363-365 24-31
[2] O.E. Garcia, *Turbulent transport in the TCV SOL*, 2007 J. Nucl. Mater. 363-365 575
[3] O.E. Garcia et al., *Interchange turbulence in the TCV scrape-off layer*, 2006 Plasma Phys. Control. Fus. 48, L1
[4] D. Carralero et al., *An experimental investigation of the large density transition of the scrape-off layer transport in ASDEX Upgrade*, 2014 Nucl. Fusion 54 123005
[5] N. Vianello et al., *Scrape-off layer transport and filament characteristics in high-density tokamak regimes*, 2019 Nucl. Fusion 60 016001
[6] D. Carralero et al., *Experimental Validation of a Filament Transport Model in Turbulent Magnetized Plasmas*, 2015 Phys. Rev. Letter 115
[7] P.C. Stangeby et al., *Plasma boundary phenomena in tokamaks*, 1990 Nucl. Fusion 30 1225
[8] D. Farina et al., *Effect of the magnetic field geometry on the flute-like perturbations near the divertor X point*, 1993 Nucl. Fusion 33 1315-1317
[9] M.V. Umansky et al., *Simulation of turbulence in the divertor region of tokamak edge plasma*, 2005 J. of Nucl. Mater. 337-339 266–270
[10] R.J. Maqueda et al., *Edge turbulence measurements in NSTX by gas puff imaging*, 2001 Rev. Sci. Instrum. 72 931
[11] Terry J.L. et al., *Observations of the turbulence in the scrape-off-layer of Alcator C-Mod and comparisons with simulation*, 2003 Phys. Plasmas 10 1739
[12] N.R. Walkden et al., *Quiescence near the X-point of MAST measured by high speed visible imaging*, 2017 Nucl. Fusion 57 126028
[13] N.R. Walkden et al., *Fluctuation characteristics of the TCV snowflake divertor measured with high speed visible imaging*, 2018 Plasma Phys. Control. Fusion 60 115008
[14] F. Scotti et al., *Divertor leg filaments in NSTX-U*, 2018 Nucl. Fusion 58 126028
[15] F. Scotti et al., *Disconnection of scrape off layer turbulence between the outer midplane and divertor target plate in NSTX*, 2020 Nucl. Fusion 60 026004
[16] D. Galassi et al., *Drive of parallel flows by turbulence and large-scale E×B transverse transport in divertor geometry*, 2017 Nucl. Fusion 57 036029
[17] D. Galassi et al., *Tokamak Edge Plasma Turbulence Interaction with Magnetic X-Point in 3D Global Simulations*, 2019 Fluids 4, 50
[18] F. Nespoli et al., *3D structure and dynamics of filaments in turbulence simulations of WEST diverted plasmas*, 2019 Nucl. Fusion 59 096006
[19] M. Tsalas et al., *Langmuir probe measurements in the lower x-point vicinity of the ASDEX Upgrade divertor*, 2005 J. of Nucl. Mater. 337-339 751-755

[20] M. Tsalas et al., *Divertor plasma flow near the lower x-point in ASDEX Upgrade*, 2007 Plasma Phys. ontrol. Fusion 49 857-872

[21] S. H. Mueller et al., *Direct observations of L-I-H and H-I-L transitions with the X-point reciprocating probe in ASDEX Upgrade*, 2014 Phys. Plasmas 21 042301

[22] J. Wesson, *Tokamaks*, Clarendon-press-Oxford 2004 3rd edition, section 9.2 and 10.9

[23] H-S. Bosch et al., *Particle exhaust studies in ASDEX Upgrade*, 1997 Plasma Phys. Control. Fusion 39 1771-1792

[24] H. Tanaka et al., *Statistical analysis of fluctuation characteristics at high- and low-field sides in L-mode SOL plasmas of JT-60U*, 2009 Nucl. Fusion 49 065017

[25] I. García-Cortés et al., *Characterization of fluctuations in the JET Divertor plasmas with Langmuir probes*, 1996 Plasma Phys. Control. Fusion 2051-2062 38

[26] J. R. Harisson et al., *Filamentary transport in the private flux region in MAST*, 2015 J. of Nucl. Mater. 463 757-760

[27] J. R. Harisson et al., *The appearance and propagation of filaments in the private flux region in Mega Amp Spherical Tokamak*, 2015 Phys. Plasmas 22 092508 205002

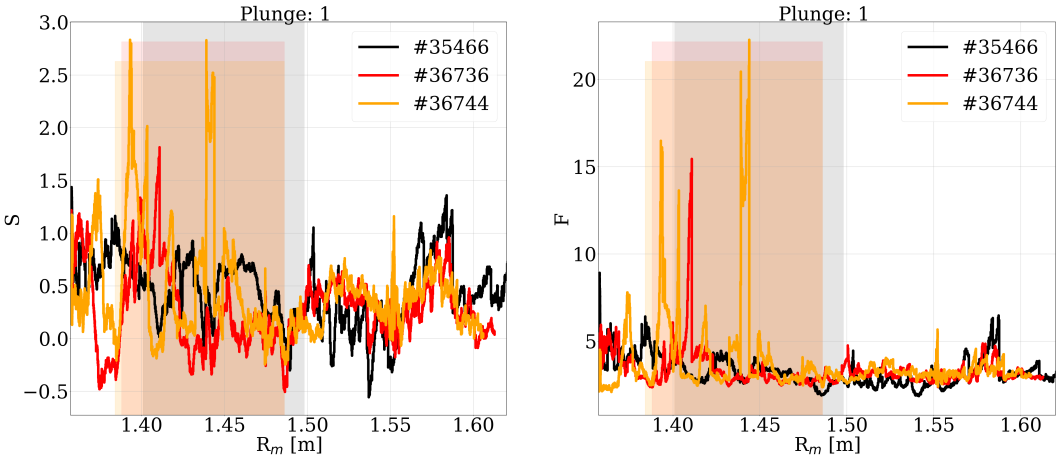

(a) (b)

Figure 5.1: (a) The skewness S, and (b) the flatness F of the data observed during the first plunge of shot #35466, #36736 and #36744 respectively.

5.2.2 Postlude

Statistical analysis of the ion-saturation current in several experimental fusion devices with different plasma parameters and magnetic configurations have shown that the skewness and flatness of fluctuations are correlated by a parabolic relation at the mid-plane [93–95]. This relation given by equation (3.22) arises in turbulent conditions, where fluctuations can be well described by a Gamma distribution. In the following, this parabolic relationship is investigated for the data presented in the paper [92]. The third (skewness S) and the fourth (flatness F) statistical moments of the time series of shot #35466, #36736 and #36744 are shown in Figure 5.1 (a) and (b) as a function of the major radius R_{m}. The largest values of the skewness and flatness are observed in the PFR during the He-shots (#36736 and #36744). Figure 5.2 shows a scatter plot of the skewness and flatness of the different data series and together with the parabolic function plotted in blue. It is evident that the parabolic relationship holds in the X-point region. However, the points with large skewness and flatness located in the PFR (as seen in fig. 5.1 (a) and (b)) deviates from the parabolic line. The deviation might be due to the 200 kHz mode that has been observed and will be discussed in section 5.4. A positive value of the skewness can be interpreted as density enhancement events, i.e., samples of filamentary structures, while a negative skewness is ascribed to holes (density depletion events) [95–97]. The measurements are mainly dominated by density enhancing filaments.

The Mach probe configuration allows for plasma flow measurements. Figure 5.3 shows the mean Mach number $\langle M \rangle$ profile of the ion-saturation current given by equation (1.14). The Mach number increases from the far SOL towards the separatrix but reduces significantly in the PFR. On the HFS, a clear difference between the profiles can be observed, as the mean Mach number increases significantly for the He shots (#36736 and #36744) compared to

the D shot (#35466). Also, since the mean Mach values are mostly above one, particles from the mid-plane are flowing at sonic speed towards the divertor. Since no detachment was observed, there was no flow from the divertor towards the mid-plane.

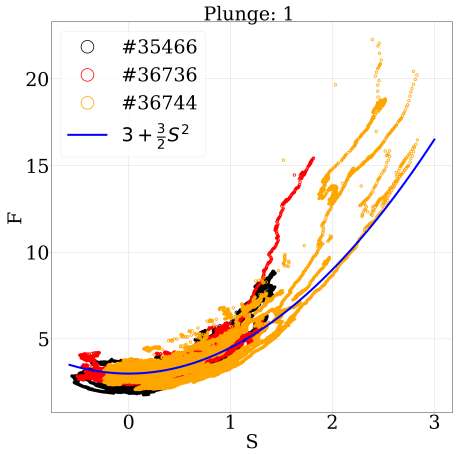

Figure 5.2: Scatter plot of the flatness F as a function of the skewness S. The parabolic relation between the two moments is shown by the blue line.

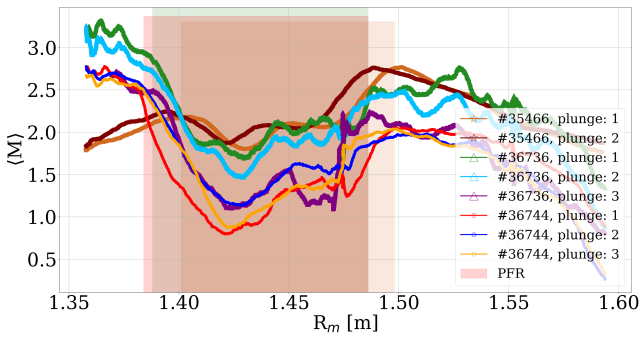

Figure 5.3: The mean profile of the Mach number for the different shots: D-ECRH (#35466), the He-ECRH (#36736) and He-NBI (#36744). The shaded regions represent the average PFR of each shot.

5.3 Fluctuation statistics of the probe-stationary phases

In this section, the methods of the filtered Poisson process (FPP) are applied to the data obtained during the first plunge of shot #36744. The synthetic data study (see chap. 4), showed that the normalized raw data from the LFS SOL has similar characteristics as that of a white noise signal. Attenuating the high frequencies by a filtering process, it was found that both the conditional averaged (CA) signal and the Fourier pair (i.e., power spectral density (PSD) and autocorrelation function (ACF)) described the data well individually. Moreover, the regime of validity of the FPP model, i.e., the mapping of the parameter pairs from the CA wave-form to the PSD and ACF remained out of reach due to a high degree of overlapping pulses in the signals.

In the following all the signals have been pre-filtered and normalized as described in section 3.2.2. The measurements on the HFS have a better signal-to-noise ratio as the ion-saturation current measured in the helium shots were much larger compared to the LFS and PFR region (see fig. 5.4 (a) and fig. B.5). However, the 5-point averaging method is implemented on all signals to bring them on equal footing.

Figure 5.4 (a) shows the raw ion-saturation current I_{sat}^{+} measured by the biased Langmuir pin 1 during the first plunge of shot #36744, where a He plasma was created. The signal of the whole plunge is shown in black and the position of the XPM is shown in green. The planed probe-stationary phases are seen as plateaus in the XPM trajectory. Each located in different region and colour coded accordingly. In the following the data collected during the probe-stationary phases will be referred to as the *static signals*. To begin with we consider the raw static signals i.e., without any filtering and normalization. The relative fluctuation level, given by equation (5.1), of the raw data in each of the regions is determined to be 0.30 for the LFS SOL, 0.25 in the PFR and 0.18 for the HFS SOL. This indicates that the signals are not pure white noise.

Even though the probe was at a fixed position, it is important to account for a moving mean in the signals. Therefore, each static measurement is now divided into ten non-overlapping windows and normalized (see sec. 3.2.2). The filtered normalized static ion-saturation current signals ($\tilde{I}_{\mathrm{sat}}^{+}$) are shown in figure 5.4 (b), (c) and (d). The time interval of the time series in the LFS SOL, PFR and HFS SOL are approximately 39 ms, 32 ms and 26 ms, respectively. The static signals in the LFS SOL and the PFR region shows a Gaussian-like behaviour as the signal varies, symmetrically around zero. The skewness S and flatness F also indicate that the data is almost distributed according to a Gaussian distribution ($S = 0$ and $F = 3$). However, the signal on the HFS SOL shows a non-Gaussian behaviour as the variation around zero is not symmetric and the signal seems to be dominated by positive bursts. This is also reflected in the skewness and flatness.

One way to check the statistical stationarity of the measured signal is to inspect when the time-lag of the ACF reaches zero for the first time. The rate of decay of the ACF may be used as a measure of the trend in a data series. A very slow decay (i.e., long time-lag) is usually observed for non-stationary time series and vice versus. Figure 5.5 shows the decaying slope of the ACF determined for the filtered normalized time series shown in

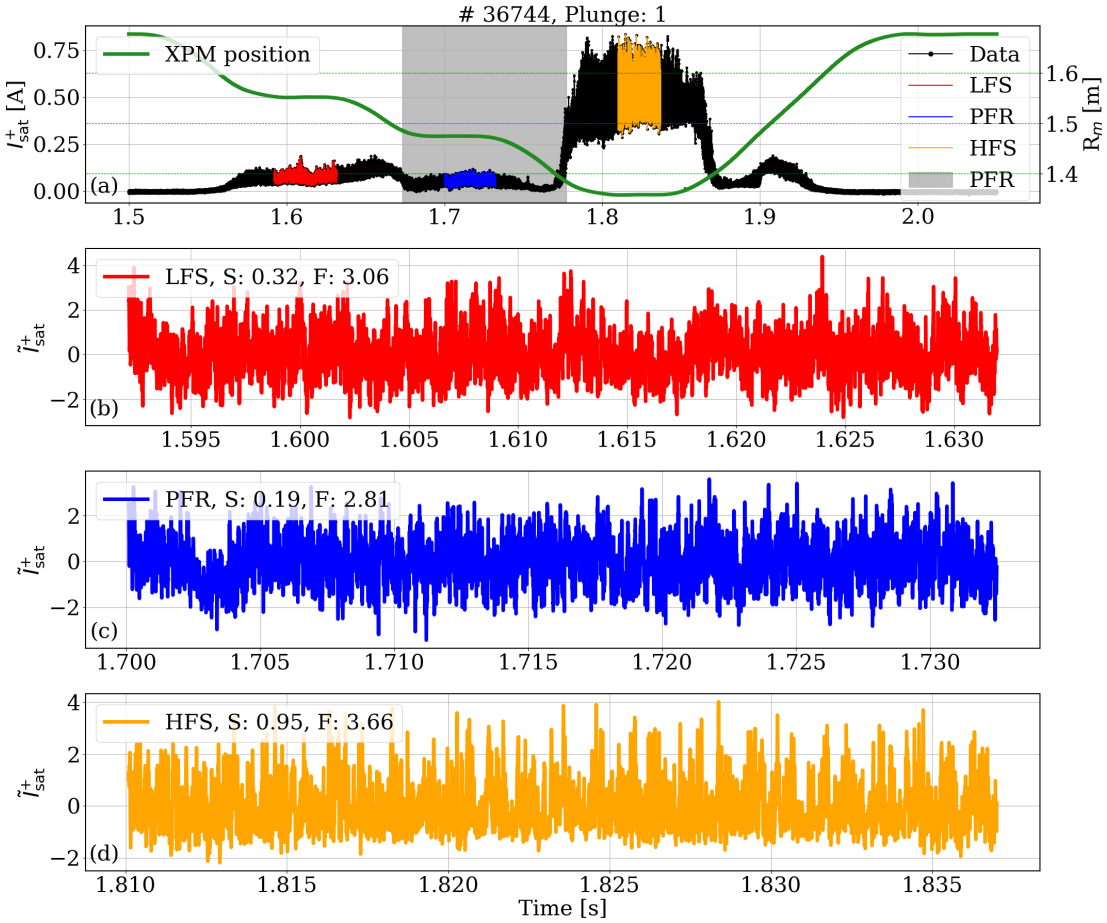

Figure 5.4: Example of a raw ion-saturation current I^+_{sat} measured by the biased Langmuir pin (a) and the three filtered and normalized static-signals ($\tilde{I}^+_{\mathrm{sat}}$) measured in the LFS SOL (b), PFR (c) and the HFS SOL (d). The skewness S and the flatness F of each static-signal is given.

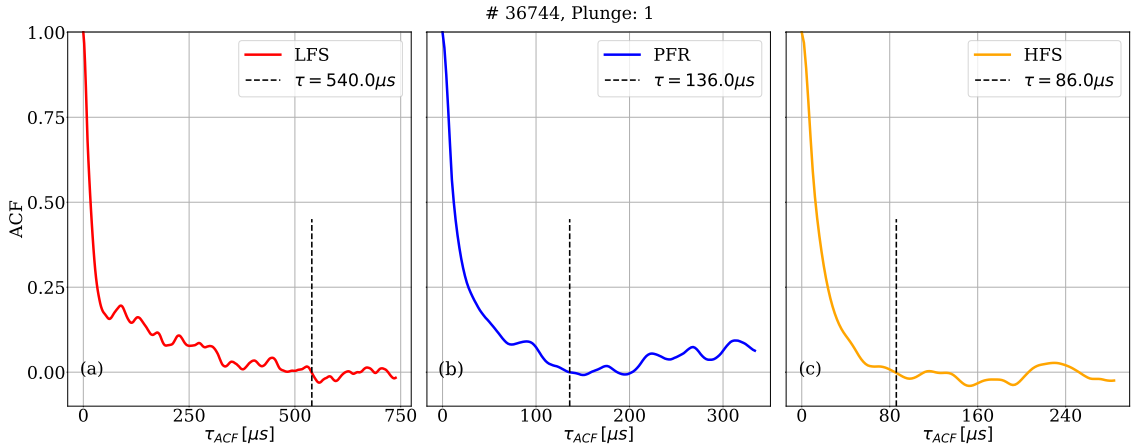

Figure 5.5: The autocorrelation function calculated for each of the filtered normalized static signals in the three different regions, the LFS SOL (a), PFR (b) and the HFS SOL (c). The dashed line gives the lag time at which the ACF reaches zero for the first time.

figure 5.4. The black dashed line marks the ACF time-lag τ_{ACF} where the ACF becomes zero for the first time. Comparing the time-lag with the interval of the individual time series, the signal may be assumed to be statistically stationary as 540μs $\ll$ 32ms. The LFS SOL exhibits the longest correlation time showing that the signal might consists of correlated pulses but there might be other mechanisms causing the long range correlation which are not uncovered yet. Note that comparing the ACF of a pure noise signal (fig. 4.2 (b)) and the measured data, it is clear that the signals consist of more than pure white noise.

Building a probability density function (PDF) is a good approach to express the information contained in a time series. The PDF accounts for how often a measured variable takes on a specific value. A way of characterising filementary structures in time series is by the degree of intermittency, i.e., the non-Gaussian character of the signal. The intermittency can be determined by constructing the PDF and calculating the higher order moments (S and F). A positively skewed PDF is usually interpreted as the signature of propagating filamentary structures in turbulent plasmas while a negatively skewed PDF may be interpreted as the creation of holes (density minima). The larger the intermittency parameter γ, is the closer the distribution resembles a Gaussian distribution. Given an ideal Gamma distribution, γ may be estimated from the skewness by equation (3.31). The estimated γ is used to plot the PDF using equation (3.30) and the goodness of the fits are given by the coefficient of determination, R^2 (see eq. (3.14)).

Figure 5.6 shows the PDFs constructed for the static signals in each of the three regions of the first plunge of shot #36744. The PDF of both the LFS SOL and the PFR are well described by a Gaussian distribution, indicating signals with no traces of filamentary structures. In contrast, the HFS SOL has the strongest intermittent turbulence during this plunge, i.e.,a small γ value which may be attributed to the creation and propagation of

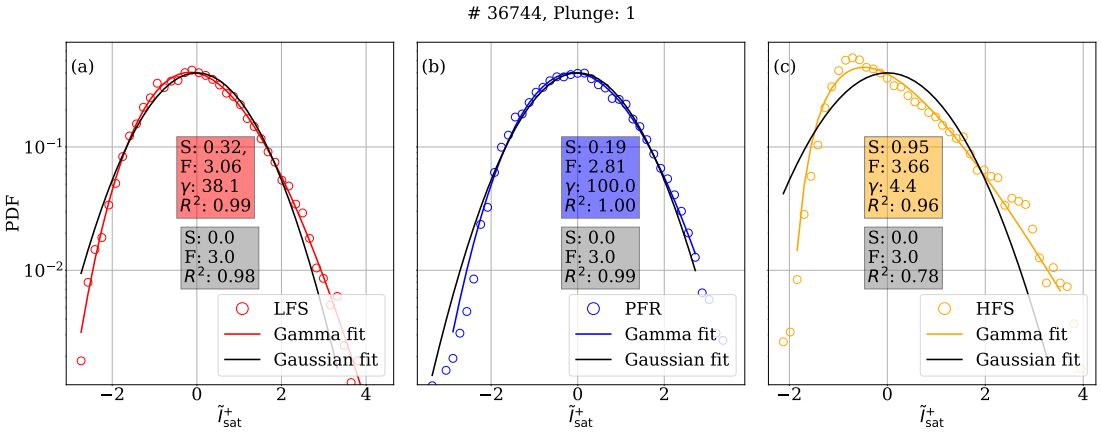

Figure 5.6: The probability density function constructed (coloured line) for each of the filtered normalized static signals in the three different regions, i.e.,the LFS SOL (a), PFR (b) and the HFS SOL (c). The ideal Gaussian (black line) is shown for comparison.

filamentary structures [7]. The relative fluctuation levels are likewise large for the LFS and PFR regions, with values of 0.30 and 0.25, respectively. This indicates a more turbulent plasma in these two regions compared to the HFS. If there are any filamentary structures in the LFS SOL and PFR these are of the order of the background density. It is worth noting that the probe-stationary phases in the PFR ended up being very close to the LFS separatrix leg, which could explain the Gaussian behaviour in this region. Note that in this case, the 5-point filtering on the LFS SOL increased the γ value from 20.2 to 38.1 whereas in the HFS SOL the γ decreased from 5.9 to 4.4.

A powerful technique to detect coherent structures in turbulent plasmas is the conditional averaging method [40, 80, 81, 98, 99]. We apply it here to get the averaged wave-form of the bursts recorded by the Langmuir probe. The CA wave-forms are determined for amplitudes exceeding a threshold value of 2.5 of the filtered-normalized ion-saturation current $\tilde{I}^+_{\text{sat}}$. At this threshold, the number of conditional events encountered in the LFS SOL, PFR and HFS SOL static signals are 59, 47 and 60, respectively. Figure 5.7 shows the CA wave-forms of the three regions. The black dotted line represents a curve-fit of a double-exponential function given by equation (3.29). The wave-forms are normalized to their respective peak values. The fitting parameters, $\tau_{d,CA}$ and λ_{CA}, are the duration time and the asymmetry parameter parametrizing the wave-form. $\tau_{d,CA}$ gives the approximate burst duration of the average filamentary structure. The mean waiting time in between pulse is noted by τ_w and the goodness of the fit is given by the R^2 coefficient. With $R^2 > 0.95$, it is observed that all wave-forms are well described by the double-exponential fit.

To further characterize the fluctuations of the signals we consider the PSD spectrum and its dual description in term of the ACF (see sec. 3.2 and 3.3). The PSD spectra and the ACF of the LFS SOL, PFR and HFS SOL are shown in figure 5.8 and 5.9, respectively. As already mentioned in section 4.3, due to the 5-point filtering the Nyquist frequency is

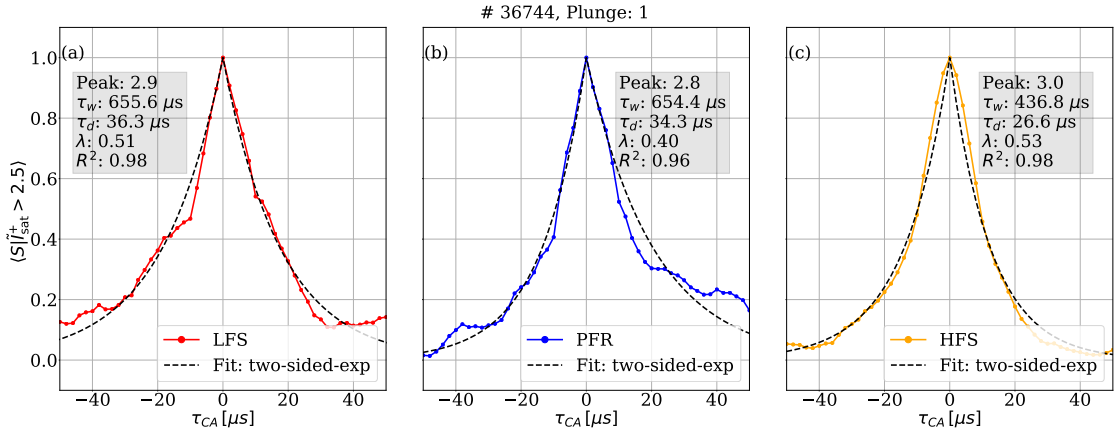

Figure 5.7: Wave-forms obtained from conditionally averaging the $\tilde{I}^+_{\text{sat}}$ signal for a threshold of 2.5. The black dashed line shows the double-exponential fit. The wave-forms are normalized to their peak value which is annotated in the figure

reduced from 250 kHz to 50 kHz. Below this frequency, the steep slope in the PSD spectra are effects of the filtering and these data are not taken into consideration. The spectra are fitted independently to obtained the pair of parameters $\lambda_{PSD}, \tau_{d,PSD}$ and only data points encircled in black are considered for the fit. In all the three regions, the PSD spectra and the ACF are well described by the individual PSD-fit. Interestingly, the LFS SOL and PFR fits tend to a one-sided exponential function, i.e., $\lambda_{PSD} = 0$ or $\lambda_{PSD} = 1$. For comparison with the parameter pair obtained from the CA wave-form the corresponding fits are shown on top of both the PSD spectra and the ACF by purple lines. It is clear for all cases that the parameter pairs of the CA and PSD/ACF are not in good mutual agreement. However, we note that the more intermittent signal on the HFS allows for better agreement between the CA wave-form and the PSD parameters pairs. This is an indication that the underlying assumptions of the FPP model is violated. In particular, if the signals are dominated by overlapping pulses. We will return to this issue at the end of the paragraph.

As mentioned in chapter 4, the tail of the ACF profile on the LFS cannot be described by the simple theoretical model 3.34. This also applies for the PFR.

At low frequencies, $\lambda = 1$ and $\lambda = 0$, the FPP model dictates that the PSD is expected to be described by a Lorentzian function falling with ω^{-2} at low frequencies (i.e., for frequencies where $\omega > 1/\tau_d$ refer to sec. 3.3 and [76]). In figure 5.10 the PSD of the static signals for each of the three regions are fitted at low frequency by a power-law $1/f^{\alpha}$ (refer to sec. 3.2.4). In the LFS SOL (fig. 5.10 (a)) it is observed that the slopes of the spectrum changes from $\alpha \approx 0.5$ (black dashed line) to $\alpha \approx 2.3$ (continuous black line). In the PFR and the HFS the slope of the PSD spectra are both approximately 1.5. In the PFR, even though an asymmetry parameter λ_{PSD} of zero is obtained from the PSD-fit, the spectrum does not fall with $\alpha \approx 2$ and similar for the spectra of the HFS SOL. On the LFS SOL, the

two fits intersect at $f \approx 12$ kHz. In the ideal case, the frequency at which the two slopes intersect is equivalent to the duration time of the pulse ($\omega = 1/\tau_d$, note the multiplying factor of 2π). On the LFS SOL, the estimated duration time is 12 μs, and the individual PSD fit gives a $\tau_{d,PSD}$ of 28 μs (refer to tab. 5.8 in next section). The values obtained for the PFR and HFS are in good agreement. The intersection frequency for the PFR and HFS SOL are at 8 kHz and 7 kHz and the estimated duration times for both regions are 20 μs and 23 μs, respectively (compare with black fit in fig. 5.8).

We now return to the discussion about the underlying assumption of the FPP model. A synthetic data study has been carried out alongside the data series obtained in the HFS SOL without applying a low-pass filter (see append. A.3). It is observed that even without the filtering the CA wave-forms are well described by the two-sided exponential fit (see fig. A.10). The synthetic one-sided exponential time series is able to describe the decaying slope of the CA wave-form, however a slower rising front is obtained (fig. A.10 (b)). This is caused by the pulse overlapping that occurs during the conditional averaging method. The wave-form of the synthetic data, generated by using the two-sided exponential function, is overestimating the duration time compared to the generating parameters (fig. A.10 (c)). Nevertheless, the fitted set of parameters (from the synthetic CA wave-form) maps much better to the PSD spectra (fig. A.11 (c)). The overestimation is also reflected in the ACF of the two-sided-exponential (fig. A.12 (c)). We see that on the moderately intermittent HFS, the two parameter pairs maps well between the CA wave-form and the PSD (and ACF), but ceases to do so for increasing γ. After reducing the noise by the 5-point filtering, the intermittency parameter γ of the HFS signal decreased from 5.9 to 4.4, which strengthen the applicability of the FPP model (see synthetic data study with low-γ in appendix. A.2). However, for the filtered signal we still observe a significant discrepancy between the CA wave-form parameters and the PSD-fit parameters as evident from the above analysis (see fig. 5.8 and 5.9).

In the next section, the static signals of the plunges of shot #36736 and #35466 are analysed in similar manner and the results are discussed. For completeness, the above analysis on the unfiltered data is presented in the appendix B.

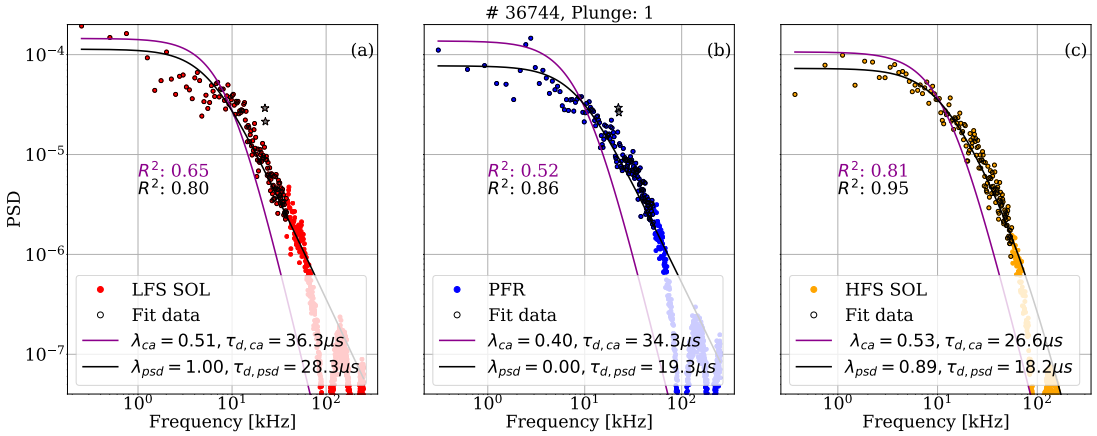

Figure 5.8: The power spectral density calculated for each of the filtered normalized static signals in the three different regions, the LFS SOL (a), PFR (b) and the HFS SOL (c). The points marked with stars in the LFS SOL and PFR are due to electrical interference and these have not taken into account while fitting the data. For the fit only data points encircles in black are considered.

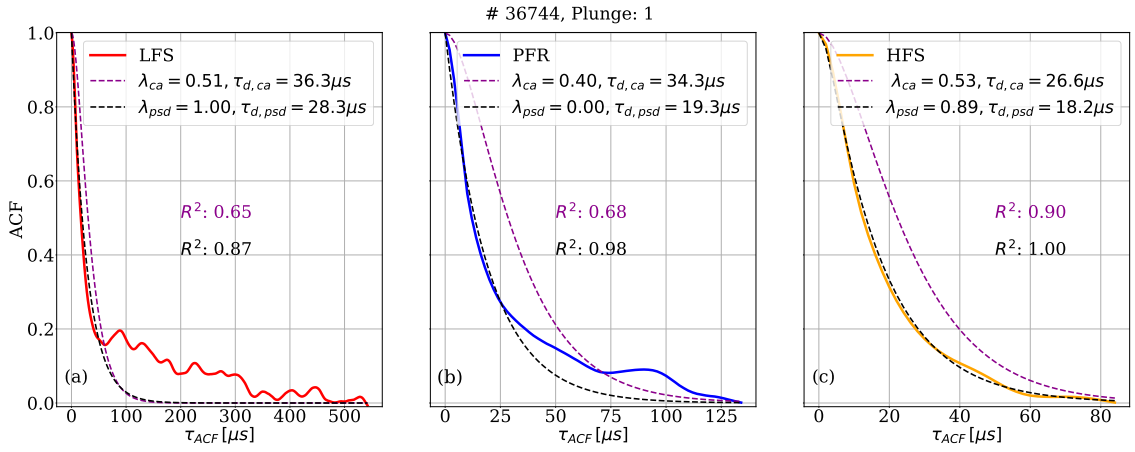

Figure 5.9: The autocorrelation function calculated for each normalized static-signals in the three different regions, the LFS SOL (a), PFR (b) and the HFS SOL (c).

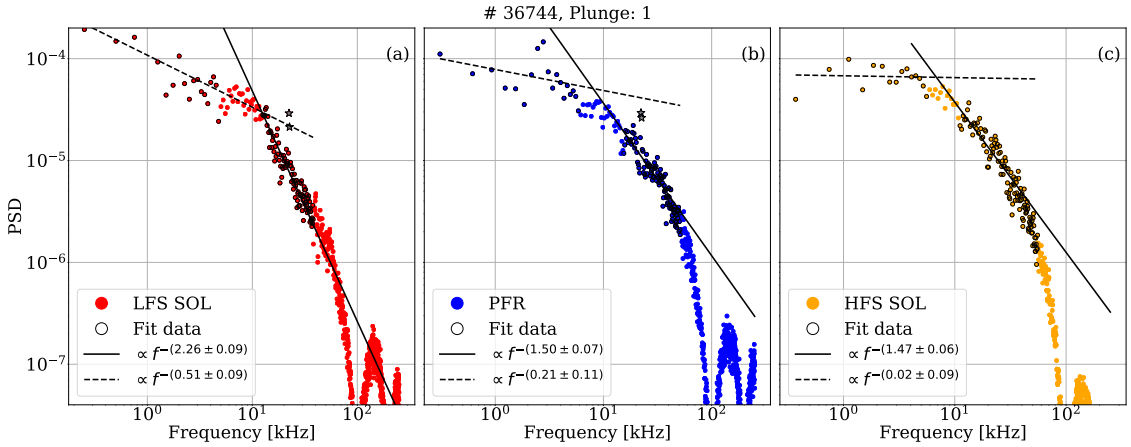

Figure 5.10: The power spectral density calculated for each normalized static-signals in the three different regions, the LFS SOL (a), PFR (b) and the HFS SOL (c). Electrical interference are noted by the stars and these data points have not been considered during the analysis. For the fit only data points encircles in black are taken into account.

5.4 Comparison between ECRH & NBI heated plasmas

In this section, the data analysis presented in the previous section is applied systematically to the data series obtained from several plunges during: a deuterium (D, #35466) and two helium (He, #36736 & #36744) shots. The L-mode shots are all medium density in a lower single null configuration with auxiliary heating of approximately 400 kW. The experimental details of the three shots are listed in table 2.2. Note that during the deuterium shot #35466 no stationary phases were planned. However, on reaching the maximum position (on the HFS SOL), the period of deceleration and acceleration of the probe is taken to be a 'probe-stationary-phase' as the major radius R_{m} does not vary significantly.

The statistical characteristics of the raw static signals (i.e., without any 5-point averaging or normalization) determined in the different regions of the tokamak are compared. In table 5.1, the statistical moments are listed for all the plunge time series together with their relative fluctuation $\hat{I}^{+}_{\mathrm{sat}}$ level (given by eq. (5.1)). The mean and standard deviation of the data on the HFS SOL is consistently larger than on the LFS SOL and PFR. Consequently, the relative fluctuation level is smaller on the HFS, approximately half of the LFS SOL and PFR. The higher statistical moments of the raw static signals are listed in table 5.2.

From the data analysis of the synthetic data series (chap. 4), it was found that an unfiltered signal from LFS SOL shows similar characteristics of that of a white noise signal. We therefore apply a simple low-pass filter to attenuate higher frequencies and to focus on the low frequencies characteristics of the signals. After the filtering, the static signals are normalized as given by equation (3.23).

In the following, we consider the filtered-normalized static signals unless otherwise specified. It is seen that for most of the plunges, the skewness and flatness of the LFS SOL and the PFR are close to a Gaussian-distribution ($S = 0$ and $F = 3.0$), whereas the data from the HFS SOL plunges are described by a Gamma distribution. The flatness as a function of the skewness is shown in figure 5.11 for all the plunges together with the parabolic relationship (see eq. (3.22)) between the two moments. The data from the LFS SOL deviates slightly from a Gaussian distribution while, on the HFS SOL the moments are scattered along the parabolic curve. The PFR, on the other hand, gives prominence to a Gaussian distribution as the moments are grouped around $F = 3$ and $S = 0$. For shot #36736 a voltage break-in was observed between 3.73 - 3.737 s (third plunge when the probe was in the PFR) giving rise to the large skewness and flatness. For the third plunge of shot #36744, it seems likely to be due to an Alfvén mode at around 200 kHz that appeared for a short time. This mode is discussed at the end of this section.

The intermittency parameter γ determined for the PDFs are listed in table 5.3. The signals obtained in the LFS SOL are in most cases described well by a Gaussian distribution (see fig. 5.6). In the PFR, the signal is perfectly normal distributed as reflected by the large intermittency parameter. As shown previously, a signal described by a normal distribution is constituted by a high degree of overlapping pulses. This violates the assumption of the FPP model and basically invalidates the applicability of the model for the signals in the LFS SOL and PFR. However, one can still consider the CA, PSD and ACF individually.

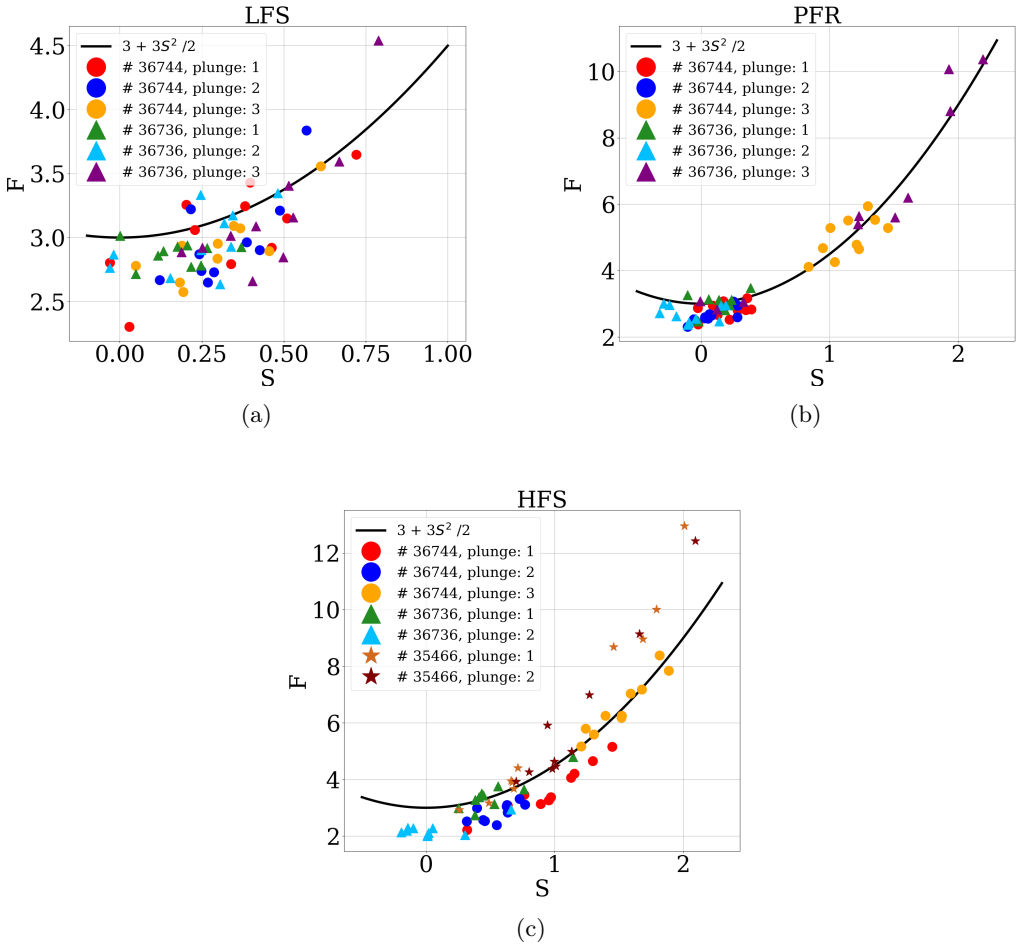

Figure 5.11: The flatness as a function of the skewness for the 5-point averaged and normalized static signals in the three regions: (a) the LFS SOL, (b) the HFS SOL and (c) the PFR.

Shot #	Plunge #	Mean $\langle I_{\mathrm{sat}}^{+} \rangle$			Stand. deviat.$\sigma_{I_{\mathrm{sat}}^{+}}$			Rel.Fluct. $\hat{I}_{\mathrm{sat}}^{+}$		
		LFS SOL	PFR	HFS SOL	LFS SOL	PFR	HFS SOL	LFS SOL	PFR	HFS SOL
36744	1	0.07	0.06	0.45	0.02	0.02	0.09	0.23	0.25	0.02
36744	2	0.06	0.07	0.56	0.01	0.02	0.07	0.18	0.23	0.13
36744	3	0.05	-	0.44	0.01	-	0.06	0.19	-	0.14
36736	1	0.08	0.07	0.47	0.01	0.01	0.04	0.15	0.20	0.09
36736	2	0.06	0.08	0.53	0.01	0.02	0.08	0.16	0.21	0.15
36736	3	0.04	-	saturation	0.01	-	saturation	0.20	-	saturation
35466	1	-	-	0.10	-	-	0.01	-	-	0.12
35466	2	-	-	0.10	-	-	0.02	-	-	0.17

Table 5.1: The mean and standard deviation of the full interval of the raw static signals and the relative fluctuation level. 'saturation' denotes that voltage break-in was observed.

Shot #	Plunge #	Skew. S			Flat. F		
		LFS SOL	PFR	HFS SOL	LFS SOL	PFR	HFS SOL
36744	1	0.3	0.2	1.0	3.0	2.8	3.7
36744	2	0.3	0.1	0.6	3.0	2.7	2.8
36744	3	0.3	-	1.5	2.9	-	6.6
36736	1	0.2	0.1	0.5	2.9	3.0	3.5
36736	2	0.2	-0.1	0.1	3.0	2.7	2.2
36736	3	0.5	-	saturation	3.2	-	saturation
35466	1	-	-	1.0	-	-	6.3
35466	2	-	-	1.2	-	-	6.1

Table 5.2: Skewness and flatness of the filtered-normalized static signals.

Shot #	Plunge #	Intermittency param. γ		
		LFS SOL	PFR	HFS SOL
36744	1	38.1	100	4.4
36744	2	37.8	100	13.0
36744	3	44.7	-	1.7
36736	1	100	100	14.3
36736	2	70.2	100	100
36736	3	18.9	-	saturation
35466	1	-	-	3.7
35466	2	-	-	3.0

Table 5.3: Intermittency parameter of the PDFs determined after 5-point averaging.

Filamentary studies in several fusion devices as well as in simulations (e.g. the ESEL code [100]) show that the LFS SOL at the outboard mid-plane is very intermittent and follows a Gamma distribution with tails covering many decades in probability [67, 72–74, 101–105]. The most directly related result to the current work, is the report from Tanaka *et al.* [105]. They report a statistical analysis of fluctuations close to the X-point region. In contrast to the current work where the ion-saturation current is obtained using the same probe, they use three different probes for each regions, i.e., SOL at outboard mid-plane, HFS SOL (lower than the mid-plane but above the X-point) and at the X-point on the LFS SOL [105]. They considered data from NBI heated plasmas, but unfortunately, the plasma ion type is not given, so a standard D plasma is assumed. Interestingly, they find that the HFS data follows a Gaussian distribution, while our measurements shows that the HFS SOL follows a Gamma distribution independent of the auxiliary heating and ion types presented. We discuss this results in more details later in section 5.5.

The number of conditional events and the amplitude of the wave-forms obtained for the plunges of the three shots are listed in table 5.4. The LFS and PFR wave-forms have a pulse amplitude around 2.9, while the pulse amplitudes on the HFS are mostly above 3.0, which

Shot #	Plunge #	Cond. Events			Amplitude		
		LFS	PFR	HFS	LFS	PFR	HFS
36744	1	59	47	60	2.9	2.8	3.0
36744	2	49	40	48	2.9	2.8	2.8
36744	3	54	-	127	2.9	-	3.4
36736	1	48	48	52	2.8	2.8	3.1
36736	2	47	24	-	2.9	2.8	-
36736	3	65	-	sat.	2.9	-	sat.
35466	1	-	-	39	-	-	3.4
35466	2	-	-	50	-	-	3.5

Table 5.4: Number of conditional events determined by the conditional averaging method for a threshold of 2.5 on the 5-point averaged signals. The corresponding peak amplitude of the wave-form determined are listed as well.

are in agreement with the ion-saturation current measurements. While the amplitude does not hold any absolute significance it can be seen that the HFS have larger amplitude relative to the LFS and PFR in agreement with the intermittency observed. The duration time $\tau_{d,CA}$ and asymmetry parameter λ_{CA} are listed in table 5.5. The goodness of the fit are listed in the last three columns of table 5.5 and shows that the double-exponential fit describes the wave-form quite well.

In all cases, measurements (e.g Langmuir probes and gas-puff-imaging) on the LFS SOL at the mid-plane of different tokamaks show that the CA wave-form is asymmetric with a fast rise and a slow decay [7, 67, 72–74, 101–105]. At the LFS mid-plane, this shape is independent of the averaged densities of plasma [67, 74]. In contrast to the mid-plane observations, the CA wave-forms in the X-point region show a symmetric profile as the estimated λ_{CA} of the three regions is approximately 0.5. Comparing the CA wave-forms to Tanaka *et al.* [105], it is evident that their wave-form is similar to the wave-forms obtained before filtering was performed (see fig. 4.5 (a) and 4.10). While, they claim this is the defining feature they seem to neglect to focus on the low-frequency part of the signal, where the energy seems to be located. Note that they have the same sampling rate as the current work which is 500 kHz.

Table 5.6 list the values of $\tau_{d,PSD}$ and λ_{PSD} obtained by fitting equation (3.33) to the PSD spectra of the signals. Compared to the CA wave-form, it is seen that even after filtering, the CA wave-form estimates a larger pulse duration time compared to the PSD-fit. The asymmetry parameter determined for the LFS SOL are in agreement. Both of the fitting routines point toward a symmetric wave-form in the LFS SOL. For the HFS SOL and PFR, the fit of the PSD spectra estimates a one-sided exponential. For the He plasmas, a slow rising and fast decaying tail is observed while for the D plasma a wave-form with a fast rising and slow decaying tail estimated.

The quality of the fits describing the PSD spectra using both pairs of parameters of CA

Shot #	Plunge #	Cond. Avg. $\tau_{d,CA}[\mu s]$			Cond. Avg. λ_{CA}			R^2		
		LFS	PFR	HFS	LFS	PFR	HFS	LFS	PFR	HFS
36744	1	36.3	34.3	26.6	0.51	0.40	0.53	0.98	0.96	0.98
36744	2	23.4	27.7	35.4	0.46	0.42	0.49	0.85	0.65	0.92
36744	3	24.5	-	16.1	0.55	-	0.49	0.84	-	0.99
36736	1	22.5	23.4	31.3	0.54	0.44	0.55	0.89	0.98	0.90
36736	2	23.5	25.2	-	0.53	0.55	-	0.95	0.93	-
36736	3	26.6	-	sat.	0.46	-	sat.	0.98	-	sat.
35466	1	-	-	22.7	-	-	0.43	-	-	0.98
35466	2	-	-	19.1	-	-	0.42	-	-	0.97

Table 5.5: Pulse duration time $\tau_{d,CA}$ and asymmetry parameter λ_{CA} determined from the CA wave-forms of the 5-point averaged and normalized signals. The last columns give quality of double-exponential fit.

Shot #	Plunge #	PSD $\tau_{d,PSD}[\mu s]$			PSD λ_{PSD}		
		LFS	PFR	HFS	LFS	PFR	HFS
36744	1	28.3	19.3	18.2	1.00	0.0	0.89
36744	2	13.1	14.6	23.2	0.50	0.0	0.99
36744	3	14.3	-	11.5	0.50	-	0.60
36736	1	12.3	12.0	24.4	0.50	0.07	1.0
36736	2	12.8	10.2	-	0.50	0.75	-
36736	3	14.8	-	sat.	0.50	-	sat.
35466	1	-	-	17.7	-	-	0.02
35466	2	-	-	15.5	-	-	0.0

Table 5.6: Pulse duration time $\tau_{d,PSD}$ and asymmetry parameter λ_{PSD} obtained by fitting equation (3.33) to the PSD spectra of the 5-point average and normalized signals.

wave-forms and the PSD-fits are given in table 5.7. It is evident that the estimated parameter pair obtained from the CA wave-forms maps very poorly to the pair obtained from the PSD-fit. However, we note that for the HFS SOL, where a large intermittent signal is present, the mapping do improve significantly.

In table 5.8 the slope parameter α obtained from the power-law fit performed for the three shots and the estimated duration time as calculated from the frequency at which the two fits intersect (see fig. 5.10) are listed. It is seen that the slopes of the LFS SOL and PFR varies between 2.0 and 3.0. The slope of the He shots have an average value of 1.5 on the HFS SOL, while the D shot have slopes of around 2.0. Tanaka *et al.* reports a slope of 1.5 for both the LFS SOL (mid-plane) and X-point, whereas a slope of 1.0 is observed on the HFS SOL [105]. In both our measurements and those reported by Tanaka *et al.*, it is seen that the HFS SOL shows a more moderate slope compared to the LFS SOL region. The duration time τ_d estimated from the intersection frequency is in good agreement with the values obtained by the fitting of the PSD spectra (see tab. 5.6).

We now analyze the unfiltered normalized PSD spectra for the three shots, where the mode of approximately 200 kHz is present. Figure 5.12 shows the unfiltered PSDs of the LFS SOL, the PRF and the HFS SOL. On the LFS SOL and PFR, two peaks are observed at 22.5 kHz for the NBI heated plasma and $\approx$ 24 kHz for the plasma heated using ECRH (see the zoomed-in of Fig. 5.12). The presence of these frequencies has been observed in spectrograms in the submitted paper [92] and are due to electronic interference as the frequencies are very specific and occurs during the whole experiments. This interference has also been observed in measurements from the bolometers in ASDEX Upgrade's divertor as shown in figure 5.14 (a). These low-frequency peaks are not visible in the PSD of the HFS SOL. It is likely that these low-frequency peaks are suppressed by the higher plasma density on the HFS SOL (see Fig. 5.4 (a) and recall that the ion-saturation current is proportional to the electron-density measured). On the LFS SOL, it is observed that the PSD spectra starts to bend at high frequencies, indicating the presence of noise in the signals. On the HFS a mode at $\approx$ 200 kHz is observed during three plunges of the He plasmas. The mode is more pronounced for the ECRH heated He plasma compared to the NBI heated plasma. This mode has also been observed in the reflectometry diagnostics at the mid-plane as shown in figure 5.13 (a) by the black arrow. Similar to the XPM measurements, these modes are only visible on the HFS (see the power spectrum of the reflectometry on the LFS Fig. 5.13 (b)). In the measurements from the Mirnov coils the frequency of approximately 200 kHz has been identified as a toroidicity-induced Alfvén eigenmode (TAE). It thus seems that the XPM measurements have captured the signature of the TAE on the HFS.

Shot #	Plunge #	R^2_{CA} PSD			R^2_{PSD} PSD			R^2_{CA} ACF			R^2_{PSD} ACF		
		LFS	PFR	HFS	LFS	PFR	HFS	LFS	PFR	HFS	LFS	PFR	HFS
36744	1	0.65	0.52	0.81	0.80	0.86	0.95	0.65	0.68	0.90	0.87	0.98	1.00
36744	2	0.51	0.39	0.66	0.81	0.80	0.84	0.91	0.36	0.75	0.99	0.91	0.98
36744	3	0.57	-	0.87	0.83	-	0.95	0.93	-	0.92	0.99	-	1.00
36736	1	0.44	0.49	0.65	0.77	0.92	0.84	0.89	0.79	0.67	0.98	0.99	0.92
36736	2	0.52	0.18	-	0.85	0.87	-	0.90	0.30	-	0.99	0.98	-
36736	3	0.59	-	sat.	0.91	-	sat.	0.94	0.58	sat.	1.0	0.75	sat.
35466	1	-	-	0.78	-	-	0.88	-	-	0.81	-	-	0.96
35466	2	-	-	0.84	-	-	0.94	-	-	0.86	-	-	0.97

Table 5.7: The quality of the fits obtained for the PSD and ACF using both the CA parameter pair and the PSD parameter pair.

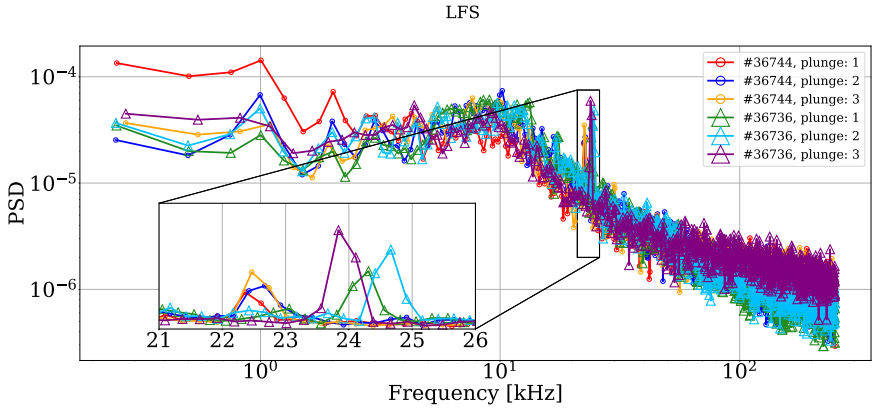

(a)

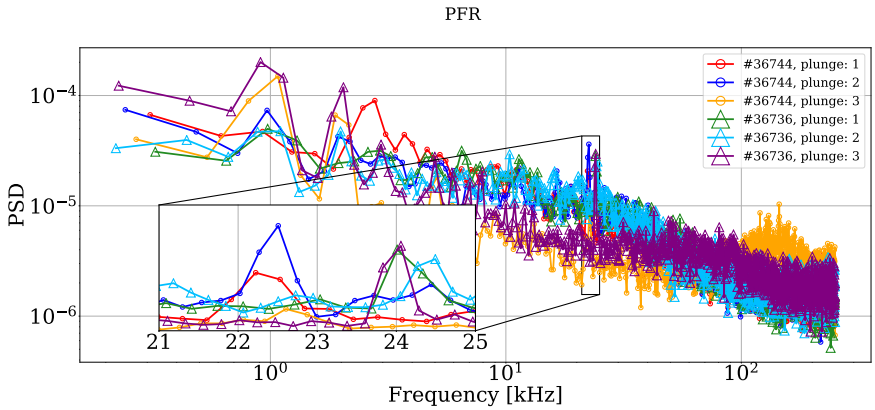

(b)

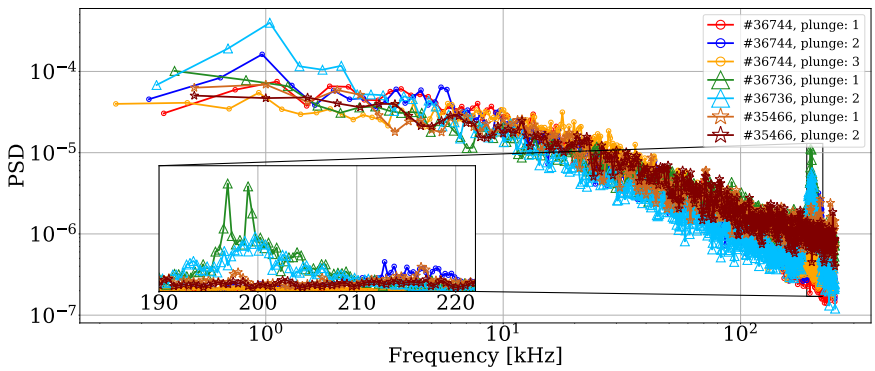

(c)

Figure 5.12: The power spectral density spectra in the frequency domain for the unfiltered normalized static signals in the three regions: (a) LFS, (b) PFR and (c) HFS.

Shot #	Plunge #	Power law α			τ_d estimate [μs]		
		LFS SOL	PFR	HFS SOL	LFS SOL	PFR	HFS SOL
36744	1	2.3±0.10	1.5±0.07	1.5±0.06	12	20	23
36744	2	2.2±0.10	2.0±0.03	1.5±0.05	12	27	27
36744	3	2.2±0.09	-	1.6±0.06	16	-	11
36736	1	3.0±0.15	2.9±0.14	1.3±0.06	9	6	14
36736	2	2.4±0.10	2.1±0.08	1.6±0.05	11	8	31
36736	3	2.0±0.07	-	saturation	16	-	saturation
35466	1	-	-	2.11±0.13	-	-	9
35466	2	-	-	1.94±0.14	-	-	9

Table 5.8: Power-law fit on the slope of the 5-point averaged PSD spectra (see solid black line in fig. 5.10) and the intersection frequency with the dashed line.

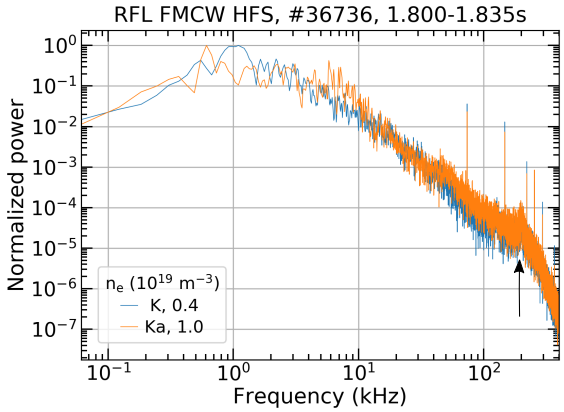

(a) HFS

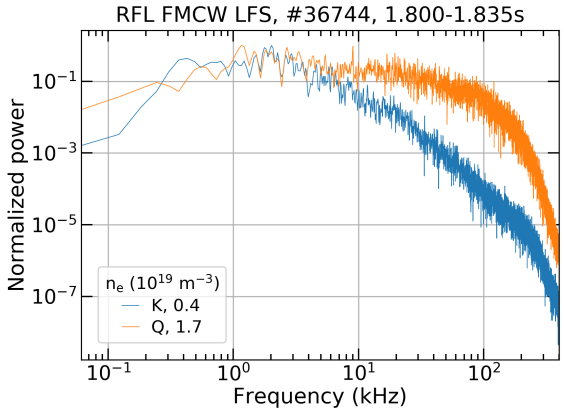

(b) LFS

Figure 5.13: (a) Power spectrum from the reflectometry on the HFS SOL at the mid-plane. Courtesy of Luis Gil.

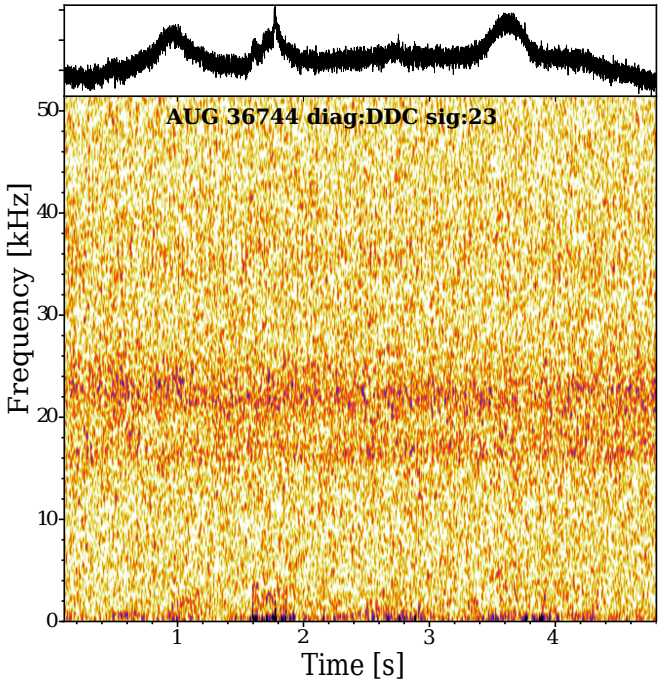

(a)

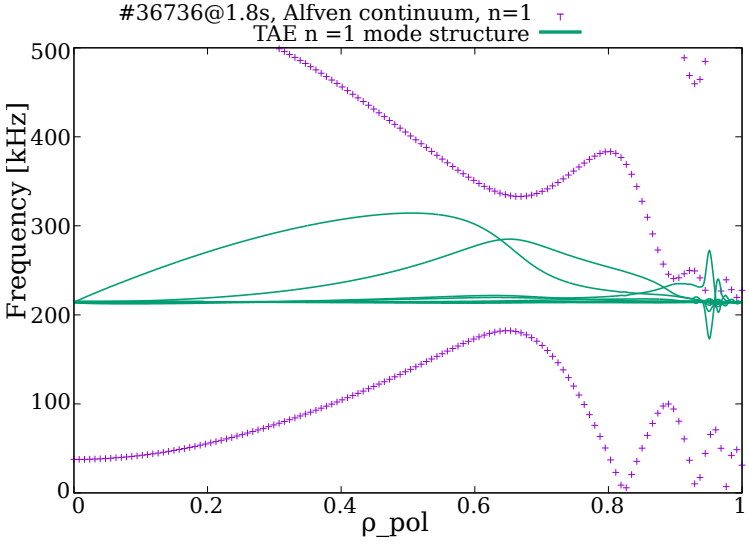

(b)

Figure 5.14: (a) Divertor bolometer data, courtesy of Pierre David (b) Toroidicity-induced Alfvén eigenmodes, courtesy of Philipp Lauber.

5.5 Discussion

The FPP model (see section 3.3) provides a framework for unifying the statistical properties of SOL fluctuations from one-point measurements. This method has been applied on data acquired at the mid-plane of several different tokamaks and its prediction has shown excellent agreement with experimental measurements. We have investigated whether the FPP model continues to hold for measurements taken just below the X-point.

We start by focusing on the differences between observations made at the LFS mid-plane and the X-point region. Therefore, using the FPP model we try to interpret the $\tilde{I}^{+}_{\mathrm{sat}}$ time series and investigate its agreement with the measurements collected just below the X-point. In the presented analysis, section 5.4, it was clear that the individual curve-fits for the CA wave-forms, the PSD spectra and the ACF are able to describe the measurements. However, the unifying property of the FPP model was not found, i.e., the parameter pairs did not map to each other.

The assumptions on which the FPP model is based assumes that the pulses are uncorrelated, Poisson distributed and that they all have the same shape and duration [78, 79]. A strong intermittency is assumed (i.e., a small γ) such that the pulse overlapping of individual pulses may be neglected [13]. Indeed, the synthetic data analysis presented in appendix A.3, shows that the FPP model performed better for small γ and non-overlapping pulses. We also observe this improvement for the HFS analysis, see tab. 5.7, especially after filtering. Still, the signals are not sufficiently intermittent.

The presented measurements shows a moderate intermittency only on the HFS SOL while Tanaka *et al.* [105] observed a Gaussian distributed PDF for the fluctuations in JT-60U, where they measured the ion-saturation current using Langmuir probes as well. A possible explanation for this difference could be that their HFS SOL measurements are acquired in between the inboard mid-plane and the X-point where the stabilizing effect of the 'good' curvature is in effect. The gradient of the pressure and the magnetic field strength are anti-parallel at the inboard mid-plane, stabilizing the interchange instabilities. The resulting $\mathbf{E}\times\mathbf{B}$ velocity arising due to charge separation is directed radially outwards relative to the major radius, which at the inboard mid-plane means 'going' back into the confined plasma. Thus, it is most likely that the fluctuations born at the outboard mid-plane and flowing towards the HFS SOL are pushed back into the confined plasma.

In contrast, the HFS probe measurements presented here are close to the separatrix leg. Here, Harrisson *et al.* reported a turbulent plasma in the HFS PFR [106, 107]. Experimental and 2D-simulation results from DIII-D identified an $\mathbf{E}\times\mathbf{B}$ convection cell around the X-point in L-mode plasmas [108, 109]. The latter reported a cross-$\mathbf{B}$ potential gradient that drives electrons and ions on equipotentials around the X-point at $\mathbf{E}\times\mathbf{B}$ drift velocity, which results in convection of particles, energy and momentum across the separatrix. The results presented in section 5.2 shows that a turbulent HFS PFR has been observed as well and is most likely due to interchange and drift-driven turbulence (see sec. 1.4), since the pressure gradient and the magnetic curvature gradient are in counter direction. Considering the $\mathbf{E}\times\mathbf{B}$ convection cell, it is likely that the fluctuations on the HFS PFR

are transported in the HFS SOL thus, making the HFS SOL (our measurements position) below the X-point turbulent. The $\mathbf{E}\times\mathbf{B}$ convection cell reported also extend above the X-point and it can be argued that HFS SOL above the X-point should be turbulent as well. However, considering the strong magnetic shearing due the X-point and the fact that the radial $\mathbf{E}\times\mathbf{B}$ drift is directed towards the confined plasma, it is likely that the fluctuations are sheared such that they are not visible by a probe, which explain Gaussian distribution of the HFS SOL in Tanaka *et al.* [105]. Our data set does not include the combination of a D plasma heated with NBI, therefore, we cannot rule out the possibility that the behaviour of the plasma could be different for a D plasma heated with NBI.

The intermittency parameter γ obtained on the HFS SOL below the X-point is still larger than what has been observed at the LFS mid-plane, showing that the pulse overlapping is not negligible. Since, the conditional averaging method does not account for overlapping pulses, one observes an increase of the wave-form's tail when applying the method. The conditional averaging method therefore predicts a broader wave-form compared to the PSD-fit. From the ACF profiles, we observe long correlation times (in particular for the LFS SOL) and we can therefore not assume that the pulses are uncorrelated or independent.

It is also observed that the wave-form obtained is symmetric compared to the asymmetric shape with a steep front and a trailing wake observed at the outboard mid-plane. At the outboard mid-plane the fluctuations are born in the edge region which is usually far away from the probe, therefore the arriving pulses can be modelled as uncorrelated pulses that satisfy a Poisson distribution. For the measurements around the X-point, the picture is different. Here, the shearing and instabilities can lead to the creation of fluctuations, which means that the probe is measuring at the local position where these filamentary structures are being 'born' rather than just 'seeing' them propagating as would be the case at the mid-plane. Therefore, the different behaviour of the FPP model compared to the LFS SOL mid-plane shows that the local fluctuations at the X-point cannot be modelled by a series of uncorrelated pulses under the assumption of a Poisson distribution. The analysis also indicates that the characteristics of the fluctuations created at the outboard mid-plane are not surviving and dominant in the divertor region, the reason for that is likely to be related to the strong magnetic shear and also the sheared motion at the divertor entrance. It is likely that local instabilities in the divertor region also contribute to the fluctuations measured and should be considered. N. Walkden has observed the presence of local instabilities in simulations carried out for the divertor region of MAST [110, 111].

Chapter 6

Conclusion

In this thesis, we have carried out a local fluctuation study of the plasma in the divertor region just below the X-point of the ASDEX Upgrade tokamak. Using Langmuir probes and the unique increased poloidal coverage of the X-point manipulator a continuous time series of the ion-saturation current was measured through the three different divertor regions: low-field side scrape-off layer, private flux region, and the high-field side scrape-off layer. The ion-saturation current is assumed to be an approximation for the density. We characterized the fluctuations in the X-point region by using similar fluctuation analysis tools on the ion-saturation current data as have previously successfully been applied at the outboard mid-plane. In this way, a comparison of the characteristics of the signals between different position in the tokamak was possible. The measurements collected by the Langmuir probes mounted on the X-point manipulator included probe-stationary phases, where data has been collected at fixed positions, one in each of the different regions. The analysis was divided into two parts. In the first part, the probe measurements was considered as a whole, i.e, the data collected during the entire insertion phase of the probe. In the second part, only the parts of the signal when the probe is in a stationary phases are considered.

The result of the first part showed the existence of a region with low fluctuation just outside of the low-field side separatrix leg. We therefore confirm the existence of this region, first identified by Walkden *et al.* [87], denoted the 'quiescent region' as successfully observed in ASDEX Upgrade as well. Spectral analysis revealed the presence of yet another region with low fluctuation levels located in the private flux region, which to the best of our knowledge has not been reported before. The existence of this region seems independent of both the types of plasma analyzed (helium and deuterium) as well as the auxiliary heating source.

In the second part we looked at the characteristics of the fluctuations by only considering the data collected during the probe-stationary phases and applied the filtered Poisson process (FPP) model. This model has been successful in describing time series obtained at the outboard mid-plane of several different tokamaks. In particular, it has been able to describe the power spectral density spectrum (PSD) and the autocorrelation function (ACF) satisfactorily from the duration time of the wave-form and its shape obtained by

conditional averaging (CA).

We evaluated the regime of validity of the FPP model by comparing the measurements to synthetic generated data series. We saw that this model is able to map the PSD and ACF from the CA wave-form for low γ only, i.e, a high degree of intermittency. Furthermore, it was clear that the unifying property of this model degrades quickly when the signal approaches a normal distributed.

We continued by applying the FPP model on the data from the X-point region, where we were able to obtain good fits of wave-forms and power spectral density spectra in all cases. However, the beauty of this model which lies in unifying all the observations (wave-form, probability density function, PSD / ACF) related to fluctuations did not work well for most of the data (with limited success on the HFS SOL).

For the individual fits, we observe that the CA wave-forms obtained in the X-point region are basically symmetric compared to the outboard mid-plane that has a universal wave-form with a steep rising front and trailing wake. Furthermore, the power spectral density showed that the filaments on the low-field side scrape-off layer has a symmetric shape. Those in the private flux region ($\lambda = 0$) and the high-field side scrape-off layer exhibit a one-sided exponential ($\lambda \approx 1$). Limited success was observed for the high-field side where the most skewed signal, approaching a Gamma distribution, was measured. This naturally enabled the underlying assumption of the filtered Poisson process model, i.e., a Gamma distribution which quantitatively showed better agreement between the two parameter pairs. Still, it is reasonable to look for better understanding of how to map the two descriptions in cases of low intermittent signals.

It is clear from the analysis that the same assumptions made at the outboard mid-plane cannot be made for the fluctuations in the X-point region. In particular, the fluctuations in the X-point region cannot be described by a train of uncorrelated and independent pulses that satisfy a Poisson distribution. One plausible explanation is that in the X-point region the fluctuations are born due to instabilities (at location of measurement), while at the outboard mid-plane the Langmuir probes measures fluctuations that are born in the edge of the plasma away from the diagnostics. The analysis also indicates that the characteristics of the fluctuations created at the outboard mid-plane are not surviving and dominant in the divertor region, the reason for that is likely to be related to the strong magnetic shear and also the sheared motion at the throat of the divertor region. However, local instabilities in the divertor region may also contribute to the fluctuations measured and should be taken into account. But it is clear that the X-point measurements have a significantly different characteristic from the usual mid-plane, which we just started to scratch the surface of.

Chapter 7

Challenges and Outlook

Here we discuss the challenges related to the data analysis and give an outlook where we discuss some future paths for improvement. The challenges related to the experimental planning have been discussed in chapter 2 (experimental setup).

7.1 Challenges related to X-point measurements

As mentioned already, one of the main obstacles in the data acquisition was the frequent observation of voltage break-in of the power supply. Unfortunately, many of the data collected had to be neglected. This is challenging when doing fluctuation analysis, as one cannot assume that the density fluctuations are dominant compared to the temperature fluctuations. Recall that we the ion-saturation current is proportional to the electron density. Also if the floating potential is much larger ($> 3T_e$) than the electron temperature, the ion-saturation current measurements could be used, however, due to the voltage break-in the I-V characteristics curve were not available to determine the plasma parameters. For the helium shots we were partly successful in tuning the plasma parameters in order to avoid having the voltage break-in. However, due to COVID-19 this has not been tested for a deuterium plasma and therefore we cannot conclude on the underlying cause (other than arcing) for the voltage break-in.

7.2 Outlook

In some sense, the era of fluctuation studies in the X-point region and the divertor region have just begun and therefore, the literature is quite limited. In this project we set out to redeem this situation by characterizing the fluctuations around the X-point region. The results presented show that the X-point fluctuations have widely different characteristic wave-forms compared to the universal steep rising slow decaying wake observed at the mid-plane. These findings suggest that the underlying assumptions of the filtered Poisson process model at the mid-plane are not well fulfilled by the fluctuations close to the X-

point. As indicated by the name, the filtered Poisson process model is based on the assumption that pulses are uncorrelated and Poisson distributed. However, it turns out that the fluctuations in the X-point region cannot be described by the a train of Poisson distributed pulses and the unifying feature of the model is simply not applicable.

This leaves lot to be done for future work. A whole series of experiments was lined up before COVID-19 pandemic lockdown, which unfortunately could not be carried out. Firstly, we would aim for repeating all measurements for the purpose of reproducibility. Repeating the measurements for deuterium plasmas with electron-resonance cyclotron heating and neutral beam injection as auxiliary heating sources as well as pure ohmic plasma to complete the data set. We may then investigate with greater certainty whether the helium and deuterium shots exhibits similar behaviour and the impact of the heating sources. It could be interesting to explore the effects due to the interaction of the probe itself. For example repeating the measurements where the probe is plunged up to the maximum position on the high-field side and perform the probe-stationary phases on the way out. We believe that the findings should be observed independent of how the plunge is made.

Furthermore, an increased sampling rate would improve the overall data quality. A higher sampling rate would allow for better resolved peaks in the signal. This might improve the wave-form determined by the conditional averaging.

Another important aspect is to improve the electronics setup. For example rearranging the power supply such that larger negative voltages can be tolerated might allow for overcoming the occurrences of the voltage break-ins.

Cross-correlating between the mid-plane and the X-point region is also of great interest. It is also possible that the fluctuations at the outboard mid-plane is not penetrating the divertor region, which might also be the reason for the poor mapping of the fluctuations characteristics using the FPP model. A comparison might provide the insight on whether the filaments still exist around the X-point or whether they are already sheared. The latter would explain the Gaussian distribution of the pulses observed in the low-field side scrape-off layer measurement presented. These experiments can be used to investigate if the fluctuations at the X-point are born locally and not dominated by those born at the mid-plane. Unfortunately, the outboard mid-plane manipulator was not operational during most of the experiments, presented in this thesis and a direct comparison is not available.

It would also be interesting to investigate, what the particular sources of the intermittent signal observed on the high-field side scrape-off layer are due to, whether it is the filaments born at the outboard mid-plane, Kelvin-Helmholtz instability or interchange turbulence [111]. The appearance of a second 'quiescent' region was not reported before and it was not expected at the planning stages of this work. Further experiments for demonstrating the existence and support the findings presented will be of great value. One such experiment is to perform stationary measurements on the high-field side private flux region while sweeping the plasma equilibrium in different directions thereby mapping out the extend of the 'quiescent' region in the poloidal plane. Taking into account the position of the second 'quiescent' region, one might speculate its importance in relation to the power

deposition on the plasma facing components as well as its determining role on the width of the scrape-off layer. Answering these questions will hopefully shed light and bring insight on one of the biggest challenges that the fusion community is facing.

Appendix A

Synthetic Time Series

In this chapter, we present the synthetic data analysis generated to mimic measurements from the scrape-off layer in section A.1 and A.3 as well as a pure synthetic signals to investigate the effects of a low intermittency parameter γ in section A.2.

A.1 Short time series

In this section, a synthetic data study is carried out for shorter time series. The parameters used to generate the synthetic data series are equivalent to the longer series considered in the main text, except for the number of arriving events K.

- $\gamma = 20.2$
- $\tau_{\mathrm{d}} : 12.0\,\mu\mathrm{s}$
- $\lambda = 0.6$
- $dt = 2\ \mu s$
- $K = 19500$

Here we consider less arriving events. We compare the synthetic data with the normalized low-field side scrape-off layer. Figure A.1 shows the time series generated with a one-sided exponential and a two-sided exponential function. Using a threshold of 2.5, the number of conditional events encountered are 42 and 26 for the one-sided and two-sided exponential, respectively. The CA wave-forms together with a double-exponential fit are shown in figure A.2. It is observed that the slope of the CA wave-forms (for the short synthetic time series) are less smooth compared to the wave-forms for a longer synthetic time series, which could explain the shape of the LFS SOL measurement. For the PSD and ACF (see fig. A.3 and A.4), we observe that even for less data points, the FPP methods are able to describe the spectra and the ACF profile individually. Even though a mapping of the parameters pairs (CA wave-form tp PSD spectra) is not observe, it can be deduced that the methods of this model is able to describe shorter time series, when considered individually.

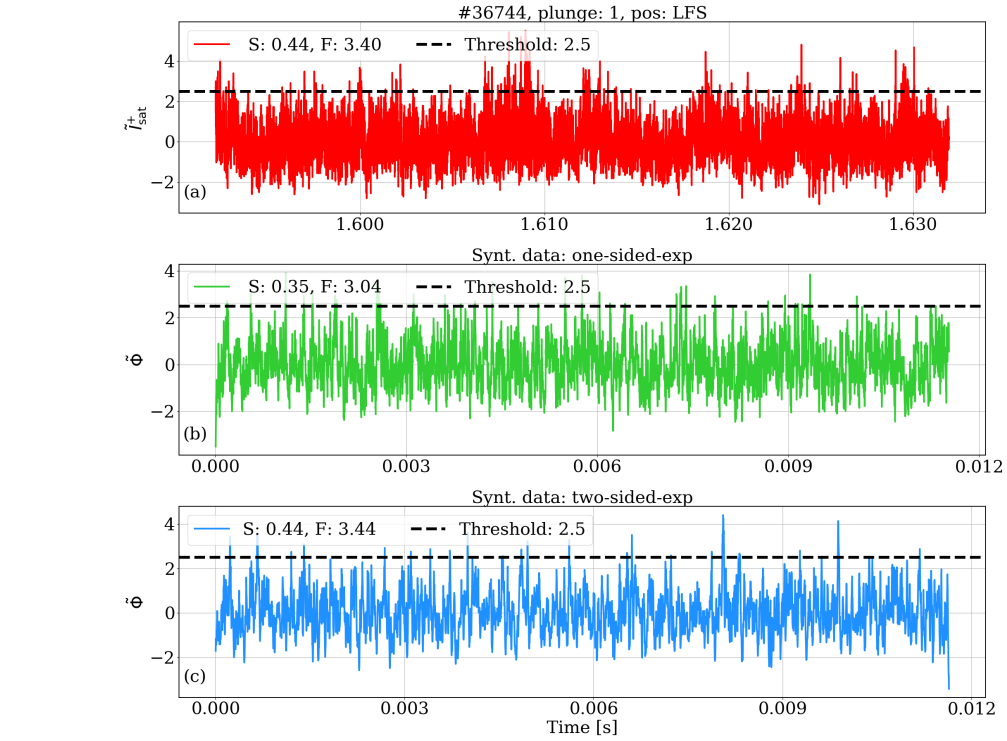

Figure A.1: Short synthetic signals. (a) The measured signal of the first plunge on the LFS of shot #36744. (b) Synthetic data generated using a one-sided exponential function and (c) synthetic data generated using a two-sided exponential.

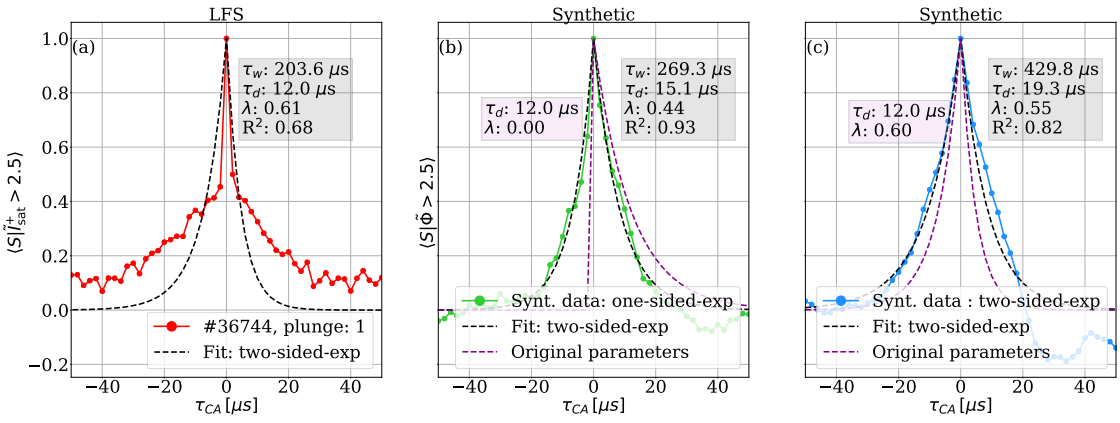

Figure A.2: Conditionally averaged wave-forms of (a) the measured signal and for the two synthetic time series generated with (b) the one-sided exponential function and (c) the two-sided exponential. The wave-forms are normalized to their peak value.

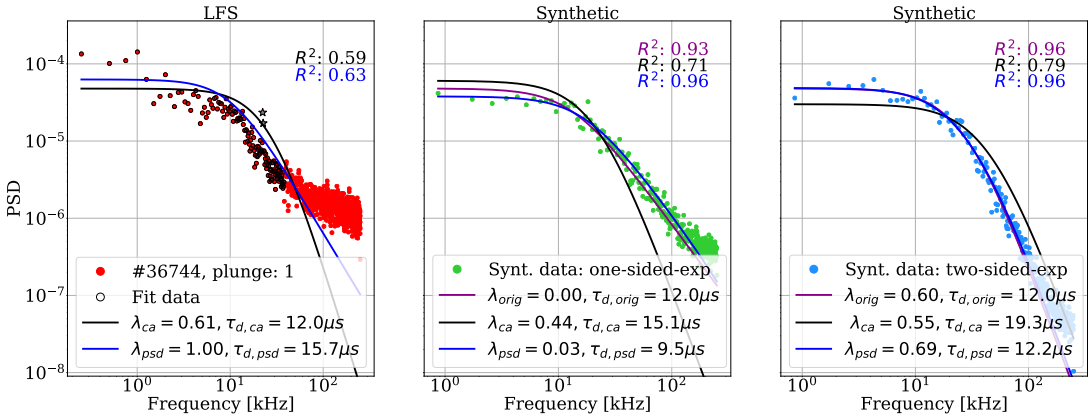

Figure A.3: Power spectral density of (a) the measured signal, (b) the one-sided exponential function and (c) the two-sided exponential.

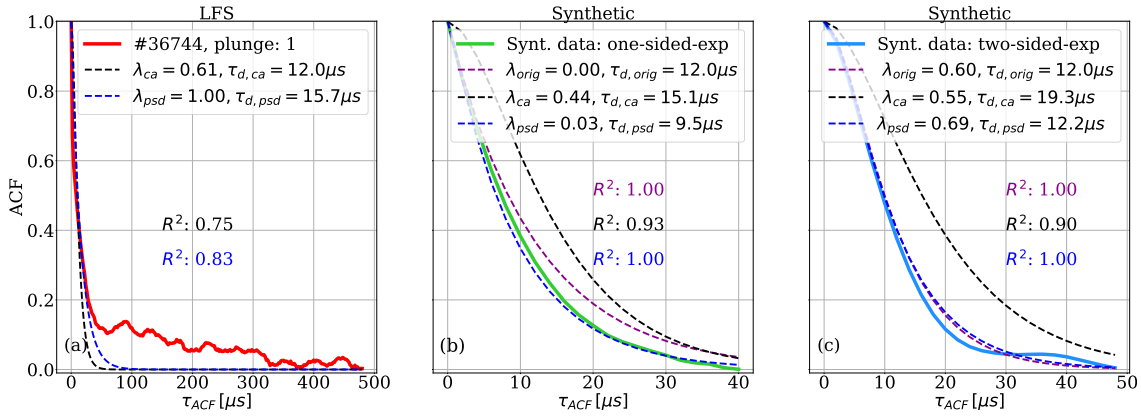

Figure A.4: Autocorrelation function of (a) the measured signal and for the short synthetic signal with (b) the one-sided exponential function and (c) the two-sided exponential.

A.2 Synthetic time series with small γ

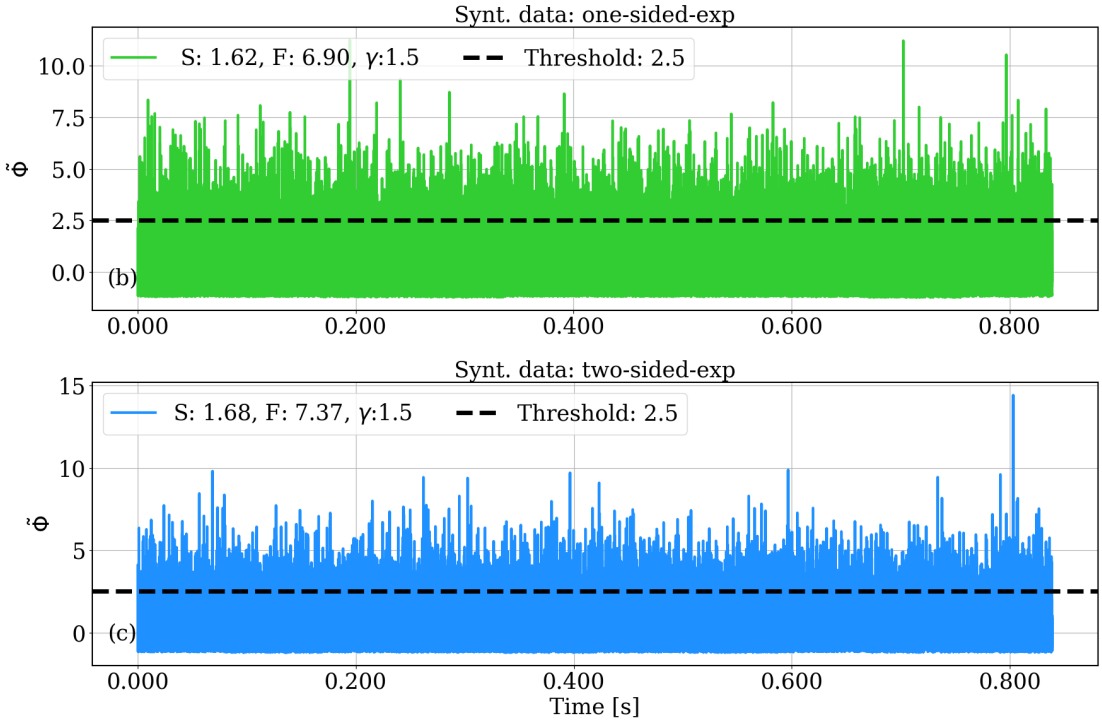

Figure A.5: (a) Synthetic data series generated for a one-sided exponential function and (b) synthetic data for a two-sided exponential.

The synthetic data study is carried out to investigate the effect of the intermittency parameter γ. Except for the intermittent parameter, which is chosen to be $\gamma = 1.5$, the other parameters used to generate the data are kept the same as those used in section 4.2:

- τ_{d} : 12.0 μs,
- $\lambda = 0.6$,
- $dt = 2\ \mu s$,
- $K = 105000$.

Figure A.5 shows that the length of the synthetic time series is much longer compared to the time series presented in section 4.2. This is because K and γ determine the length of the synthetic signal. The number of conditional events encountered are 5218 and 4290 for the one-sided and two-sided exponential, respectively. The CA wave-forms together with the double-exponential fit are shown in figure A.6. In both cases, the fitting routine is able to reconstruct the generating parameters from the CA wave-forms. Comparing the double-exponential wave-form to the others, in this case an almost perfect agreement is observed between the generating parameters and the fitted ones, whereas a deviation

was observed in the other synthetic data generated (sec. 4.2, A.1 and A.3). Also the parameters determined from CA wave-forms are in good agreement with the PSD-fit and this is shown in figure A.7. In both cases, it is observed that duration time is in agreement with the original value used to generate the synthetic data. In the one-sided exponential case (fig. A.7 (a)), the asymmetry parameter determined from the CA waveform is slightly larger than zero. Nevertheless, the slope of the PSD spectra is well described and the differences in the asymmetry parameter is seen mostly on the high frequency range.

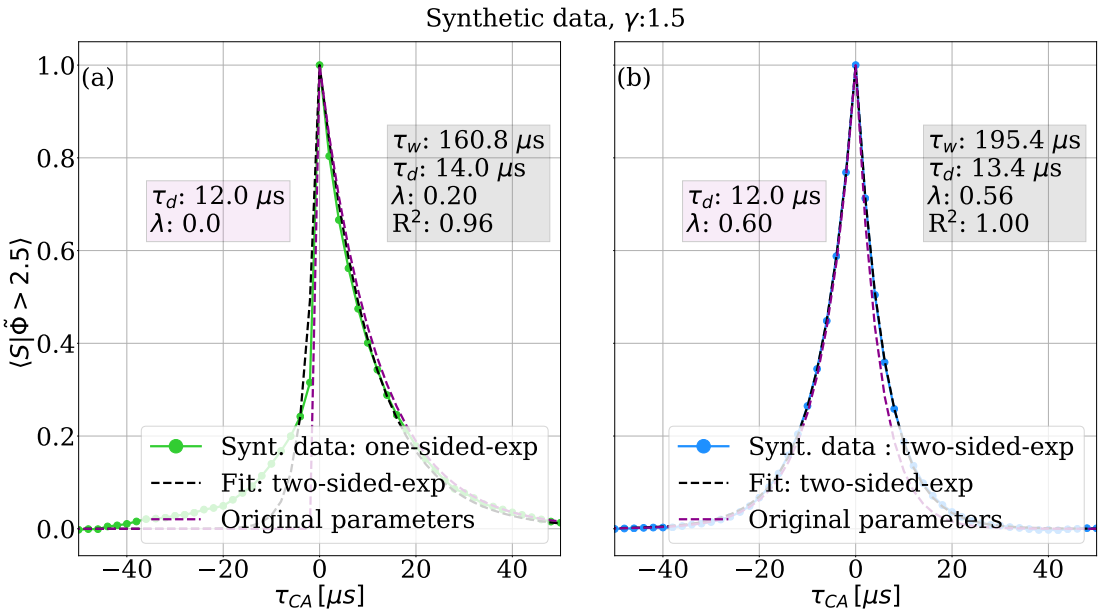

Figure A.6: Conditionally averaged wave-form of (a) the measured signal and for the two short synthetic time series generated with (b) the one-sided exponential function and (c) the two-sided exponential. The wave-forms are normalized to their peak value.

Since the PSD spectra and the ACF are Fourier pairs, the parameters describing the PSD spectra should be able to describe the ACF curve as well. This agreement is shown in figure A.8. The study with a low intermittency parameter γ shows that the FPP model maps the conditional averaged wave-form parameter pair with the PSD and ACF satisfyingly and such a good mapping has also been observed for experimental data at the outboard mid-plane where the measurements are highly intermittent.

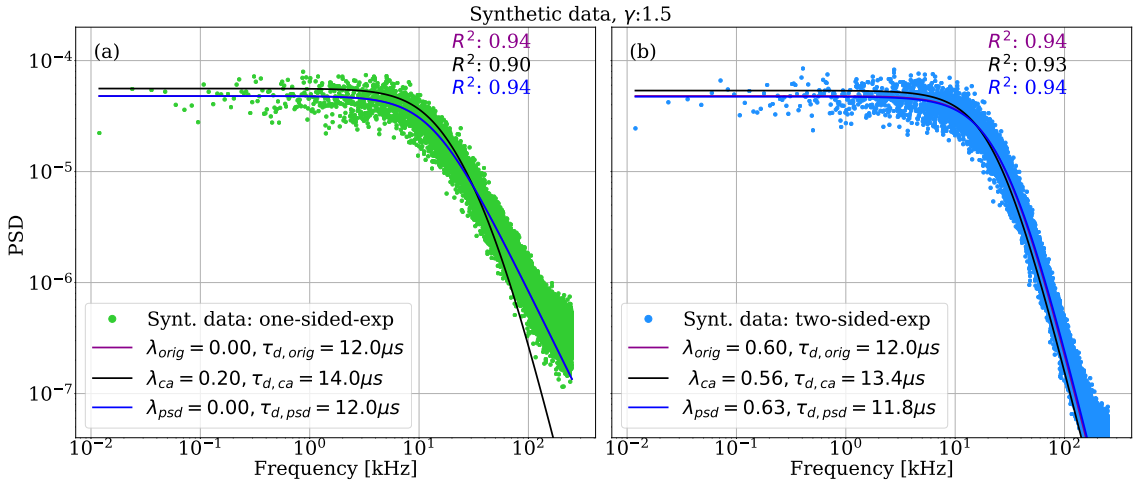

Figure A.7: Power spectral density of (a) the measured signal (b) the one-sided exponential function and (c) the two-sided exponential. Synthetic data for a short time series

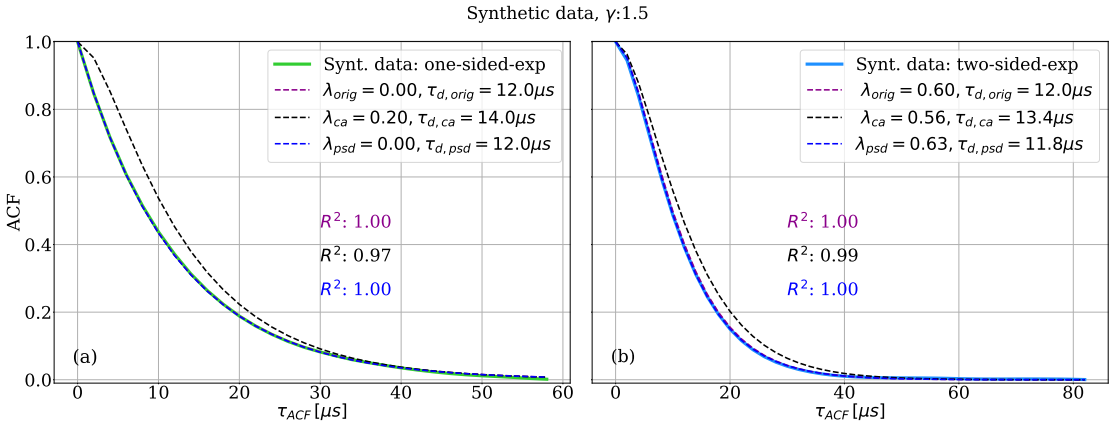

Figure A.8: Autocorrelation function of (a) the measured signal for the short synthetic signal with (b) the one-sided exponential function and (c) the two-sided exponential.

A.3 HFS synthetic data

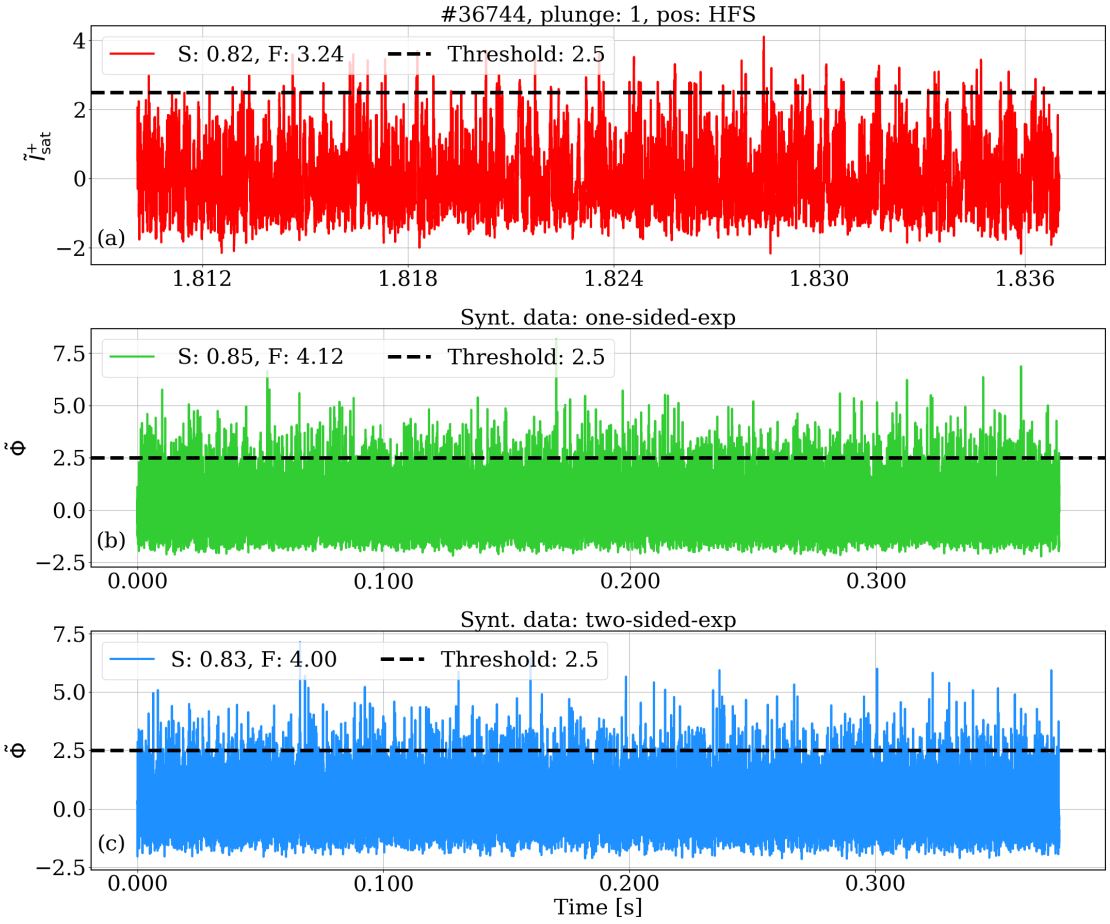

Figure A.9: (a) Measured signal of the first plunge on the HFS of shot #36744. (b) Synthetic data generated for a one-sided exponential function and (c) Synthetic data for a two-sided exponential. The black dashed line shows the threshold used for the conditional averaging method.

The synthetic data study is carried out to investigate the behaviour of the HFS measurement of the first plunge of shot #36744. The synthetic data are generated, using parameters that have been determined from the measured signal, as described in section 4.2.

- $\gamma = 5.9$
- τ_d : 21.0 μs
- $\lambda = 0.56$

- $dt = 2\ \mu s$
- $K = 105000$

Figure A.9 shows the measured signal and the two synthetic signals generated with a one-sided -and two-sided-exponential function, respectively. Figure A.10 shows the CA wave-form obtained for a threshold value of 2.5 and the number of conditional events are 99, 1374 and 775 for the real measurement, the one-sided exponential synthetic data and the two-sided one, respectively. Since the signal has a higher degree of intermittency ($\gamma = 5.9$), the synthetic data generated shows a good agreement as already discussed in appendix A.2, i.e., the parameters fitted from the wave-form and the PSD-spectra are in good agreement with each other and both set of parameters are able to describe the ACF curve as well. However, it is interesting to observe that the measurement itself does not show the same agreement. That is, for the measured signal the parameters obtained from the CA wave-form do not describe the PSD-spectra similar to what is observed on the LFS. The synthetic data shows that the signal is intermittent enough for the FPP model to work as anticipated, i.e., a mapping of the CA wave-form parameters to the PSD spectra. The overestimated duration time of the wave-form is however, reflected more in the ACF compared to the PSD spectra. The inconsistency between the synthetic data and HFS measurement is discussed in the result chapter (chapter. 5).

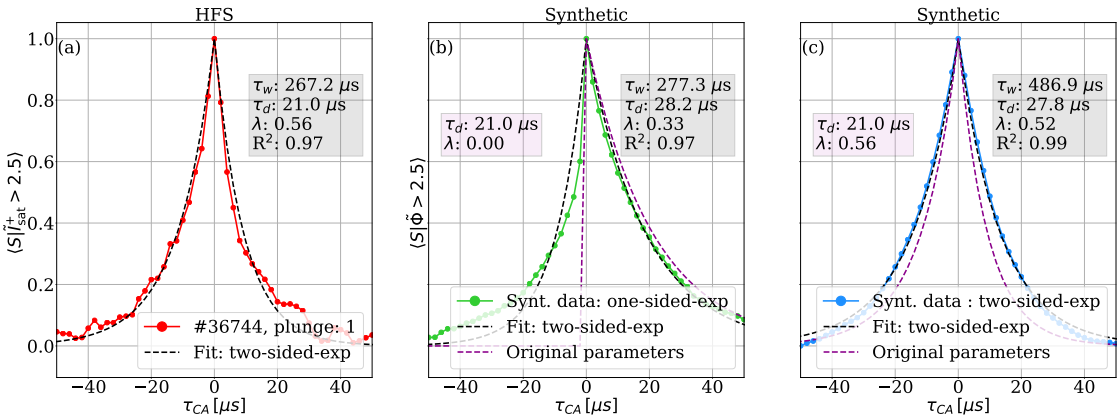

Figure A.10: Conditionally averaged wave-form of (a) the measured signal and for the two synthetic time series generated with (b) the one-sided exponential function and (c) the two-sided exponential. The wave-forms are normalized to their peak value.

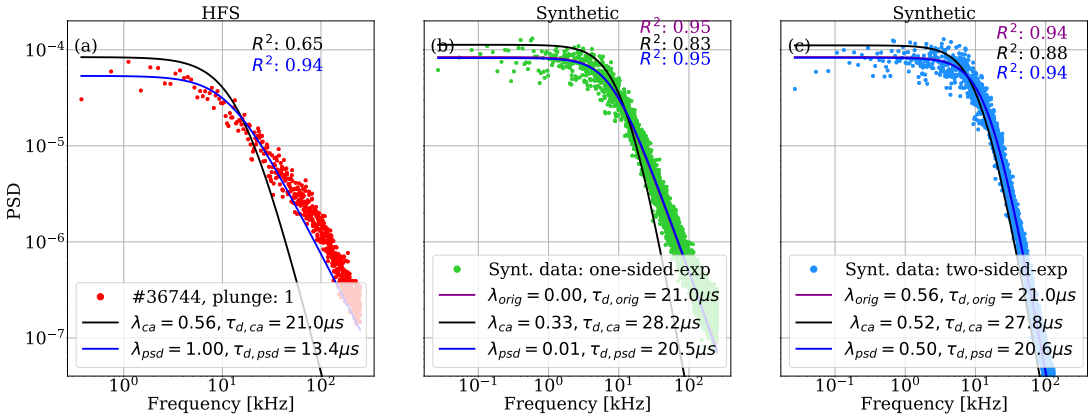

Figure A.11: Power spectral density of (a) the measured signal on the HFS (b) the one-sided exponential function and (c) the two-sided exponential. Synthetic data for a short time series

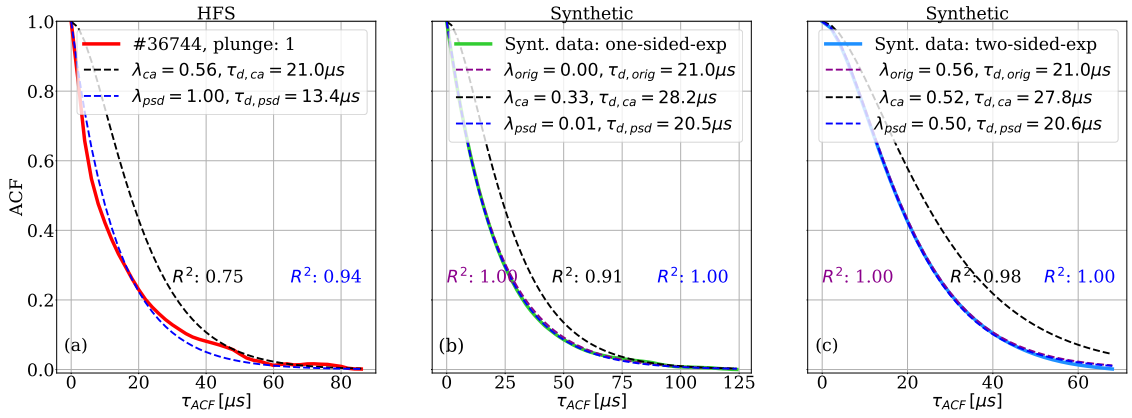

Figure A.12: Autocorrelation function of (a) the measured signal and the synthetic signal with (b) the one-sided exponential function and (c) the two-sided exponential.

Appendix B

Data Analysis Without Filtering

In this chapter the results of the analysis of the unfiltered signals are presented. The analysis has been carried out the same way as presented in the chapter 5. Figure B.1 (a) shows an example of the I_{sat}^{+} measured by the biased Langmuir pin 1 during the first plunge of shot #36744. The data points are shown in black and the XPM position is shown in green. The planned probe-stationary phases are represented by the plateaus in the XPM trajectory. The probe-stationary phases in each of the three regions are coloured. The normalized $\tilde{I}_{\mathrm{sat}}^{+}$ static signals are shown in figure B.1 (b), (c) and (d). The same colour coding is used as in figure B.1 (a) Figure B.2 shows part of the ACF determined for the normalized time series in figure B.1. The black dashed line represent the time-lag τ where the ACF reaches zero for the first time. The time interval of the time series in the LFS SOL, PFR and HFS SOL are approximately 39 ms, 32 ms and 26 ms, respectively. Comparing the time-lag to the length of the measurements, it can be deduced that normalizing the signals rendered them statistically stationary.

Figure B.3 shows the PDF of the first plunge of shot #36744 in the three different regions. Comparing the PDFs of the LFS- and HFS-SOL, a positive tail is observe in both cases indicating the existence of propagating filamentary structures. The intermittency parameters, however, indicates that the HFS SOL has the strongest intermittent turbulence during this plunge. The γ parameter of the PFR is the largest, thus showing the Gaussian distribution.

To get the averaged wave-form that would best described the bursts, the conditionally averaged method is applied to determine wave-form for a threshold vale of 2.5. For this threshold, the conditional events found on the LFS SOL, PFR and HFS SOL are 190, 89 and 99, respectively. Figure B.4 shows the conditionally averaged wave-forms of the three regions and the black dotted line represents the fit of a double-exponential function (see eq. 3.29). The fitting parameters, τ_d and λ, are given in the grey box as well as the waiting time in between pulse τ_w and the goodness of the fit. With an R^2 of 0.98, it is observed that wave-form on the HFS is best described by the double-exponential fit.

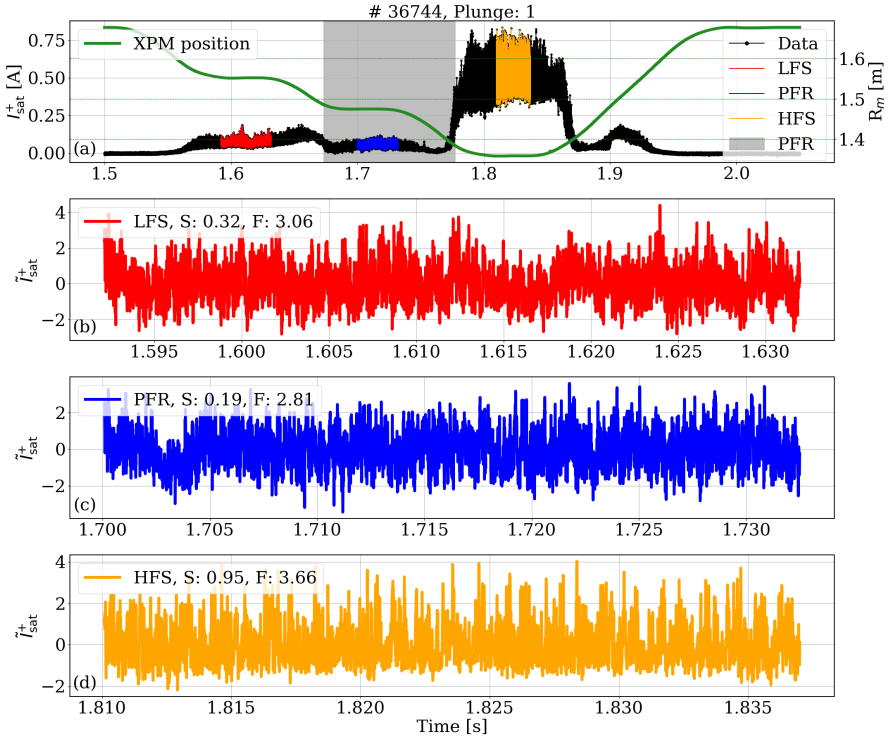

Figure B.1: Example of an I^+_{sat} measured by the biased Langmuir pin and the three normalized static-signals ($\tilde{I}^+_{\mathrm{sat}}$) measured in the LFS SOL, PFR and the HFS SOL. The skewness S, and the flatness F, of the each static-signal is given.

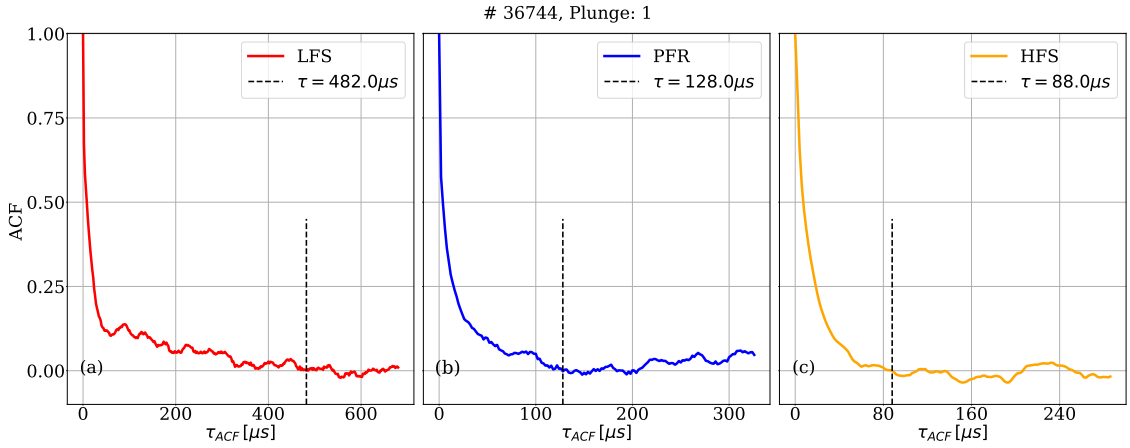

Figure B.2: The autocorrelation function calculated for each normalized static-signals in the three different region, i.e the LFS SOL, PFR and the HFS-SOL. The dashed line gives the lag time at which the ACF reached zero for the first time.

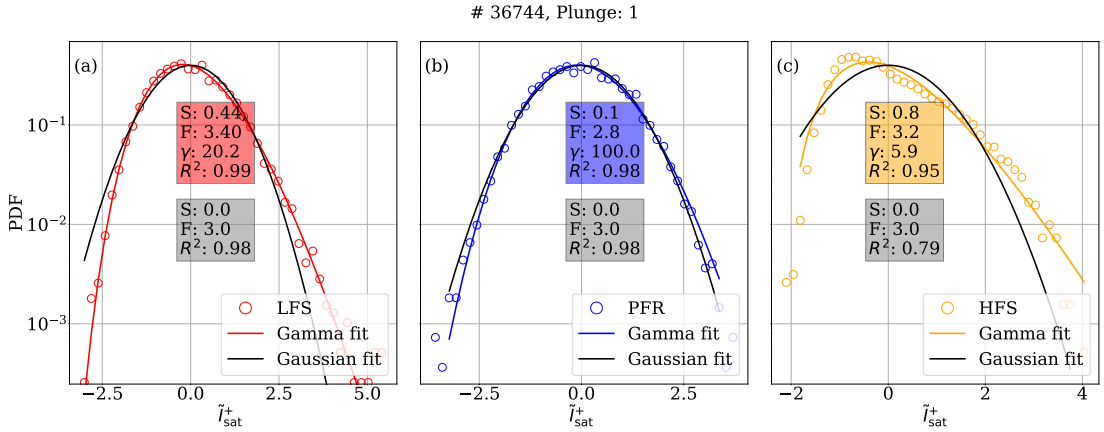

Figure B.3: The probability density function calculated for each normalized static-signals in the three different regions, i.e the LFS SOL (a), PFR (b) and the HFS SOL (c).

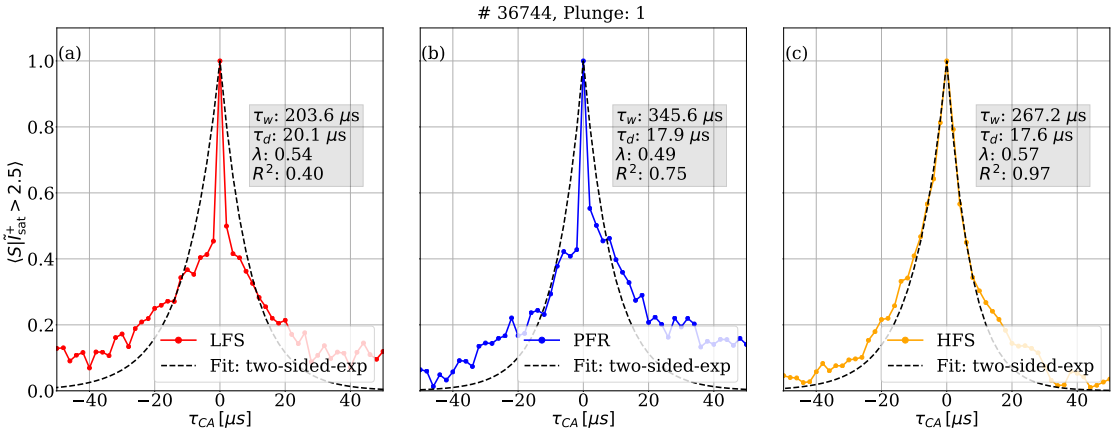

Figure B.4: Wave-forms obtained from conditionally averaging the $\tilde{I}^{+}_{\mathrm{sat}}$ signal for a threshold of 2.5. The black dashed line shows the double-exponential fit. Wave-form of LFS SOL (a), PFR (b) and HFS SOL (c).

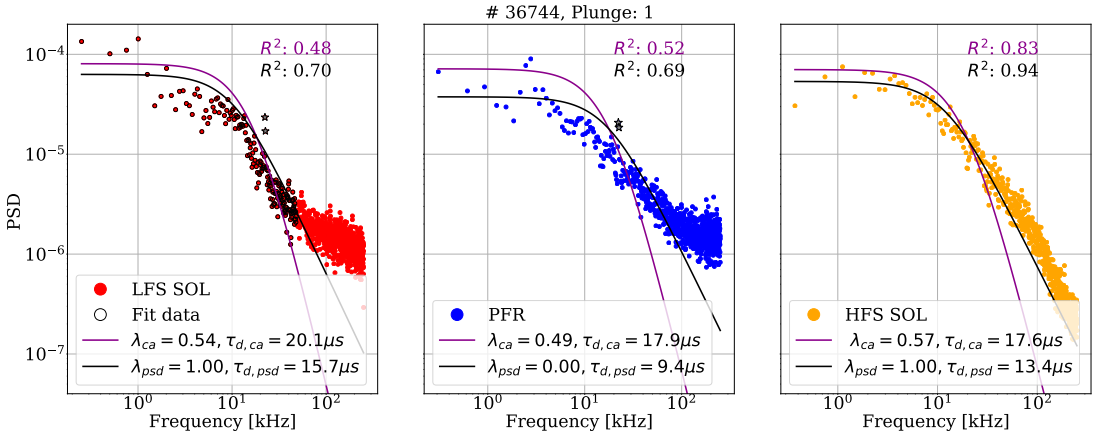

Figure B.5: The power spectral density calculated for each normalized static-signals in the three different regions, i.e., (a) the LFS SOL, (b) PFR and (c) the HFS SOL. The grey stars are due to electrical interference and was not taken into account during the curve fitting.

To further characterize the fluctuations of the signals we consider the PSD spectrum and its dual description in term of the ACF (see sec. 3.2 and 3.3). The PSD spectra and the ACF of the LFS SOL, PFR and HFS SOL are shown in figure B.5 and B.6, respectively. The PSD spectra are fitted using equation 3.33 and is shown as a black line. The quality of the fit, shows that the methods of the FPP model is able to describe only the measurement of the HFS SOL reasonably. Since the ACF and the PSD are a Fourier pair, as expected, the PSD-fit parameters are in good agreement with the ACF calculated. To compare with the fitting parameter pair obtained by the conditional averaged wave-form, the purple line is plotted on top of the PSD spectra as well as in the ACF (fig. B.6. The discrepancy between the two parameter pairs are reflected in all cases.

The PSDs of the LFS SOL, PFR and HFS SOL are shown in figure B.7 (a), (b) and (c), respectively. The data used to fit the slopes are encircled in black. It is observed that the slopes in the different regions follow the power-law behaviour and are in the range of $1 \leq \alpha \leq 2$. In the LFS SOL (fig. B.7 (a)) it is observed the that the slopes of the spectrum changes values from $\alpha \approx 0.5$ (black dashed line) to $\alpha \approx 1.8$ (continuous black line). The two fits intersect at $f \approx 12$ kHz for the LFS SOL while in the PFR and the HFS SOL, the slopes are relative flat for frequencies less than 4 kHz and 8 kHz, respectively. The estimated duration time from the intersecting frequencies are 13 μs, 40 μs, and 20 μs for the LFS SOL, the PFR and the HFS SOL, respectively.

It is observed that without applying a low-pass filter to the measurements (LFS SOL and PFR), the FPP model does not seem to be able to describe the data. The results of the filtered data are discussed in chapter 5.

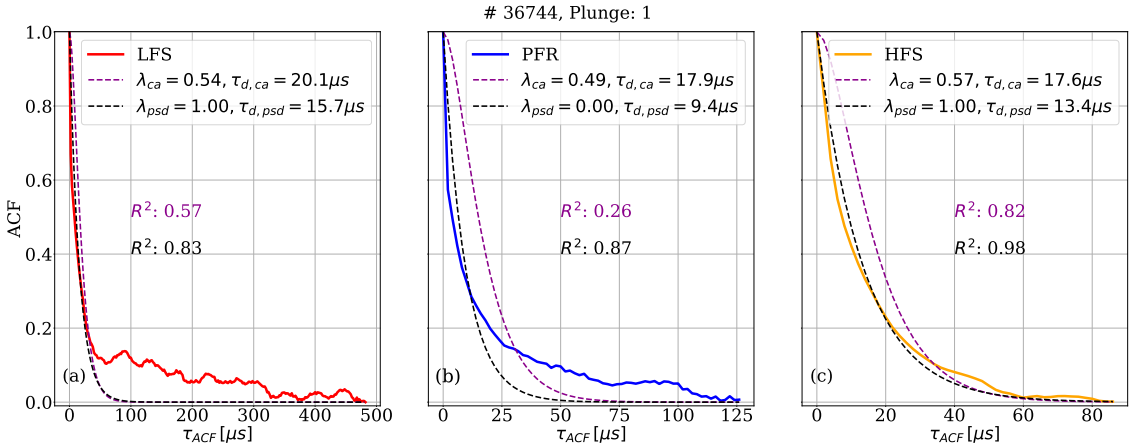

Figure B.6: The autocorrelation function calculated for each normalized static-signals in the three different regions, i.e., (a) the LFS SOL, (b) PFR and the (c) HFS SOL.

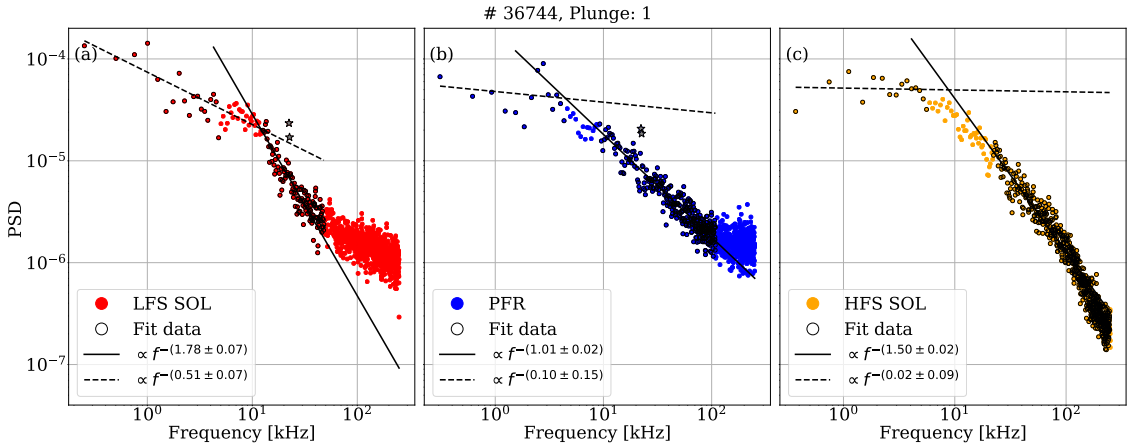

Figure B.7: The power spectral density calculated for each normalized static-signals in the three different regions, i.e., (a) the LFS SOL, (b) PFR and (c) the HFS SOL. The grey stars were not considered while performing the curve-fit as these data points are due to electrical interference.

Bibliography

[1] *Key world energy statistics*, International energy agency, 2019.

[2] R. K. Pachauri and L. A. Meyer, *(eds.)-core writing team of intergovernmental panel on climate change, climate change 2014: synthesis report. contribution of working groups i, ii and iii to the fifth assessment report of the intergovernmental panel on climate change*, IPCC, Geneva, Switzerland, 2014.

[3] R. D. Nem, *Surface temperature measurement of in-vessel components on ASDEX upgrade using infrared spectroscopy*, MSc. Thesis `https://pure.mpg.de/rest/items/item_2506539/component/file_2506540/content`, 2017.

[4] J. P. Freidberg, *Plasma physics and fusion energy, cambridge university press* (2007).

[5] *Iter*, `https://www.iter.org/proj/inafewlines`, 2020.

[6] C. M. Braams and P. E. Stott, *Nuclear fusion, half a century of magnetic confinement fusion research* (2002).

[7] D. A. D'Ippolito, J. R. Myra, and S. J. Zweben, "Convective transport by intermittent blob−filaments: comparison of theory and experiment", Physics of Plasmas **18**, 060501 (2011).

[8] J. Wesson, *Tokamaks, fourth edition* (2011).

[9] J. R. Myra, D. A. Russell, and D. A. DÌppolito, "Collisionality and magnetic geometry effects on tokamak edge turbulent transport. i. a two−region model with application to blobs", Physics of Plasmas **13**, 112502 (2006).

[10] C. Theiler, I. Furno, P. Ricci, A. Fasoli, B. Labit, S. H. Müller, and G. Plyushchev, "Cross-field motion of plasma blobs in an open magnetic field line configuration", Phys. Rev. Lett. **103**, 065001 (2009).

[11] P. Manz, D. Carralero, G. Birkenmeier, H. W. Müller, S. H. Müller, G. Fuchert, B. D. Scott, and U. Stroth, "Filament velocity scaling laws for warm ions", Physics of Plasmas **20**, 102307 (2013).

[12] G. Fuchert, G. Birkenmeier, D. Carralero, T. Lunt, P. Manz, H. W. Müller, B. Nold, M. Ramisch, V. Rohde, and U. Stroth, "Blob properties in L- and H-mode from gas−puff imaging in ASDEX upgrade", Plasma Physics and Controlled Fusion **56**, 125001 (2014).

[13] O. E. Garcia, "Stochastic modeling of intermittent scrape−off layer plasma fluctuations", Phys. Rev. Lett. **108**, 265001 (2012).

[14] From: `https://ristevski.weebly.com/nuclear-fusion.html`.

[15] S. Potzel, *Experimental classification of divertor detachment* (PhD Thesis, University of Bayreuth, Germany, Bayreuth, 2012).

[16] S. i. r. s. Health Physics Society, *Tritium*, `https://hps.org/documents/tritium_fact_sheet.pdf`, 2020.

[17] R. A. Cairns, "Tokamaks 3rd edition by john wesson, oxford university press 2004, 749pp, hardback 0 19 850922", Journal of Plasma Physics **71**, 377–377 (2005).

[18] H. Bosch, *Basic nuclear fusion, lecture script* (IPP summer university, Munich Germany, 2014).

[19] `https://www.euro-fusion.org/fusion/history-of-fusion/`.

[20] L. Spitzer, "The stellarator concept", The Physics of Fluids **1**, 253–264 (1958).

[21] ITER, `https://www.iter.org/mach`.

[22] B. Sieglin, *Divertor power load studies in all metal ASDEX upgrade and JET* (PhD Thesis, Max-Planck Institute for Plasma Physics, Boltzmanstraße 2, Garching München, 2014).

[23] C. García−Rosales, "Erosion processes in plasma−wall interactions", Journal of Nuclear Materials **211**, 202–214 (1994).

[24]R. Neu, K. Asmussen, K. Krieger, A. Thoma, H.-S. Bosch, and et al., "The tungsten divertor experiment at ASDEX upgrade", Plasma Physics and Controlled Fusion **38**, A165–A179 (1996).

[25]R. Neu, *Tungsten as a plasma facing material in fusion devices*, Habilitation Thesis, Max-Planck-Institut for Plasma Physics, Garching, Germany, 2003.

[26]F. Wagner, G. Fussmann, T. Grave, M. Keilhacker, M. Kornherr, and et al., "Development of an edge transport barrier at the h−mode transition of ASDEX", Phys. Rev. Lett. **53**, 1453–1456 (1984).

[27]K. H. Burrell, "Effects of E×B velocity shear and magnetic shear on turbulence and transport in magnetic confinement devices", Physics of Plasmas **4**, 1499–1518 (1997).

[28]K. Itoh and S.-I. Itoh, "The role of the electric field in confinement", Plasma Physics and Controlled Fusion **38**, 1–49 (1996).

[29]P. H. Diamond, V. B. Lebedev, D. E. Newman, B. A. Carreras, T. S. Hahm, W. M. Tang, G. Rewoldt, and K. Avinash, "Dynamics of transition to enhanced confinement in reversed magnetic shear discharges", Phys. Rev. Lett. **78**, 1472–1475 (1997).

[30]K. H. Burrell, "Role of sheared e × b flow in self-organized, improved confinement states in magnetized plasmas", Physics of Plasmas **27**, 060501 (2020).

[31]K. Petrovay, "Turbulence in the solar photosphere", arXiv, astro-ph/0005409 (2000).

[32]H. Tennekes and J. L. Lumley, *A first course in turbulence, the MIT press* (1972).

[33]J. Gottweiss, *A smoky candle*, `https://galileospendulum.org/2012/12/05/a-smoky-candle-science-advent-4/`, 2012.

[34]N. Brooks Martner, `https://www.researchgate.net/figure/The-Kelvin-Helmholtz-instability-is-visible-by-clouds-Source-Brooks-Martner-NOAA-ETL_fig9_279953803`.

[35]U. Stroth, *Plasmaphysik: phaenomene, grundlagen und anwendungen, 2. auflage* (2018).

[36]C. Brandt, *Active control of drift wave turbulence*, PhD Thesis, university of Greifswald, 2009.

[37]H. Park, D. L. Brower, W. A. Peebles, N. C. Luhmann, R. L. Savage, and C. X. Yu, "Development and application of multichannel collective scattering systems", Review of Scientific Instruments **56**, 1055–1056 (1985).

[38]J. Vicente, G. D. Conway, M. E. Manso, H. W. Müller, C. Silva, F. da Silva, L. Guimarãis, and A. Silva, "H−mode filament studies with reflectometry in ASDEX upgrade", Plasma Physics and Controlled Fusion **56**, 125019 (2014).

[39]B. Geiger, R. Dux, R. M. McDermott, S. Potzel, M. Reich, F. Ryter, M. Weiland, D. Wünderlich, and M. Garcia−Munoz, "Multi−view fast−ion d−alpha spectroscopy diagnostic at ASDEX upgrade", Review of Scientific Instruments **84**, 113502 (2013).

[40]I. Teliban, *Spatio−temporal diagnostics of plasma fluctuations with probe arrays and statistical techniques* (PhD Thesis, Christian-Albrechts-University, Germany, Kiel, 2006).

[41]F. F. Chen, *Langmuir probe diagnostics*, `http://www.seas.ucla.edu/~ffchen/Publs/Chen210R.pdf`, 2003.

[42]I. H. Hutchinson, *Principles of plasma diagnostics, 2nd edition, cambridge university press* (2005).

[43]B. S. Schneider, C. Ionita, S. Costea, O. Vasilovici, J. Kovačič, T. Gyergyek, B. Končar, M. Draksler, R. D. Nem, V. Naulin, J. J. Rasmussen, M. Spolaore, N. Vianello, R. Stärz, A. Herrmann, and R. Schrittwieser, "New diagnostic tools for transport measurements in the scrape−off layer (SOL) of medium−size tokamaks", Plasma Physics and Controlled Fusion **61**, 054004 (2019).

[44]K.-S. Chung, "Mach probes", Plasma Sources Science and Technology **21**, 063001 (2012).

[45]I. H. Hutchinson, "Oblique ion collection in the drift approximation: how magnetized mach probes really work", Physics of Plasmas **15**, 123503 (2008).

[46]S. H. Mueller, G. D. Conway, G. Birkenmeier, D. Carralero, T. Happel, A. Herrmann, P. Manz, P. de Marné, A. Mlynek, H. W. Mueller, S. Potzel, V. Rohde, U. Stroth, M. Tsalas, G. R. Tynan, and E. Wolfrum, "Direct observations of L−I−H and H−I−L transitions with the x−point reciprocating probe in ASDEX upgrade", Physics of Plasmas **21**, 042301 (2014).

[47]IPP, `http://www.ipp.mpg.de/16208/einfuehrung`.

[48]R. Neu, A. Kallenbach, M. Balden, V. Bobkov, and et al., "Overview on plasma operation with a full tungsten wall in ASDEX upgrade", Journal of Nuclear Materials **438**, Proceedings of the 20th International Conference on Plasma-Surface Interactions in Controlled Fusion Devices, S34–S41 (2013).

[49]IPP, `http://www.ipp.mpg.de/16340/stand`.

[50] https://www.aug.ipp.mpg.de/aug/local/aug_only/AUG_Aufbau/Picture_Gallery/ipage00022.htm, 2007.

[51] B. Streibl, P. T. Lang, F. Leuterer, J.-M. Noterdaeme, and A. Stäbler, "Chapter 2: machine design, fueling, and heating in ASDEX upgrade", Fusion Science and Technology **44**, 578–592 (2003).

[52] V. Bobkov, *Plasma waves and wave heating*, IPP summer university for plasma physics script, 2014.

[53] M. Tsalas, N. Tsois, V. Rohde, and J. Neuhauser, "Langmuir probe measurements in the lower x−point vicinity of the ASDEX upgrade divertor", Journal of Nuclear Materials **337-339**, PSI-16, 751–755 (2005).

[54] H. Meyer and et al., "Overview of physics studies on ASDEX upgrade", Nuclear Fusion **59**, 112014 (2019).

[55] P. J. McCarthy, P. Martin, and W. S. Schneider, "The cliste interpretive equilibrium code", (1999).

[56] M. Tsalas, D. Coster, C. Fuchs, A. Herrmann, A. Kallenbach, H. Mueller, J. Neuhauser, V. Rohde, and N. Tsois, "In–out divertor flow asymmetries during elms in ASDEX upgrade h−mode plasmas", Journal of Nuclear Materials **363-365**, Plasma-Surface Interactions-17, 1093–1098 (2007).

[57] D. S. Sivia, *With J. Skilling, data analysis, a bayesian tutorial, 2nd edition, oxford university press* (2006).

[58] D. University, *Statistics - notes 12: the jeffreys' prior*, https://www2.stat.duke.edu/courses/Fall11/sta114/jeffreys.pdf, 2011.

[59] V. Krishnan, *Probability and random processes, A J. Wiley & Sons, inc publication* (2006).

[60] A. Maurizi, "On the dependence of third− and fourth−order moments on stability in the turbulent boundary layer", Nonlinear Processes in Geophysics **13**, 119–123 (2006).

[61] P. Sura and P. D. Sardeshmukh, "A global view of non−gaussian SST variability", Journal of Physical Oceanography **38**, 639–647 (2008).

[62] K. R. Sreenivasan and R. A. Antonia, "The phenomenology of small−scale turbulence", Annual Review of Fluid Mechanics **29**, 435–472 (1997).

[63] C. Chatfield, *The analysis of time series, an introduction, fifth edition, Chapman & Hall CRC* (1995).

[64] R. Johansson, *Numerical python, scientific computing and data science applications with numpy, scipy and matplotlib, second edition, apress* (2019).

[65] P. Welch, "The use of fast fourier transform for the estimation of power spectra: a method based on time averaging over short, modified periodograms", IEEE Transactions on Audio and Electroacoustics **15**, 70–73 (1967).

[66] TU Berlin,https : / / www . itp . tu - berlin . de / fileadmin / a3233 / grk / pototskyLectures2012 / pototsky _ lectures_part1.pdf.

[67] O. Garcia, J. Horacek, R. Pitts, A. Nielsen, W. Fundamenski, V. Naulin, and J. J. Rasmussen, "Fluctuations and transport in the TCV scrape-off layer", Nuclear Fusion **47**, 667–676 (2007).

[68] F. Militello, P. Tamain, W. Fundamenski, A. Kirk, V. Naulin, and A. H. N. and, "Experimental and numerical characterization of the turbulence in the scrape-off layer of MAST", Plasma Physics and Controlled Fusion **55**, 025005 (2013).

[69] N. R. Walkden, A. Wynn, F. Militello, B. Lipschultz, G. Matthews, C. Guillemaut, J. Harrison, and D. M. and, "Interpretation of scrape-off layer profile evolution and first-wall ion flux statistics on JET using a stochastic framework based on filamentary motion", Plasma Physics and Controlled Fusion **59**, 085009 (2017).

[70] N. Walkden, A. Wynn, F. Militello, B. Lipschultz, G. Matthews, C. Guillemaut, J. Harrison, and D. M. and, "Statistical analysis of the ion flux to the JET outer wall", Nuclear Fusion **57**, 036016 (2017).

[71] O. E. Garcia, S. M. Fritzner, R. Kube, I. Cziegler, B. LaBombard, and J. L. Terry, "Intermittent fluctuations in the Alcator C-Mod scrape-off layer", Physics of Plasmas **20**, 055901 (2013).

[72] A. Theodorsen, O. E. Garcia, J. Horacek, R. Kube, and R. A. Pitts, "Scrape-off layer turbulence in TCV: evidence in support of stochastic modelling", Plasma Physics and Controlled Fusion **58**, 044006 (2016).

[73] R. Kube, A. Theodorsen, O. E. Garcia, B. LaBombard, and J. L. Terry, "Fluctuation statistics in the scrape-off layer of alcator c−mod", Plasma Physics and Controlled Fusion **58**, 054001 (2016).

[74] A. Theodorsen, O. Garcia, R. Kube, B. LaBombard, and J. Terry, "Relationship between frequency power spectra and intermittent, large-amplitude bursts in the Alcator C-Mod scrape-off layer", Nuclear Fusion **57**, 114004 (2017).

[75] O. Garcia, R. Kube, A. Theodorsen, J.-G. Bak, S.-H. Hong, H.-S. Kim, the KSTAR Project Team, and R. Pitts, "SOL width and intermittent fluctuations in KSTAR", Nuclear Materials and Energy **12**, Proceedings of the 22nd International Conference on Plasma Surface Interactions 2016, 22nd PSI, 36–43 (2017).

[76]A. Theodorsen, *Statistical properties of intermittent fluctuations in the boundary of fusion plasma*, Dissertation for a PhD, The Arctic university of Norway, 2018.

[77]A. Theodorsen and O. E. Garcia, "Probability distribution functions for intermittent scrape-off layer plasma fluctuations", Plasma Physics and Controlled Fusion **60**, 034006 (2018).

[78]O. E. Garcia, R. Kube, A. Theodorsen, and H. L. Pécseli, "Stochastic modelling of intermittent fluctuations in the scrape-off layer: correlations, distributions, level crossings, and moment estimation", Physics of Plasmas **23**, 052308 (2016).

[79]O. E. Garcia and A. Theodorsen, "Auto-correlation function and frequency spectrum due to a super-position of uncorrelated exponential pulses", Physics of Plasmas **24**, 032309 (2017).

[80]H. Johnsen, H. L. Pécseli, and J. Trulsen, "Conditional eddies in plasma turbulence", The Physics of Fluids **30**, 2239–2254 (1987).

[81]T. Huld, A. H. Nielsen, H. L. Pécseli, and J. J. Rasmussen, "Plasma vortices and their relation to cross-field diffusion: a laboratory study", Phys. Rev. Lett. **64**, 3023–3026 (1990).

[82]T. Huld, A. H. Nielsen, H. L. Pécseli, and J. Juul Rasmussen, "Coherent structures in two-dimensional plasma turbulence", Physics of Fluids B: Plasma Physics **3**, 1609–1625 (1991).

[83]R. V. Edwards and A. S. Jensen, "Particle−sampling statistics in laser anemometers: sample−and−hold systems and saturable systems", Journal of Fluid Mechanics **133**, 397–411 (1983).

[84]A. H. Nielsen, H. L. Pécseli, and J. J. Rasmussen, "Turbulent transport in low-beta plasmas", Phys.Plasmas **3**, 1530–1544 (1996).

[85]D. Block, I. Teliban, F. Greiner, and A. Piel, "Prospects and limitations of conditional averaging", Physica Scripta Volume T **122**, 25–33 (2006).

[86]R. Fischer, A. Bock, M. Dunne, J. Fuchs, L. Giannone, K. Lackner, P. McCarthy, E. Poli, R. Preuss, M. Rampp, and et al., "Coupling of the flux diffusion equation with the equilibrium reconstruction at asdex upgrade", Fusion science and Technology **69**, 526–536 (2016).

[87]N. Walkden, J. Harrison, S. Silburn, T. Farley, S. S. Henderson, A. Kirk, F. Militello, A. Thornton, and the MAST team, "Quiescence near the x-point of MAST measured by high speed visible imaging", Nuclear Fusion **57**, 126028 (2017).

[88]N. R. Walkden, B. Labit, H. Reimerdes, J. Harrison, T. Farley, P. Innocente, and F. Militello, "Fluctuation characteristics of the TCV snowflake divertor measured with high speed visible imaging", Plasma Physics and Controlled Fusion **60**, 115008 (2018).

[89]F. Scotti, S. Zweben, V. Soukhanovskii, D. Baver, and J. Myra, "Divertor leg filaments in NSTX-U", Nuclear Fusion **58**, 126028 (2018).

[90]D. Galassi, P. Tamain, H. Bufferand, G. Ciraolo, P. Ghendrih, C. Baudoin, C. Colin, N. Fedorczak, N. Nace, and E. Serre, "Drive of parallel flows by turbulence and large-scale exb transverse transport in divertor geometry", Nuclear Fusion **57**, 036029 (2017).

[91]D. Galassi, G. Ciraolo, P. Tamain, H. Bufferand, P. Ghendrih, N. Nace, and E. Serre, "Tokamak edge plasma turbulence interaction with magnetic x-point in 3d global simulations.", Fluids **50**, 4 (2019).

[92]R. D. Nem, P. Manz, N. Vianello, V. Naulin, N. Walkden, J. J. Rasmussen, B. Sieglin, A. Herrmann, and the ASDEX Upgrade team, "Quiescent regions below the x-point in ASDEX Upgrade", submitted in May 2020 (2020).

[93]B. Labit, I. Furno, A. Fasoli, A. Diallo, S. H. Müller, G. Plyushchev, M. Podestà, and F. M. Poli, "Universal statistical properties of drift−interchange turbulence in TORPEX plasmas", Phys. Rev. Lett. **98**, 255002 (2007).

[94]F. Sattin, M. Agostini, R. Cavazzana, G. Serianni, P. Scarin, and N. Vianello, "About the parabolic relation existing between the skewness and the kurtosis in time series of experimental data", Physica Scripta **79**, 045006 (2009).

[95]B. Nold, G. D. Conway, T. Happel, H. W. Müller, M. Ramisch, V. Rohde, U. Stroth, and A. U. Team, "Generation of blobs and holes in the edge of the ASDEX upgrade tokamak", Plasma Physics and Controlled Fusion **52**, 065005 (2010).

[96]T. A. Carter, "Intermittent turbulence and turbulent structures in a linear magnetized plasma", Physics of Plasmas **13**, 010701 (2006).

[97]J. A. Boedo, D. L. Rudakov, R. A. Moyer, and et al., "Transport by intermittency in the boundary of the DIII−D tokamak", Physics of Plasmas **10**, 1670–1677 (2003).

[98]R. J. Adrian, "Conditional eddies in isotropic turbulence", The Physics of Fluids **22**, 2065–2070 (1979).

[99]R. F. Blackwelder and L. S. G. Kovasznay, "Time scales and correlations in a turbulent boundary layer", The Physics of Fluids **15**, 1545–1554 (1972).

[100]N. Yan, A. H. Nielsen, G. S. Xu, V. Naulin, J. J. Rasmussen, J. Madsen, H. Q. Wang, S. C. Liu, W. Zhang, L. Wang, and B. N. Wan, "Statistical characterization of turbulence in the boundary plasma of EAST", Plasma Physics and Controlled Fusion **55**, 115007 (2013).

[101]G. S. Kirnev, V. P. Budaev, S. A. Grashin, E. V. Gerasimov, and L. N. Khimchenko, "Intermittent transport in the plasma periphery of the t-10 tokamak", Plasma Physics and Controlled Fusion **46**, 621–637 (2004).

[102]O. E. Garcia, J. Horacek, R. A. Pitts, A. H. Nielsen, W. Fundamenski, J. P. Graves, V. Naulin, and J. J. Rasmussen, "Interchange turbulence in the TCV scrape-off layer", Plasma Physics and Controlled Fusion **48**, L1–L10 (2005).

[103]Y. H. Xu, S. Jachmich, R. R. Weynants, and the TEXTOR team, "On the properties of turbulence intermittency in the boundary of the TEXTOR tokamak", Plasma Physics and Controlled Fusion **47**, 1841–1855 (2005).

[104]W. Fundamenski, O. Garcia, V. Naulin, R. Pitts, A. Nielsen, J. J. Rasmussen, J. Horacek, J. Graves, and J. E. contributors, "Dissipative processes in interchange driven scrape-off layer turbulence", Nuclear Fusion **47**, 417–433 (2007).

[105]H. Tanaka, N. Ohno, N. Asakura, Y. Tsuji, H. Kawashima, S. Takamura, and Y. U. and, "Statistical analysis of fluctuation characteristics at high- and low-field sides in l-mode SOL plasmas of JT-60u", Nuclear Fusion **49**, 065017 (2009).

[106]J. R. Harrison, G. M. Fishpool, A. J. Thornton, and N. R. Walkden, "The appearance and propagation of filaments in the private flux region in mega amp spherical tokamak", Physics of Plasmas **22**, 092508 (2015).

[107]J. Harrison, G. Fishpool, and B. Dudson, "Filamentary transport in the private flux region in MAST", Journal of Nuclear Materials **463**, PLASMA-SURFACE INTERACTIONS 21, 757–760 (2015).

[108]J. A. Boedo, M. J. Schaffer, M. Maingi, C. J. Lasnier, and J. G. Watkins, "Divertor EXB plasma convection in DIII-D", (1999).

[109]M. Schaffer, B. Bray, J. Boedo, T. Carlstrom, R. Colchin, C. L. Hsieh, R. Moyer, G. Porter, T. Rognlien, and J. Watkins, "EXB circulation at the tokamak divertor x-point", Physics of Plasmas **8** (2001).

[110]N. Walkden, private communication.

[111]N. Walkden, F. Riva, B. Dudson, C. Ham, F. Militello, D. Moulton, T. Nicholas, and J. Omotani, "3D simulations of turbulent mixing in a simplified slab-divertor geometry", Nuclear Materials and Energy **18**, 111–117 (2019).